

**Establishing Baseline Data for an Experimental Apparatus that
Measures Heat Transfer Under Conditions of
Oscillating Pressure and Flow**

by

Charles Edwin Dean

Bachelor of Science
United States Military Academy
(1983)

Submitted to the Department of Mechanical Engineering
in Partial Fulfillment of the Requirements for the Degree of

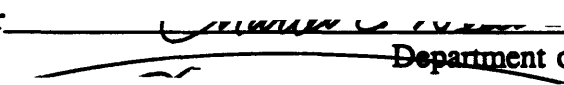
MASTER OF SCIENCE IN MECHANICAL ENGINEERING

at the


MASSACHUSETTS INSTITUTE OF TECHNOLOGY


May 1993

© Massachusetts Institute of Technology, 1993. All rights reserved,
except as granted to the United States under NASA Grant No. NAG3-1076
and Martin Marietta Energy Systems Grant No. 19X-5K139C.

Signature of Author 
Department of Mechanical Engineering
May 7, 1993

Certified by 
Professor John H. Lienhard V
Thesis Supervisor

Certified by 
Professor Joseph L. Smith, Jr.
Thesis Supervisor

Accepted by 
Professor Ain A. Sonin
Chairman, Departmental Graduate Committee

Establishing Baseline Data for an Experimental Apparatus that Measures Heat Transfer Under Conditions of Oscillating Pressure and Flow

by

Charles Edwin Dean

Submitted to the Department of Mechanical Engineering
on May 7, 1993 in partial fulfillment of the requirements
for the Degree of
Master of Science in Mechanical Engineering

Abstract

Mathematical correlations for predicting heat transfer under conditions of oscillating pressure and flow are in their developmental infancy. Such heat transfer is commonly found in reciprocating machinery such as internal combustion engines, gas springs, and Stirling cycle engines. In order to understand and improve the thermodynamic performance of reciprocal engines, it is necessary that mathematical correlations be developed that accurately predict heat loss through the walls of the components within these systems.

A heat transfer apparatus has been built that models the oscillating flow of a gas in a pipe as found in the regenerator of a Stirling engine. The apparatus is capable of measuring stream temperature and velocity at any point across the diameter of the pipe, the wall temperature, gas pressure, and gas to wall heat flux. This work addresses the collection of baseline heat transfer data for this apparatus under conditions of oscillating flow and pressure by (a) explaining the addition of a laser Doppler velocimeter to measure stream velocities, (b) investigating velocity profiles within the test section as the flow oscillates, and (c) recording and analyzing baseline heat transfer data.

Results show a close correlation between the phase angle between the two compressors mounted at each end of the test section and the complex-valued Nusselt number that has been derived. These results will be instrumental in developing codes that can predict this type of heat transfer in flows subject to oscillations in velocity direction and pressure.

Thesis Supervisors: Dr. Joseph L. Smith, Jr., and John H. Lienhard V
Titles: Professors of Mechanical Engineering

Acknowledgments

I would like to express my sincere appreciation to professors Joseph L. Smith, Jr. and John H. Lienhard V who not only taught me a great deal about our experiment and engineering in general, but who were always available to lend a hand to tame our experimental apparatus when it failed to cooperate.

The extensive assistance that I received from my research partners Alexander K. Tziranis and William A. Grassmyer enabled me to conduct this research and to complete my portion of the project. Alex was instrumental in building the thermocouple traversing system and installing the heat flux sensor. Bill helped me with daily wrench turning and data collection, and was especially helpful in preparing the computer programs that were used to smooth and reduce data, conduct a Fourier transformation of the data, and analyze the role of turbulence within the flow. I owe these two men my sincere gratitude.

My friends in the Cryogenic Engineering Laboratory kept me always heading in the right direction and provided me with a constant source of comraderie and humor. Sankar Sunder and Hayong Yun were especially key in this respect as were Eric Ratts, Michael Romm, Edward Ognibene, Norman Christophersen, and Jeffrey Hebb. Eric's patience while dragging me along on our many runs along the Charles River provided me with good exercise and company. Dr. Sangkwon Jeong played an important role for me as someone with considerable hardware knowledge who eagerly made himself available on short notice to provide advice, assistance, and support.

Robert Gertsen and Michael Demaree were extremely helpful in sharing their technical knowledge and skills and ensuring that I graduated with all ten fingers. I greatly enjoyed working with these two men who probably taught me some of the most important skills that I acquired while at MIT. Lisa Langone was instrumental in enabling me to keep straight with paperwork, purchases, and those ever missing receipts, and had the coffee hot every morning to jolt me into action.

I would like to recognize the support of Dr. Roy Tew at the NASA-Lewis Research Center and Mr. John Shonder at the Oak Ridge National Laboratory for actively supporting this project.

I am extremely grateful to the United States Army and especially the United States Military Academy for granting me the time and resources to follow a dream and to make that dream come true.

Finally and most importantly, I would like to thank my wonderful family, and especially my wife Didi, for helping me to meet the daily challenges as a student at MIT. Without their support and encouragement the endeavor would have been a much more arduous task and certainly not as much fun.

Table of Contents

Abstract	2
Acknowledgments	3
Table of Contents	4
Table of Figures	8
Nomenclature	10
Chapter 1. Introduction	12
1.1 Background	12
1.2 Theoretical Background of Heat Transfer Under Conditions of Oscillating Pressure and Flow	13
1.3 Research Objectives	17
Chapter 2. Experimental Apparatus	18
2.1 Phase 1: Smith-Ho Experimental Heat Transfer Apparatus	18
2.2 Phase 2: Tziranis Additions To The Phase 1 Apparatus	20
2.3 Phase 3: Modifying the Phase 2 Apparatus With A Laser Doppler Velocimeter	21
2.3.1 Components of the Laser Traverse System	22
2.3.2 Stepping Motor Control Box	25
2.3.3 Mineral Oil Smoke Generator	25
2.3.4 Assembled Phase 3 Apparatus	26

Chapter 3. Laser Doppler Velocimetry	31
3.1 Principles of Laser Doppler Velocimetry	31
3.1.1 Frequency Shifting By Bragg Cells	31
3.1.2 Measuring the Frequency of Seed Particles	32
3.2 The Aerometrics 300 mW Argon Ion Laser	34
3.2.1 Optical System	34
3.2.2 The Backscatter Transceiver	35
3.2.3 Photodetector	35
3.2.4 Doppler Signal Analyzer System	36
3.3 Optical Investigation Of Lasers Penetrating Curved Windows	36
Chapter 4. Oscillating Flow Velocity Study	46
4.1 Flow Symmetry Within the Experimental Apparatus	47
4.2 Comparison of Velocity Data With That of Other Research Teams	49
4.2.1 Uchida and White's Analytic Velocity Profiles	49
4.2.2 Experimental Studies by Hino et al and Akhavan et al	52
4.2.3 Comparison of Experimental Velocity Profiles with Previous Findings	53
4.3 Initial Examination of the Onset of Turbulence Within the Experimental Apparatus	54
Chapter 5. Experimentally Determined Heat Transfer Under Conditions of Oscillating Pressure and Flow	62
5.1 Revised Complex Nusselt Number Model	62
5.2 Experimental Procedure for Collecting Baseline Heat Transfer Data	66

5.3 Discussion of Baseline Heat Transfer Data	73
5.3.1 General Description of Results	73
5.3.2 Phase Angle Relationships	75
5.3.3 Complex Nusselt Number Relationships	76
Chapter 6. Conclusion	87
6.1 Summary of the Study	87
6.2 Recommendations for Future Work	88
6.2.1 Equipment Recommendations	88
6.2.2 Experimental Recommendations	90
Appendix A. Aligning the Laser Doppler Velocimeter	93
A.1 External and Internal Mirror Alignment	93
A.2 Fiber Optic Coupler Alignment	94
A.3 Laser Beam Polarization Alignment	95
A.4 Equalizing Dual Beam Power	96
A.5 Laser Beam Intersection and Transceiver Flexure Alignment	97
A.6 Laser Beam To Test Window Alignment	98
Appendix B. Computer Programs	101
B.1 Data Smoothing and Fourier Decomposition Program, "Smoothy"	101
B.2 Complex Nusselt Number and Phase Shift Program, "NuC1"	113
B.3 Turbulence Study Program, "Turb"	119
B.4 Velocity Profile Creation Program, "Phase5"	131
B.5 Theoretical Velocity Profile Creation Program, "White"	133

Appendix C. Calculation of Beam Refractance Due to Window	138
Appendix D. Baseline Heat Transfer Data	142
References	144

Table of Figures

2.1	Smith-Ho Experimental Apparatus	27
2.2	Tziranis' Thermocouple Traversing System	27
2.3	Three Piece Test Section	28
2.4	Laser Traversing System	28
2.5	Caliper Mount Blocks	29
2.6	Mineral Oil Smoke Generator	29
2.7	Phase 3 Apparatus	30
3.1	Shifting the Frequency of a Light Beam By the Use of an Acousto-optic Bragg Cell	41
3.2	Particle Passing Through Fringe Pattern	41
3.3	Probe Volume Dimensions	42
3.4	Optical System	42
3.5	Backscatter Transceiver	43
3.6	Laser Beams Properly Entering the Glass Pipe	43
3.7	Laser Beam Refractance due to Flat Glass Plate	44
3.8	Laser Beams Not Intersecting Within the Test Section	44
3.9	Bench Top Experiment to Investigate Beam Intersection	45
4.1	Initial Velocity Profiles at $Re_w=69.36$, $\Psi=180^\circ$	56
4.2	Improved Velocity Profiles at $Re_w=69.52$, $\Psi=180^\circ$	56
4.3	Coordinate System for a General Pipe	57
4.4	Laminar Theoretical Profiles, $f=0.005$ Hz, $Re_w=1.0$	57
4.5	Laminar Theoretical Profiles, $f=0.151$ Hz, $Re_w=30.0$	58
4.6	Laminar Theoretical Profiles, $f=5.0$ Hz, $Re_w=991.0$	58
4.7	Hino et al's Oscillating Velocity Time History at $f=0.33$ Hz, $Re_w=0.0344$, $D=0.00145$ m	59
4.8	Akhavan et al's Oscillating Velocity Profiles at $Re_s=1080$, $\Lambda=10.60$	59
4.9	Initial Centerline Periodic Velocity, $Re_w=15.85$, $\Psi=180^\circ$	60
4.10	Corrected Centerline Periodic Velocity, $Re_w=69.52$, $\Psi=180^\circ$	60
4.11	Turbulent Bursts at Centerline, $Re_w=69.52$, $\Psi=180^\circ$	61
5.1	RdF Heat Flux Sensor Calibration Curve	78
5.2	Diagram of Drive Tube Connection to Inertial Sheaves	78
5.3	Diagram of Compressor Variable Volumes	79
5.4	Raw and Smoothed Heat Flux Sensor Data, $f=5.07$ Hz, $Re_w=1044.8$, $\Psi=0^\circ$	79
5.5	Low Frequency Oscillations, $f=0.33$ Hz, $Re_w=65.4$, $\Psi=0^\circ$	80
5.6	Higher Frequency Oscillations, $f=5.07$ Hz, $Re_w=1004.8$, $\Psi=0^\circ$	80
5.7	Maximum Cyclic Heat Flux as a Function of Ψ and Pe_w	81
5.8	Maximum Cyclic ΔT as a Function of Ψ and Pe_w	81
5.9	Low Frequency Oscillations, $f=0.33$ Hz, $Re_w=65.4$, $\Psi=45^\circ$	82

5.10	Higher Frequency Oscillations, $f=5.07$ Hz, $Re_{\omega}=1004.8$, $\Psi=45^{\circ}$	82
5.11	Low Frequency Oscillations, $f=0.32$ Hz, $Re_{\omega}=64.42$, $\Psi=90^{\circ}$	83
5.12	Higher Frequency Oscillations, $f=6.02$ Hz, $Re_{\omega}=1193.08$, $\Psi=90^{\circ}$	83
5.13	Low Frequency Oscillations, $f=0.23$ Hz, $Re_{\omega}=45.58$, $\Psi=135^{\circ}$	84
5.14	Higher Frequency Oscillations, $f=6.81$ Hz, $Re_{\omega}=1349.6$, $\Psi=135^{\circ}$	84
5.15	1st Harmonic Phase Shift as a Function of Pe_{ω}	85
5.16	2nd Harmonic Phase Shift as a Function of Pe_{ω}	85
5.17	1st Harmonic Complex Nusselt Numbers as a Function of Pe_{ω}	86
5.18	2nd Harmonic Complex Nusselt Numbers as a Function of Pe_{ω}	86
6.1	Improved Test Section Design	91
6.2	Optical Window Bracket	91
6.3	Heat Flux Sensor Port	92
A.1	Schematic Diagram of Laser Beam Path	99
A.2	Fiber Optic Coupler	99
A.3	Transceiver Flexure Coupling	100
C.1	Geometry of Refractance Analysis	141
C.2	Similar Triangles	141

Nomenclature

a	General Fourier series cosine coefficient
b	General Fourier series sine coefficient
a_0	General Fourier series DC offset
c_p	Specific heat at constant pressure
c_v	Specific heat at constant volume
B	Angle of incidence of seed particle striking probe volume
d_f	Distance between two adjacent fringes in probe volume
d_m	Half width of probe volume
D	Diameter of pipe
D_{e-2}	Laser beam diameter based upon e^{-2} intensity at front focusing lens
f	Frequency of piston oscillations
f_p	Frequency of modulated light reflected off a seed particle
f_{shift}	Frequency difference between two incident beams
F	Focal length of front focusing lens (250 mm)
h	Heat transfer coefficient
h_c	Complex heat transfer coefficient
h_i	Imaginary part of complex heat transfer coefficient
h_r	Real part of complex heat transfer coefficient
i	$\sqrt{-1}$
k	Thermal conductivity of gas
K	White's pressure constant
l_m	Length of probe volume
n	n-th harmonic
N	N-th (final) harmonic
Nu_c	Magnitude of complex Nusselt number
Nu_i	Imaginary part of complex Nusselt number
Nu_r	Real part of complex Nusselt number
P	Pressure
Pe_ω	Oscillating flow Peclet number, $\omega D^2/\alpha$
q	Heat flux
q_c	Complex heat flux
q_m	Magnitude of n-th harmonic complex heat flux
r_p	Pressure ratio, (max pressure per cycle)/(min pressure per cycle)
r	Nondimensional radius of pipe
R	Inner radius of pipe
Re	Reynolds number, $V_{max}D/\nu$
Re^δ	Reynolds number based on Stokes boundary layer, $V_0\delta/\nu$
Re_p	Reynolds number based on mean piston velocity
Re_ω	Valensi number, $\omega r^2/\nu$
t	Time
T	Temperature
T_{cl}	Centerline gas temperature

T_{MM}	Mixed mean gas temperature
T_w	Wall temperature
u	Axial velocity component in a pipe
u^*	Nondimensional velocity
U	Internal energy
v	Radial velocity component in a pipe
V	Volume
Y	Admittance (1/Resistance)
α	Thermal diffusivity
δ	Stokes boundary layer thickness, $(2\nu/\omega)^{1/2}$
Δ	Difference
ΔT	Temperature difference between center line gas temperature and wall temperature
ΔT_n	Magnitude of n-th harmonic complex temperature difference
κ	Half angle between two incident laser beams
λ	Wavelength of laser beam
Λ	Wavelength of acoustic waves in Bragg cell
ν	Kinematic viscosity
ϕ	Phase angle of harmonic
ψ	Pfriem's variable
Ψ	Phase angle between compressors
ρ	Density
θ	Angular offset of laser beams striking glass pipe
ω	Angular frequency
ϑ	Higher order terms

SUBSCRIPTS

c	Complex
dc	Fourier series DC offset
i	Imaginary component
n	n-th harmonic
o	Mean
r	Real component
q	Heat flux
T	Temperature

Chapter 1

Introduction

1.1 Background

For the better part of the last twenty years, several research groups have investigated heat transfer under conditions of oscillating pressure and flow in an effort to obtain numerical heat transfer correlations for this type of periodic motion. The objective of these studies has been to better enable engineers to improve the performance of reciprocating machines, and in particular, the regenerators found within Stirling cycle engines. Even though several correlations for the Nusselt number have been derived from a handful of experimental and analytic studies, the search continues for precise correlations that describe the periodic heat transfer that occurs within oscillating flows subject to large amplitude pressure variations.

Heat transfer to the walls of a reciprocating machine represents a primary source of thermodynamic inefficiency. Estimation of wall heat transfer is difficult in these situations not merely due to the flow oscillating, but because the large pressure variations provide a means of entropy transfer to the walls that is independent of heat conduction through the boundary layer. Consequently, standard convection theory or heat transfer coefficients - which are developed for isobaric flows - are not applicable to such processes. More general models are required.

This thesis reports baseline heat transfer experiments in a new apparatus that produces oscillating flow with an independently variable pressure oscillation. These experiments will facilitate the development of a wall heat loss correlation that can be applied over a broad range of pressure and flow conditions, especially those typical of Stirling machines. Because a phase shift between the pressure and temperature fields is

inherent in flows of this type, the results are most conveniently expressed in terms of a complex-valued Nusselt number. The experimental results are correlated in that form.

1.2 Theoretical Background of Heat Transfer Under Conditions of Oscillating Pressure and Flow.

A seminal investigation of heat transfer within an oscillating flow was conducted by H. Pfriem (1943) who solved a simplified energy equation and reported that heat transfer under conditions of oscillating pressure should be out of phase with the bulk

$$\text{Energy equation } \frac{\partial T}{\partial t} = \alpha \frac{\partial^2 T}{\partial x^2} + \frac{1}{\rho c_p} \frac{\partial P}{\partial t} \quad (1.1)$$

gas-to-wall temperature difference. Pfriem assumed that density was constant and that convection was negligible. His assumption of a constant density introduced error into his simplified solution on the order of c_p versus c_v . In fact, he should have considered density as variable to evaluate a heat source at constant temperature, and density as constant to evaluate temperature change as a result of the heat transfer. Pfriem's early work was either lost or ignored, but more recently numerous research groups have analytically and experimentally demonstrated that Pfriem's analysis was generally representative of the phenomena of oscillating heat transfer. His resulting complex Nusselt number equation is:

$$Nu_c = D\psi \frac{[(1 - e^{-2\delta\psi}) + s\psi(1 + e^{-2\delta\psi})]}{[(1 - e^{-\delta\psi})^2 + s\psi(1 - e^{-2\delta\psi})]} \quad (1.2)$$

where

$$\psi = \sqrt{i\omega\alpha_o}$$

Pfriem's boundary layer thickness is appropriately related to Stokes' boundary layer thickness, δ , which, for fluids with a Prandtl number of unity, can be written as:

$$\delta = \sqrt{2\nu/\alpha_0}$$

Pfriem defines the term s as:

$$s = \frac{\text{Volume of Turbulent Core}}{\text{Heat Transfer Surface Area}}$$

Pfriem's work demonstrated analytically that a phase shift exists between the heat transfer between the gas and the duct wall and the temperature difference between the turbulent core and the wall. These findings indicated that the steady-state correlations for convective heat transfer were inappropriate for internal combustion engines as well as other reciprocating machines. Pfriem demonstrated that at low frequency oscillations, the periodic heat flux and temperature difference are in phase whereas at higher frequencies the heat flux leads the temperature difference by a phase shift of 45°. He explained that the highest temperature rise on compression is due to the greatest pressure rise and that the core temperature would therefore lead the wall temperature by 180° due to the thermal boundary layer. Pfriem then stated that the heat flow needs time to reach the wall from the core and that the peak heat flow would consequently lead the temperature oscillation by a phase angle between 0° and 180°. He found this phase angle to be 45° (Pfriem, 1943, pp 9-10).

More recently, Annand and Pinfold (1980) reported a Nusselt number correlation based upon experimental data taken in one cylinder of a Leyland E.0600 compression-ignition engine. Their equation is:

$$Nu = 0.3Re_p^{0.7} \left[1 + 0.27 \frac{D}{V\Delta T} \frac{dT_{CL}}{dt} \right] \quad (1.3)$$

where ΔT is the difference between the gas bulk temperature and the wall temperature, V is the instantaneous gas velocity, and the Reynolds number, Re_p , is based upon the mean piston velocity. Annand and Pinfold determined that it was very difficult to find

a correspondence between the temperature difference, ΔT , and the heat flux. Even though they found phase shifts between the two, these shifts were inconsistent across their range of frequencies and were a function of the ability of the particular gas to heat and cool and not as much a function of the temperature difference between the gas core and the duct wall (Annand and Pinfeld, 1980).

A few years later K. P. Lee (1983) made an analytic study of periodic heat transfer and independently derived Pfriedman's solution of the energy equation (Eq. 1) except that Lee modelled turbulence by incorporating a turbulent thermal diffusivity into the Peclet number, Pe_ω . Lee's resulting equation for the complex Nusselt number is:

$$Nu_c = \sqrt{\frac{Pe_\omega}{2}} \frac{[(1+i)\tanh z]}{[1-\tanh z/z]} \quad (1.4)$$

$$\text{where } z = (1+i) \sqrt{\frac{Pe_\omega}{32}}$$

$$Pe_\omega = \frac{\omega D^2}{\alpha}$$

Lee's results showed that at low values of Pe_ω (< 0.125), the difference in gas to wall temperature is in phase with the heat transfer. He also found that when Pe_ω is greater than 50, the temperature difference lags the heat transfer by 45° .

Kornhauser and Smith (1988) took experimental data in a closed end cylinder apparatus and reported that heat flux under conditions of oscillating pressure and flow was proportional to both temperature difference and the rate of change in temperature. For purely sinusoidal variations, dT_{Cl}/dt drives the 90° out of phase component of the heat flux. Kornhauser and Smith assumed that T_w is constant and the mixed mean temperature

varies sinusoidally as:

$$T_{MM_c} = (T_{MM_c})_r + i(T_{MM_c})_i = T_{MM_{dc}} + T_{MM_a} \cos \omega t + iT_{MM_b} \sin \omega t \quad (1.5)$$

The first derivative with respect to time of Equation 5 is:

$$\frac{dT_{MM_c}}{dt} = -\omega T_{MM_a} \sin \omega t + i\omega T_{MM_b} \cos \omega t \quad (1.6)$$

The real components of Equations 5 and 6 show that these two equations are 90° out of phase with one another. Since the actual heat transfer taking place is equal to the real component of the complex heat transfer, Kornhauser and Smith wrote:

$$(q_c)_r = \frac{k}{D} \left[(Nu_c)_r [(T_{MM_c})_r - T_w] + \frac{(Nu_c)_i}{\omega} \frac{d(T_{MM_c})_r}{dt} \right] \quad (1.7)$$

a further simplification provides their final equation for heat flux:

$$q = \frac{k}{D} \left[Nu_r (T_{MM} - T_w) + \frac{Nu_i}{\omega} \frac{dT_{MM}}{dt} \right] \quad (1.8)$$

Kornhauser found that for Pe_ω over 100, his expression for complex heat transfer correlated quite closely with his experimental data and that the Nusselt number could be simplified to:

$$Nu_r = Nu_i = 0.56 (Pe_\omega)^{0.69} \quad (1.9)$$

$$\text{for } 100 \leq Pe_\omega \leq 10000$$

At lower values of Pe_ω , no simple equation could be obtained.

As of the completion of Kornhauser's experiments in 1989, no experimental results had yet been published on periodic heat transfer under conditions of oscillating pressure

and flow in an apparatus that allows independent control of flow variation and pressure variation. As of this same year, neither analytic nor experimental results from within the engineering community had shown phase shifts between heat flux and ΔT to exceed the 45° that Pfriem had predicted close to half a century earlier.

1.3 Research Objectives.

The objectives for this research project are to:

(a) Install a laser Doppler velocimeter (LDV) onto the test section of an existing heat transfer apparatus so that cross-sectional velocity measurements can be recorded and related to concurrent periodic heat transfer, temperature, and pressure measurements.

(b) Configure the experimental apparatus' data acquisition system so that all velocity, temperature, heat flux, and pressure data are collected simultaneously as a function of shaft encoder position.

(c) Collect baseline heat transfer data across the frequency range of the apparatus while varying the phase angle between the two compressors and maintaining the pressure ratio close to 2.0.

Chapter 2

Experimental Apparatus

This chapter will briefly describe the experimental apparatus and its modifications with particular emphasis placed on the Phase 3 alterations. The reader is directed to the 1991 thesis of Yung Ho and the 1992 thesis of Alexander Tziranis for further details on their work in respectively making the Phase 1 apparatus and completing the Phase 2 modifications. The primary reference for the overall apparatus is Ho's thesis. Ho designed and built the basic apparatus that produces the oscillating flow under conditions of oscillating pressure. Ho's work is addressed henceforth as Phase 1 of the equipment's development. Tziranis' Phase 2 work modified Ho's apparatus by mounting a traversing thermocouple system onto the outside of the test section. This traverse system enables a 6-inch extended body thermocouple to enter the inside of the test section through a sealed port. The thermocouple can then be traversed across the diameter of the test section to record temperature measurements. Tziranis also installed a heat flux sensor on the inside wall of the test section to record gas to wall heat flow. The final Phase 3 modifications were made by the author and included building a traversing system for a laser Doppler velocimeter's (LDV) transceiver that was then mounted to the outside of the test section. The laser's traverse system enables the LDV to record axial periodic gas velocities across the diameter of the test section.

2.1 Phase 1: Smith-Ho Experimental Heat Transfer Apparatus.

During the period of 1989-1991, Yung Ho, working with Professor Joseph L. Smith, Jr. at the Cryogenic Engineering Laboratory at MIT, designed and built a dual compressor experimental apparatus for measuring cyclic heat transfer under conditions of oscillating pressure and flow (Fig. 2.1). The apparatus was built to study the periodic heat transfer found in Stirling engine regenerators and was a follow-on to the single piston gas spring apparatus that Alan Kornhauser had reported in his 1989 doctoral thesis.

The Smith-Ho apparatus consists of six basic elements: two 9-inch stroke by 11-inch bore Joy compressors joined by a common drive shaft and with a variable phase angle Ψ between the two compressors, a Westinghouse 25 HP DC motor that powers the compressors through a belt and pulley system, a 1.75-inch inner diameter pipe joining outlet/inlet ports on the head of each compressor, a three piece 1.75-inch inner diameter test section centered in the middle of the pipe connecting these two compressors, two variable clearance volumes mounted to the head of each compressor to enable adjustments of the pressure ratio within the test section, and a bounce volume pipe connecting the gas under the piston in one compressor to the gas occupying the same space in the other compressor. The DC motor is controlled by a variable voltage auto transformer that controls the RPM of the compressor crankshafts. The compressor directly connected to the DC motor is referred to as the driven compressor; the compressor connected to the driven compressor through the drive shaft is consequently referred to as the undriven compressor.

The test section in the Smith-Ho apparatus was capable of measuring gas pressure, wall temperature, centerline gas temperature, and crank angle of the undriven compressor as the system went through each 360° cycle. At this stage of the apparatus' development, the wall heat flux and the flow velocities were calculated from the recorded data.

Ho wrote a data acquisition program that permitted the data to be collected by two eight channel Data Translation DT2801-A analog and digital I/O boards. This program was a modification of Kornhauser's earlier data acquisition program for his two space apparatus (Kornhauser, 1989). Ho's data collection was triggered by a Vernitech optical shaft encoder mounted to the undriven compressor crank shaft. Ho also wrote a data reduction program and a data analysis program, both of which can be found in his thesis.

2.2 Phase 2: Tziranis Additions to the Phase 1 Apparatus.

From 1990-1991, Alexander Tziranis improved the Phase 1 apparatus by installing both a traversing thermocouple system to measure cross-sectional gas temperatures as depicted in Figure 2.2, and an inside wall heat flux sensor. In order to add these instruments to the Phase 1 apparatus, Tziranis modified the center section of the three piece test section (Fig. 2.3). These modifications involved drilling and threading a through hole to facilitate passing through the 5.5-inch extension rod for the traversing thermocouple, drilling a conical through hole to later serve as an optical view window for a LDV system, mounting a Pyrex glass pipe on the inside of this steel center piece of the test section, mounting a heat flux sensor to the inside of the Pyrex glass pipe, and constructing the traversing system for the thermocouple.

The traversing thermocouple was custom manufactured by the Paul Beckman Company and consists of a Type E thermocouple at the end of 0.008-inch diameter, 0.5-inch long hollow rod mounted to the end of a 0.125-inch diameter, 5.5-inch long stainless steel extension rod. The 0.008-inch rod separating the thermocouple junction from the 0.125-inch extension rod was designed to minimize flow disturbances caused by the extension rod from reaching the thermocouple junction. The end of this extended thermocouple opposite to the junction is mounted to a Berg model LBSC-20 ball slide. The ball slide is traversed by a Hurst model 4014-002 Linear Stepping Actuator. The model 20455-1 heat flux sensor was made by the RdF Corporation and basically consists of two thermocouples mounted on opposite sides of a material whose coefficient of thermal conductivity is known.

Tziranis milled a flat section on the outside bottom of this center cylinder of the test section to permit the horizontal support beam holding the thermocouple traverse system to be bolted to the test section. This steel beam secures the base of the Berg ball slide as well as the motor mount bracket for the Hurst stepping motor.

Tziranis and Stephen Umans wrote a data acquisition program that included command lines for pulsing the stepping motor and to thus position the thermocouple's junction at any location across the inside diameter of the test section. The positioning of the thermocouple is accurate to 0.001-inches.

2.3 Phase 3: Modifying the Phase 2 Apparatus with a Laser Doppler Velocimeter.

The work for this thesis centered on modifying the Phase 2 apparatus so that it would accommodate an Aerometrics 300 mW Argon ion laser Doppler velocimeter. Included in this work was the building of a traversing system for the LDV's transceiver that positions the intersection of the two emitted laser beams at any position across the inside diameter of the of the test section. The steel support beam for the laser's traversing system perpendicularly connects to Tziranis' horizontal support beam. As shown in Figure 2.4, this vertical support beam holds the ball slide for traversing the transceiver and the motor mount for the stepping motor. The same computer commands that position the traversing thermocouple, position the laser beams. Phase 3 modifications additionally included building a traverse system control box that permits the operator to select whether the laser, thermocouple, or both are traversed by the computer and in which direction (into or out of the flow) either is moved. Included with the Aerometrics LDV system was an external input device that permits other instruments' signals to be collected by the LDV's software each time the LDV's signal processor collects velocity data. With the completion of the Phase 3 modifications, the overall system can now measure temperature and flow velocity data across the inside diameter of the test section, wall temperature and pressure readings, and compressor crank angle positions. The calculations for bulk velocity and heat flux that Ho performed are no longer necessary and have now been replaced by direct data collection from the new instruments.

2.3.1 Components of the Laser Traverse System.

(a) Vertical Support Beam.

The vertical support beam is machined out of steel and measures 19-inches long, 4-inches wide, and 0.635-inches thick. Its function is to secure all stationary components of the laser traverse system. At the end closest to Tziranis' horizontal support beam, is a welded extension perpendicular to the vertical support beam. This extension measures 5.6-inches long, 4-inches wide, and 0.635-inches thick and permits the vertical support beam to be bolted and pinned to the horizontal support beam. The vertical support beam fits into a 0.637-inch milled groove in the extension and the two are then welded together. After these two were welded, the extension was re-milled following any thermal expansion to ensure that the extension remained perpendicular to the vertical support beam and parallel to the horizontal support beam. Besides being bolted together, the extension and the horizontal support beam are pinned together with two hardened steel dowel pins that always maintain a common alignment between the horizontal and vertical support beams.

(b) Daedal Ball Slide.

A Daedal model 4601 ball slide is screwed to the vertical support beam 10.6-inches up from the intersection of the beam extension with the vertical support beam. This ball slide measures 6-inches long, 2.62-inches wide, and 1-inch high. The slide can traverse 2-inches in either direction of its center and is accurate to 0.00008-inches for every 1-inch of travel. This slide is capable of supporting up to 64 pounds normal to its traverse but is only required to carry less than 10 pounds in line with its traverse for this experiment.

(c) Transceiver Spacing Block.

The transceiver spacing block is machined aluminum and is designed to position the laser beams emitting from the transceiver, directly above the optical window built into the test section. The block measures 1.5-inches high, 6-inches long, and 2.32-inches wide. The block is screwed to the top of the ball slide. A 0.25-inch hole is drilled at the top end of the block with an adjoining set screw to secure the stepping motor's Acme screw to the block.

(d) Motor Mount.

The motor mount holds the stepping motor in place and is milled out of aluminum. The mount measures 1-inch long, 2.8-inches high, and 4-inches wide. This mount has a 0.75-inch through hole in its center to permit the stepping motor's Acme screw to pass through the motor mount. The mount is screwed to the vertical support beam.

(e) Hurst Stepping Motor.

The Hurst model 4014-002 linear stepping actuator is identical to the motor used for the traversing thermocouple system. This 12 Volt DC motor is capable of traversing a 0.25-inch diameter Acme screw 0.001-inches with each pulse received from the Hurst model EPC-013 motor controller board. The board in turn receives pulses from the computer's data acquisition board based upon the desired traverse distance input through the keyboard.

(f) Traverse Stops.

Two traverse stops are mounted with set screws onto the Acme screw on either side of the stepping motor. These stops deny the laser's further traverse at either end of the test section's inner diameter. Two of these stops are also used on the Acme screw in the traversing thermocouple system and serve the additional purpose of preventing the researcher from inadvertently moving the junction of the thermocouple into the wall of the test section.

(g) Caliper Mounts.

In order to know where the intersection point of the two laser beams is within the test section at all times, a Mitutoyo model 06252837 digital vernier caliper is mounted both to the spacing block and to the motor mount by clamping its jaws in each location with a caliper mount. These mounts are machined out of aluminum and are depicted in Figure 2.5. The caliper can be zeroed in any location, but was always zeroed when the traverse had pulled the beams out of the center of the test section and to the inside of the test section wall closest to the laser transceiver, where a traverse stop prevented further movement.

(h) Laser Support Bracket.

The laser support bracket was manufactured by Aerometrics as a component of the laser transceiver. The base of the bracket is bolted with two thumb screws to the spacing block. This bracket measures 0.5-inches high, 6-inches wide, and 9-inches long. The thumb screws pass through slotted holes in this bracket and into threaded holes in the spacing block. Due to these slotted holes in the bracket, the bracket itself can be moved slightly before the thumb screws are tightened. This movement allows the point of intersection of the two laser beams to be properly aligned with both the traverse and the test section.

2.3.2 Stepping Motor Control Box.

In order to control the stepping motors for both the thermocouple traverse and the laser traverse, two Hurst model EPC-013 motor controller boards were purchased. These boards receive the same signal from a channel in the computer's data acquisition board. Based upon the wiring for each board, the signal from the computer causes the corresponding stepping motor to turn in one direction or the other. The control box provides a housing for these two controller boards and gives the operator a series of switches and light emitting diodes (LEDs) to choose which motor will operate when the computer's pulses arrive, which direction either motor will turn, and whether the motors will turn a full step or a half step with each pulse.

2.3.3 Mineral Oil Smoke Generator.

As will be described in Chapter 3, the flow stream must be seeded with foreign particles for the LDV to record velocity data. The mineral oil smoke generator provides the seed for the air within the apparatus. The particles produced by this generator were measured with an Aerometrics laser Doppler particle size analyzer and found to average 1.3 μm in diameter. They are noncorrosive to the apparatus and nontoxic to the researchers. The generator is depicted in Figure 2.6 and uses compressed house air at 40 psi to draw the oil out of the reservoir due to the Venturi effect and into the burn chamber. Within the burn chamber the oil is burned with the heat emitted from a propane torch and the resulting smoke is blown into the test section. The smoke was introduced to the test section prior to a series of experimental runs. After the smoke was seen to have penetrated the entire system, the generator was turned off, its valves closed, and then the data was taken. Using this method, sufficient smoke for data collection remained airborne within the test section for over one hour at a time. Over time the seed particles accumulated on the inside of the test section and required that we clean the test section periodically to prevent the oil from insulating the heat flux sensor.

2.3.4 Assembled Phase 3 Apparatus.

The laser traverse system was completed before the Aerometrics laser arrived from the manufacturer. With the addition of this LDV system, the apparatus took on the appearance depicted in Figure 2.7. The Gateway model 2000 486 computer collects all laser data and external input data from the sensors mounted on the test section. The Dell model 325SX 386 computer positions the traversing systems. Two data runs are required to record all data at each experimental setting due to the limited three channels in the external input device.

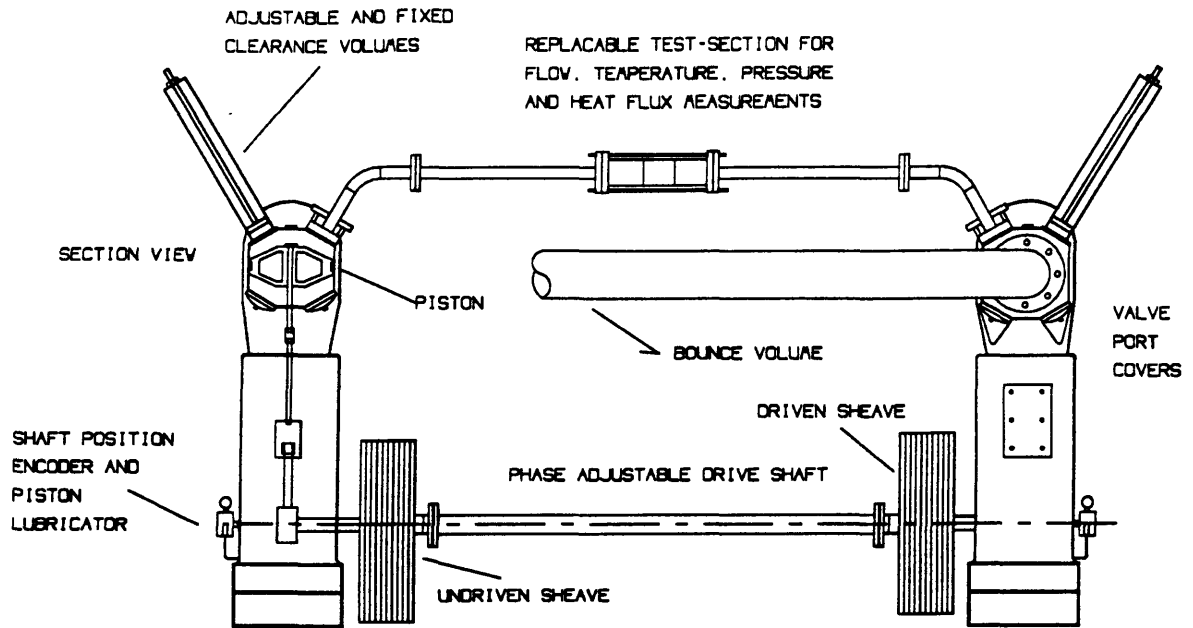


Figure 2.1 Smith-Ho Experimental Apparatus (Ho, 1991)

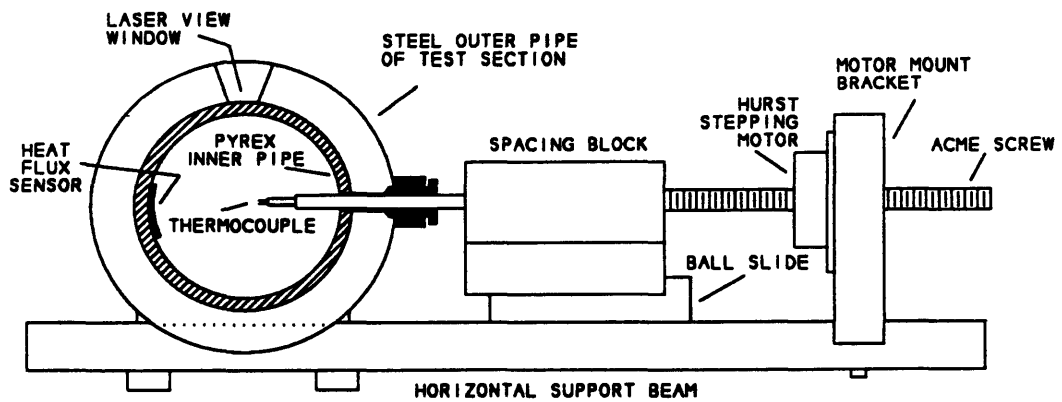


Figure 2.2 Tziranis' Thermocouple Traversing System

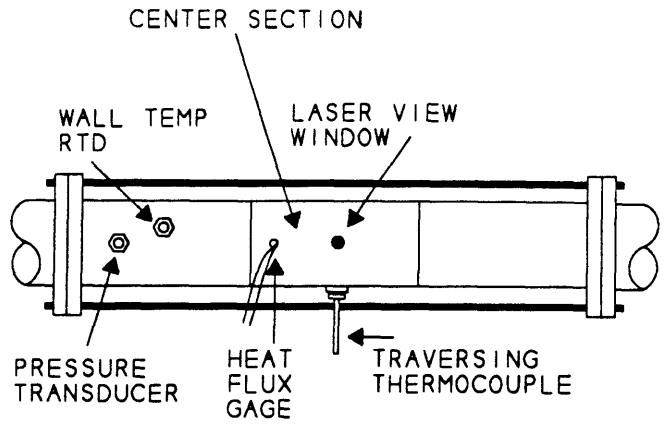


Figure 2.3 Three Piece Test Section

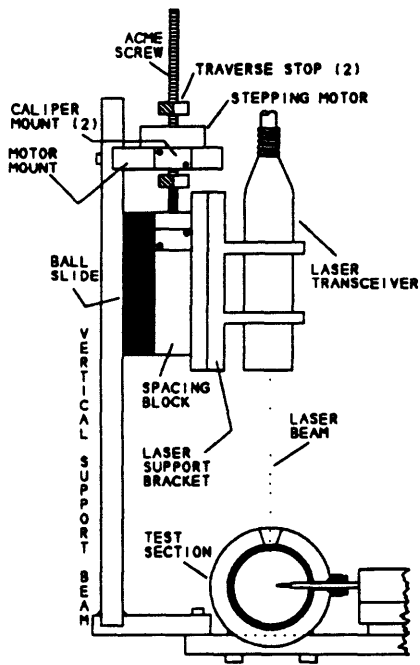


Figure 2.4 Laser Traversing System

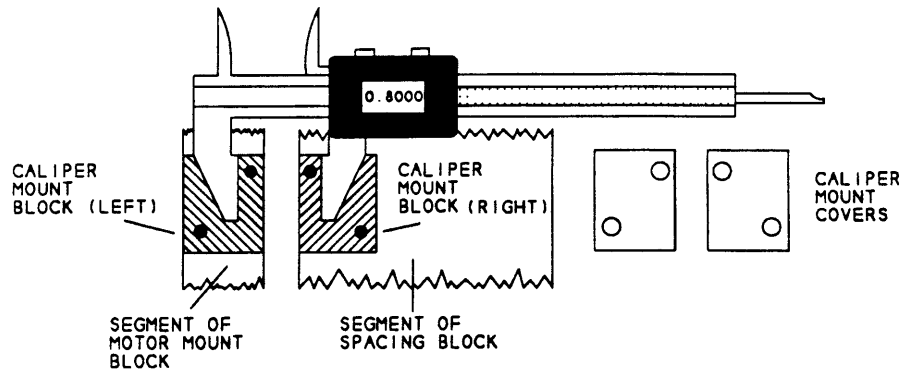


Figure 2.5 Caliper Mount Blocks

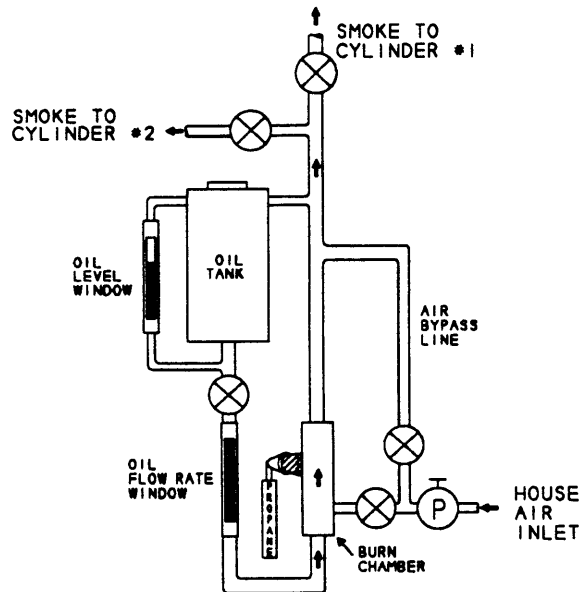


Figure 2.6 Mineral Oil Smoke Generator

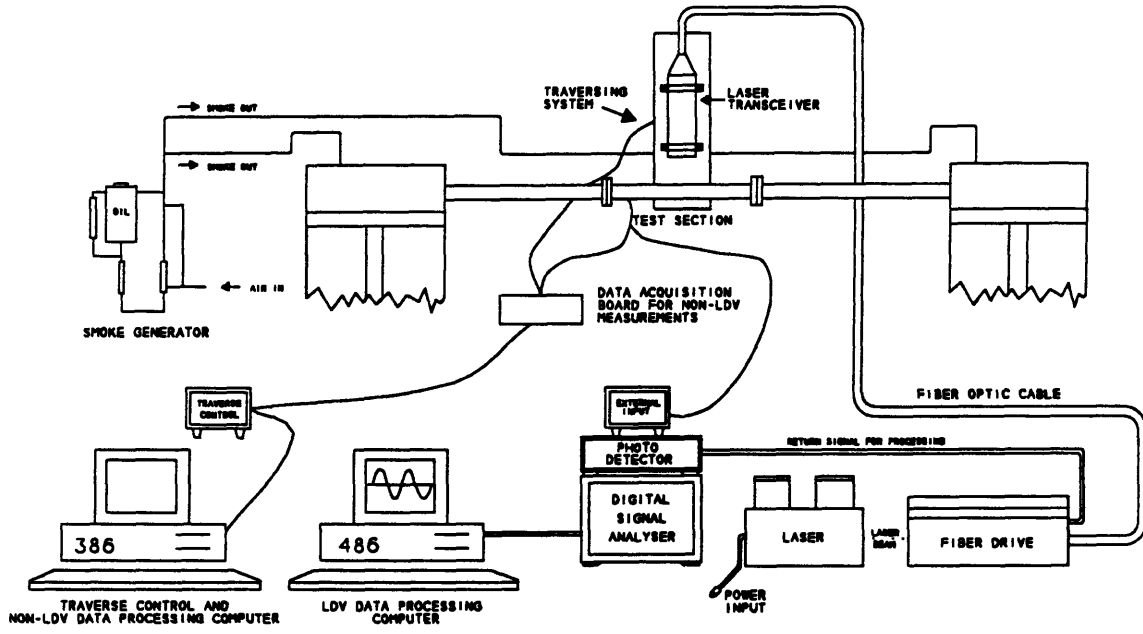


Figure 2.7 Phase 3 Apparatus

Chapter 3

Laser Doppler Velocimetry

Lasers are widely used today in researching fluid flow phenomena in such areas as internal pipe and impeller flows, external propeller flows, and aerodynamic design. In most cases, the predecessor to the laser Doppler velocimeter (LDV) was the hot-wire anemometer. The LDV has proven itself as a much simpler instrument to utilize as well as a more accurate instrument over the hot-wire anemometer. A significant advantage to the LDV type system is that it is a nonintrusive device. The LDV can record data through a window to the flow and prevents having to place hot-wire instruments into the flow. LDVs are manufactured by a handful of companies throughout the world and these companies produce a variety of models that can investigate 1-D to 3-D flow fields and are also capable of analyzing particles within the flow as might be used for studying particle deposition. In general, these lasers all utilize the same principles as this chapter will describe.

3.1 Principles of Laser Doppler Velocimetry.

3.1.1 Frequency Shifting by Bragg Cells.

Emitting from the transceiver of the LDV are two laser beams that intersect within the test section. These two beams differ in frequency as a result of having previously passed through a Bragg cell within the LDV's fiber drive. The Bragg cell receives the original reference laser beam that emits from the laser, splits the beam into two beams, and varies the frequency of the two beams by a set frequency shift. The frequency difference between the shifted beam and the original reference beam is equal to the frequency of the acoustic waves travelling within the cell that are generated by a piezoelectric transducer as shown in Figure 3.1. These waves travel at speed V and have a wavelength Λ (Drain, 1980).

3.1.2 Measuring the Frequency of Seeded Particles.

In order to utilize the LDV to measure flow velocities, particles must exist within the flow that will scatter light from the laser beams. Some fluids, such as common household water, naturally carry sufficiently large particles that the introduction of other seed particles may not be necessary. Most fluids and gases require the addition of seed particles before a LDV can be used. The size of these seed particles is very important. On one hand large particles scatter light better than do smaller particles, but large particles may not follow the high frequency characteristics of the flow as will the small particles. Generally speaking, particles on the order of 0.1 to 2 μm in diameter are sufficient for properly seeding the flow (Aerometrics' LDV brochure). Many different types of particles are used to seed flows based upon the type of flow medium. The reader is referred to the TSI Incorporated mini-course on LDV systems (TSI, 1992) for a detailed discussion of what type of seed particle is recommended for various flows.

As the two laser beams depart the fiber drive, they are redirected by lenses within the transceiver to intersect one another within the flow at their respective focal points. As these two focused Gaussian beams intersect, they interfere with one another and cause an interference fringe pattern as depicted in Figure 3.2. This ellipsoidal shaped region of fringes is called the probe volume. The fringes are parallel to one another and run parallel to the centerline of the transceiver. The distance between the fringes is:

$$d_f = \frac{\lambda}{2\sin\kappa} \quad (3.1)$$

where κ is the half angle between the two incident beams. As a seed particle travels with

the flow across the fringe pattern, it causes a modulation of light intensity at a frequency of:

$$f_p = \frac{2u \cos B \sin(\alpha/2)}{\lambda} \quad (3.2)$$

The light scattered by this particle is collected back through the same optical lenses in the transceiver that were previously used by the incident beams, and passes this reflected light to the photodetector. The computer's signal processing software can determine the velocity u of the particle from the frequency of the reflected light because:

$$u = \frac{d_f}{t} = d_f \times f_p \quad (3.3)$$

where t is the time the particle takes to cross two adjacent fringes and f_p is the Doppler shift frequency of the light scattered by the particle.

The probe volume's dimensions are easily determined. The half width d_m of the probe volume measured perpendicular to the axis of the lenses in the transceiver and in line with the recorded velocities of the seed particles is:

$$d_m = \frac{4F\lambda}{\pi D_{e,2}} \quad (3.4)$$

where F is the focal length of the transceiver's front focusing lens, λ is the wavelength of the laser beams, and $D_{e,2}$ is the focused beam diameter. The length of the probe volume, l_m , is computed as follows where κ is the half angle between the two incident beams:

$$l_m = \frac{d_m}{\tan \kappa} \quad (3.5)$$

An LDV equipped with a Bragg cell can measure both positive and negative velocities. Due to the frequency difference between the two incident beams, the fringe

pattern oscillates at a frequency equal to the frequency difference between these two beams (the Bragg cell transducer's frequency, f_{shift}). When a LDV measures an oscillating flow that has both positive and negative velocities, the particle's frequency f_p differs based upon whether the particle is travelling in the positive or the negative direction. A particle travelling in the same direction as the oscillation of the fringe pattern has a frequency equal to $f_p - f_{\text{shift}}$. A particle moving in the opposite direction as the oscillation of the fringe pattern has a frequency of $f_p + f_{\text{shift}}$.

3.2 The Aerometrics 300 mW Argon Ion Laser.

The Aerometrics laser Doppler velocimeter (LDV) was built for the project to measure oscillating 1-D velocity components. Besides the Omnichrome air cooled 300 mW Argon ion laser, this system consists of five basic components, an optical system, an optical transceiver, a photodetector, an external input device, and a Doppler signal analyzer (DSA) system. These components will each be described separately to offer the reader a general understanding of how each piece of the LDV system cooperates to yield velocity data.

3.2.1 Optical System.

The optical system for the LDV is based upon the use of fiber optic cables transmitting the laser beams to the separate focusing optics within the transceiver. The optical system consists of an output and an input external mirror, a Bragg cell fiber drive, a Bragg cell driver, and a fiber optic cable. The beam emitted from the Omnichrome laser is directed first by the output external mirror and then the input external mirror into the Bragg cell fiber drive. Within the fiber drive, the beam is first filtered to permit only the 514 nm light to pass to the Bragg cell. Within the Bragg cell this beam is separated into two beams with the second beam being oscillated to a 40 MHz higher frequency than the original reference beam as was more fully described in paragraph 3.1.1. These two

beams are then redirected by two internal mirrors to intersect a prismatic rhomboid that further separates the two beams from the one another and focuses the beams. Two fiber optic couplers secure the two ends of the transmitting optical fibers in position to intersect these two beams at their respective focal points. These two fibers then carry the beams to the transceiver.

3.2.2 The Backscatter Transceiver.

The fiber optic cable enters the conical rear of the transceiver's housing and the two individual optical fibers terminate at two flexure couplings. The couplings direct the two beams departing the optical fibers through two through holes drilled in the receiver lens and to the front focusing lens. This front focusing lens has a focal distance of 250 mm and redirects the two beams to intersect at their common focal point 250 mm in front of the transceiver. As a seed particle passes through the probe volume, the scattered light is collected by the front focusing lens and redirected to the receiver lens which in turn focuses this light onto the return signal optical fiber mounted in the center rear of the transceiver's housing, between the two flexure couplings. This return signal light is then transmitted by this optical fiber through the optical cable to the fiber drive and directly to the photodetector.

3.2.3 Photodetector.

The photodetector transforms the return signal light arriving through the optical fiber into an electrical signal which is then amplified by the detector's photomultiplier. This signal is then passed electronically to the LDV's Doppler Signal Analyzer (DSA).

3.2.4 Doppler Signal Analyzer System.

The DSA is a frequency domain signal processor that is used to analyze the signals received from the photodetector. The DSA system consists of the DSA's electronics, a high speed array processor, a computer interface card, and system software used in the Gateway model 2000/486 computer which was part of the LDV package. The DSA can process Doppler frequencies up to 150 MHz. Its two 160 MHz analog to digital converters (ADCs) concurrently measure quadrature mixing signals resulting in a combined maximum sampling frequency of 320 MHz. The DSA utilizes fast Fourier transformation algorithms to estimate a sample's frequency, and a Fourier Transform Burst Detector (FTBD) to detect and to then concentrate the signal processing on the center of the burst to minimize noise processing. The FTBD can perform up to 20 million Fourier transformations each second.

The signal processing itself is undertaken by first high pass filtering the signal to eliminate the Gaussian pedestal. The filtered signal is then logarithmically amplified to improve its dynamic range, is then given a quadrature mixing, and then sent through a low pass filter to raise the signal to noise ratio (SNR) and hence eliminate the higher frequency component produced within the mixer. The signal is then sent to the FTBD where continuous transformations are completed to determine the frequency and phase of the signals. Particle velocity is determined by the software based upon the frequency information produced by the FTBD for each particle with a sufficiently high signal to noise ratio. The analog burst detector determines the amplitude of the signal and prevents analysis of background noise (Aerometrics DSA brochure, 1992).

3.3 Optical Investigation of Lasers Penetrating Curved Windows.

The two laser beams that emit from the front focusing lens of the transceiver pass through air before they intersect the glass window in the test section. The glass window

is a small section of a pyrex glass pipe that is affixed by Loctite model 290 anaerobic adhesive to the inside of the metal pipe that forms the test section in the heat transfer apparatus. The glass pipe is 1.90 mm thick and provides an optical window to the flow that enables the flow to remain undisturbed as velocity measurements are taken by the LDV.

As discussed earlier, the two laser beams lie in a plane that must remain parallel to the flow in order to measure axial flow velocities. The experimental apparatus was designed so that this plane coincides with the long axis of the glass pipe at its apex as shown in Figure 3.5. When the beams intersect the glass in this manner, the glass appears to the beams as a flat plate with a constant thickness of 1.90 mm. As the beams enter the glass they refract in accordance with Snell's law as shown in Figure 3.6. This refraction moves their intersection point further into the pipe by a distance P . As the laser's traversing system moves the probe volume across the inside diameter of the pipe, the distance P remains 6.36 mm. The calculations for P can be found in Appendix D.

There are several potential problems that arise, however, when taking data inside a glass pipe. The first problem is that as the probe volume moves close to the far inside wall of glass pipe, light reflects off this wall and joins the reflected light coming off the seed particles that enters the transceiver. The computer ends up processing a very noisy signal that is a poor representation of the true signal. Some researchers counter this problem by coating the inside surface of the far wall with nonreflective paint to reduce these undesired reflections. Another common practice is to only measure data across the first half of the pipe's diameter and to then assume that the velocity profiles are radially symmetrical. This second method was used in this research after finding that the signals close to the far wall were too noisy.

The second problem with measuring any data with a LDV is that the LDV cannot take data at the surface of the wall. The reason for this is that probe volume is destroyed when the intersection point of the beams is closer to the wall than the half length of the

probe volume ($l_m/2$). The calculations below show the dimensions of the probe volume associated with this experiment as determined by Equations 3.4 and 3.5:

$$d_m = \frac{4F\lambda}{\pi D_{e-2}} = \frac{4(.250)(514 \times 10^{-9})}{(3.141593)(2 \times 10^{-3})} = 81.8 \mu m$$

$$l_m = \frac{d_m}{\tan \kappa} = \frac{(8.18 \times 10^{-5})}{\tan(4.574^\circ)} = 1.023 \text{ mm}$$

Due to the problems associated with traversing the probe volume close to a wall, some researchers stop taking data within 5% of the radius away from the wall (Bhunja, 1988). We were capable of taking data at a location 2% of the radius from the wall.

Experiment and theory have proven that the worst possible problems that can arise when passing two laser beams through the surface of a glass pipe are that the laser beams do not intersect or that they intersect at some location where they are not focused. If the alignment procedure that ensures that the plane of the two beams is parallel with the long axis of the glass pipe and that the beams enter this pipe through the apex of its curved surface, is inaccurate, then very poor data can be expected. When a beam of light strikes a transparent surface, it refracts into that surface in a plane made of the incident beam and the normal to the surface at the point of incidence (Snell's Second Law). When this surface is flat, this is of little concern. When the surface is curved, which is the case when our two laser beams are improperly aligned with the glass pipe, as exaggerated in Figure 3.8, the resulting plane passes through the glass in a completely different orientation than the plane formed by the two incident beams. Each of the two laser beams then refract into the glass in separate refractance planes that may or may not intersect inside the pipe. They will never intersect if the two beams intersect the glass symmetrically about the long axis of the pipe. They may intersect if the beams intersect the glass at a skewed angle. Even if the two refracted planes do intersect within the pipe, there is little chance that the beams in those planes will coincide at the same point along the line of intersection of these two planes. Even if these two beams do intersect along

this line of plane intersection, they will more than likely not be in focus at that point.

A bench top experiment was conducted to investigate whether or not the ideas just expressed are valid. The laser beams were sent through a glass pipe identical to the pipe used in the test section. The beams passed out of the inside of the pipe through an already existing hole on the far side. A microscope objective was placed outside this hole at the point where the beams appeared to intersect. The microscope objective magnified the image of these intersecting beams onto a screen. Figure 3.9 depicts the setup for this experiment. It was found that when the two beams properly intersected the glass pipe along its long axis ($\theta=0^\circ$), the microscope objective showed that they did indeed intersect and that they were in focus at the point of intersection. When the plane of the incident beams was turned to $\theta=90^\circ$ and the incident beam plane now lay perpendicular to the long axis of the glass pipe, the beams once again intersected, but this time they were not in focus at their intersection point. When the plane of the incident beams was placed at angles between the two just mentioned ($0^\circ < \theta < 90^\circ$), it was clearly seen that the beams did not intersect at all.

Several different techniques were considered for properly aligning the plane of the two incident beams with the long axis of the glass pipe. The simplest method actually proved the most efficient. The laser traversing system was designed to ensure that the laser transceiver was directly above the apex of the glass pipe. To align the incident beam plane with the long axis of the pipe, the beams are first roughly aligned by eye. The LDV is then enabled to collect data and as the data is being collected, the transceiver is slightly turned in either direction until the data validation rate is maximized. At this point the alignment procedure is complete.

Understanding how to work with a glass pipe as the window for a LDV is crucial in order that good data can be collected. No literature was found of previous investigations of the optical effects of lasers penetrating curved surfaces. The design engineers at Aerometrics, Incorporated stated that they knew of no studies on the optical

problems associated with curved windows. Within the LDV research community, the common practice is to use flat windows to eliminate these problems altogether or to immerse both sides of the window in a fluid with an index of refraction equal to that of the glass so that the beams never notice the curved walls of the glass view port.

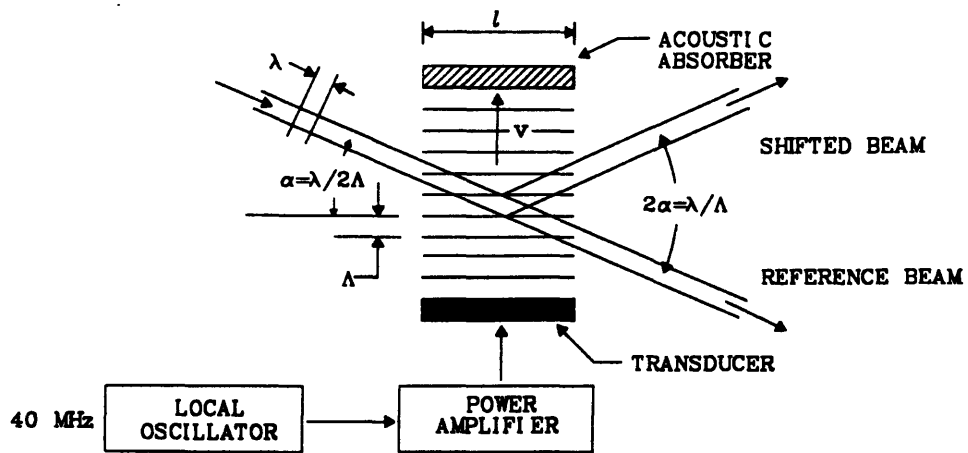


Figure 3.1 Shifting the Frequency of a Light Beam By the Use of An Acousto-Optic Bragg Cell (TSI, 1992)

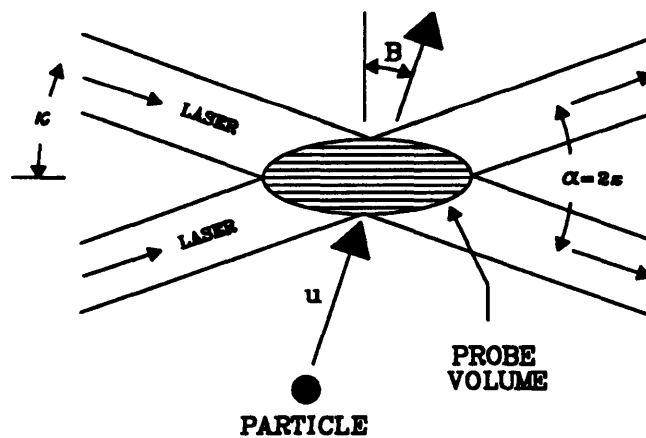


Figure 3.2 Particle Passing Through Fringe Pattern

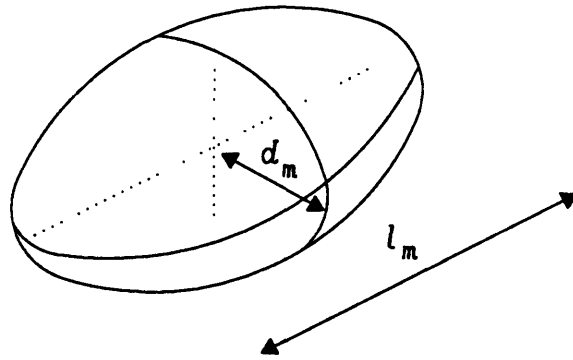


Figure 3.3 Probe Volume Dimensions

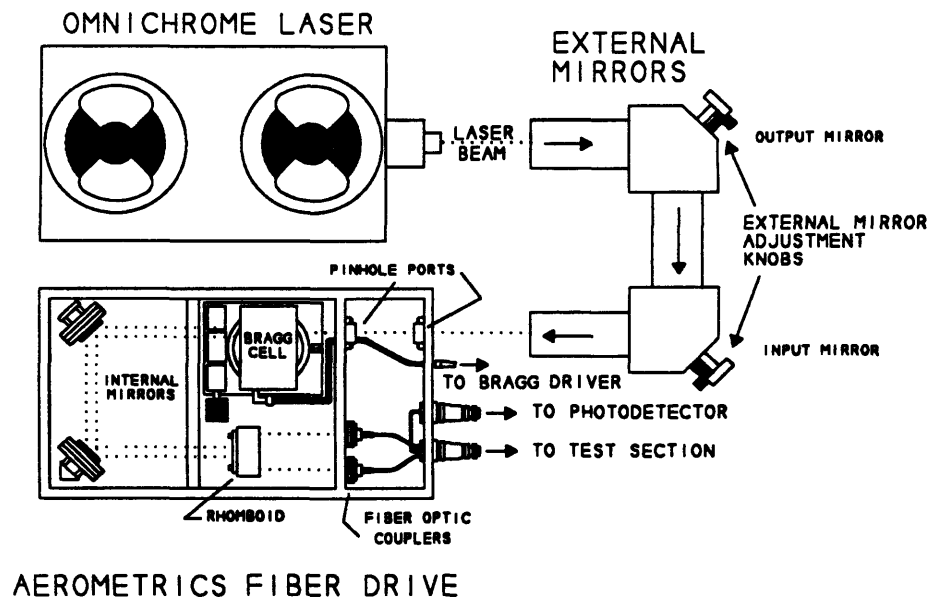


Figure 3.4 Optical System

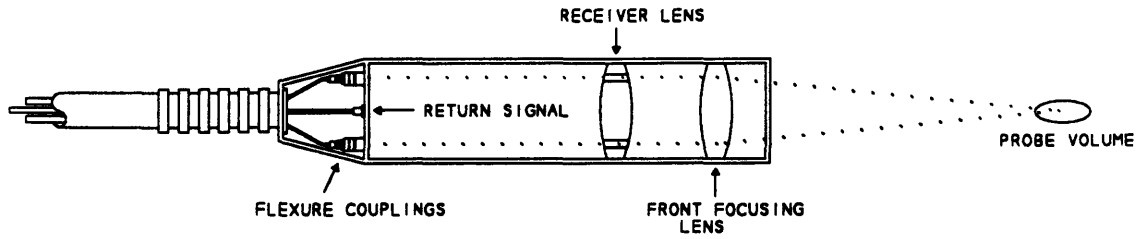


Figure 3.5 Backscatter Transceiver

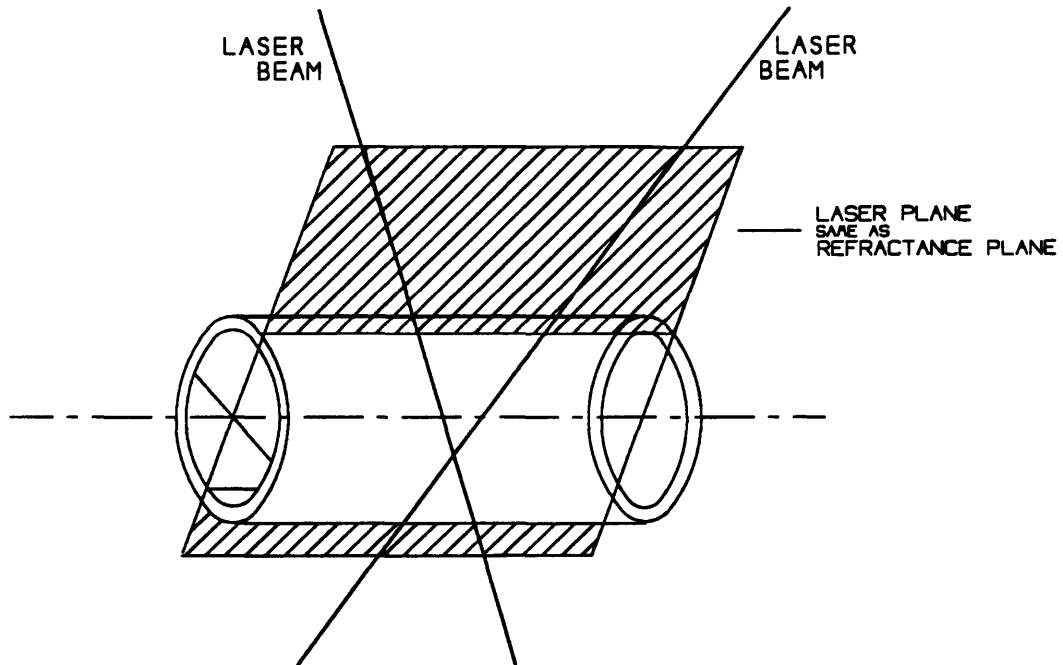


Figure 3.6 Laser Beams Properly Entering the Glass Pipe

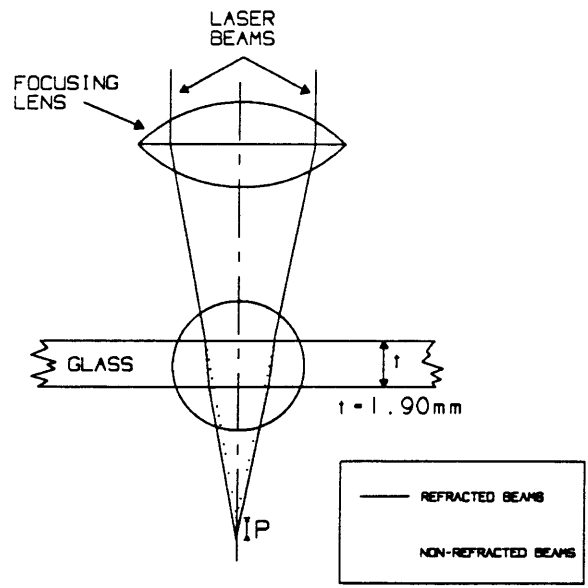


Figure 3.7 Laser Beam Refractance Due to Flat Glass Plate

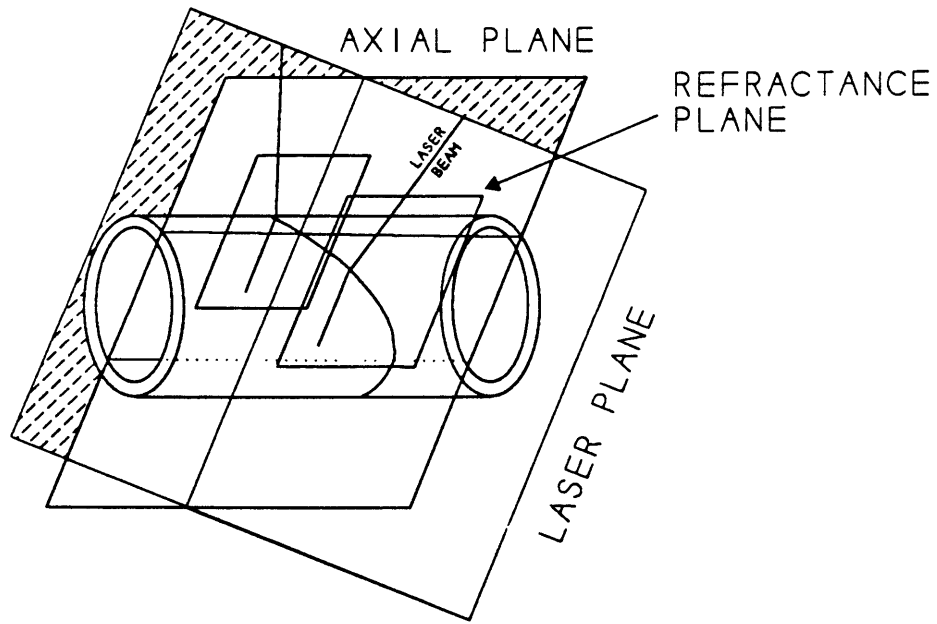


Figure 3.8 Laser Beams Not Intersecting Within the Test Section

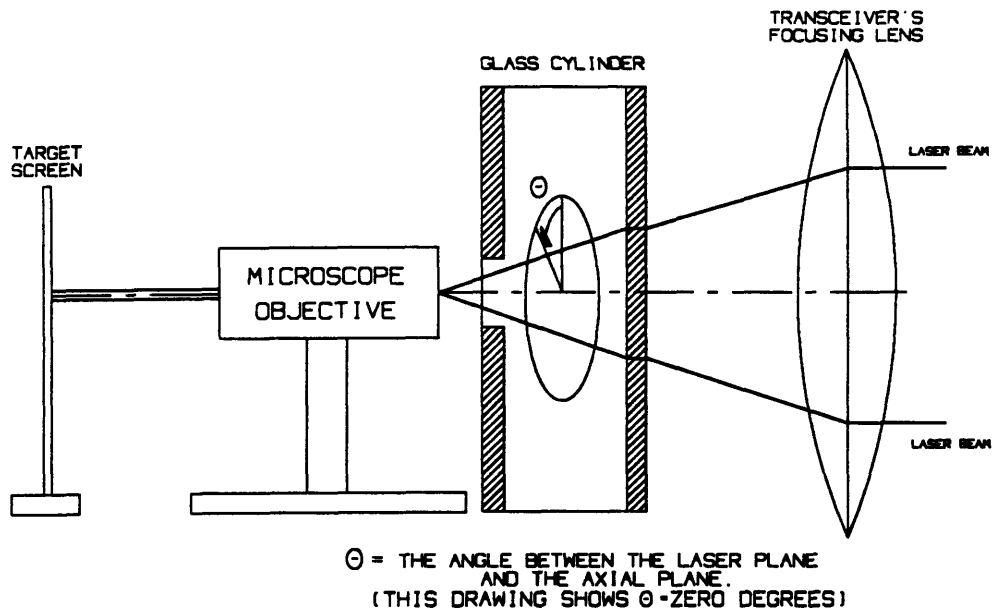


Figure 3.9 Bench Top Experiment To Investigate Beam Intersection

Chapter 4

Oscillating Flow Velocity Study

Over the last forty years, numerous research groups have studied the phenomena of oscillating flow in a pipe caused by a periodic pressure gradient. Most studies have concentrated on laminar flow or transitional flow with only a few examining the fully turbulent case. The most classical study of laminar pulsating flow was made by J.R. Womersley (1955), who examined oscillating blood flow in the arteries of animals. Womersley's work was followed by S. Uchida (1956), who expanded upon Womersley's previous analytic study to carry the theory one step further. Hino et al in 1976 used hot wire anemometry to study the transition to turbulence of oscillating pipe flow and found that turbulence occurred late in accelerating strokes and lasted until the end of the following decelerating strokes. More recently, Akhavan, Kamm, and Shapiro completed a combined analytic and experimental investigation of transitional oscillating Stokes flows (1991). Akhavan et al's study serves as an excellent example of the velocity profiles that result during transitional oscillating flow.

The purpose of our study of velocity profiles in our oscillating system is threefold. The first objective is to show that in constructing our apparatus, we had truly designed and built a symmetrical system that experienced no inlet effects from either compressor at the test section. The second objective is to compare our velocity data with the velocity profiles predicted by Uchida (1956) and White (1991) and those experimentally collected by Akhavan et al in order to see how our results agree with these previous works. The third objective is to take an initial look at when during our cycles the flow transitions to turbulence and to compare this with the earlier findings of Hino and Akhavan et al.

4.1 Flow Symmetry Within the Experimental Apparatus.

Before the LDV was incorporated into the experimental apparatus during the Phase 2 modifications, Ho and Tziranis had been unable to determine how axially symmetric the flow was within the test section. Axial flow asymmetry can result from design asymmetry at either end of the pipe containing the test section and connected to the inlet/outlet ports of the two adjacent Joy compressors. Such a design asymmetry can create non-symmetrical secondary flow patterns that enter the pipe from the two compressors and disturb the flow field within the test section. Gas leakage from anywhere within the test section or the compressors can be another cause of asymmetrical flow as gas is exhaled and inhaled into the system at varying mass flow rates. Certainly we had to ensure that our flow was axially symmetric within the test section before we could progress with a study of periodic heat transfer.

Simon and Seume (1988) provide a crucial demonstration of the importance of designing the test section so that asymmetrical entrance region effects are minimized in order to reduce their influence on the periodic heat transfer. In their experiment on oscillating heat transfer in a pipe, they found that at one end of their test section, the turbulent air exhausted with each stroke was then ingested with the following stroke. This slug of turbulent air entering the test section from only one end was found to directly influence the heat transfer process. As emphasized by their experimental results, it was crucial that our apparatus maintain a symmetrical flow of air within the test section to avoid the asymmetrical problems that Simon and Seume had to overcome.

In order to record velocity profiles across our test section, the probe volume was traversed from the inside wall of the Pyrex inner pipe closest to the transceiver to the centerline. Time history velocity data for several cycles each were recorded at numerous locations along the radius. We then assumed that the flow was radially symmetrical across the second radii of the inner diameter. Several attempts were made to record

velocity data across the full inner diameter of the glass pipe but we found that as we approached the far glass wall, the reflection of the laser beams off that wall caused too much noise and our signal was destroyed. An attempt was even made to blacken the inner surface of the far wall to prevent or reduce these reflections, but this effort did not prove sufficient to prevent the reflections from interfering with the signal.

The external input device was used to collect the crank angle position of the driven compressor as the LDV recorded velocity data. Once all the radial data was collected, it was smoothed and harmonically decomposed using the "Smoothy" program found in Appendix B, paragraph B.1. Next the "Phase" program found in Appendix B, paragraph B.4, was used to enter each of the smoothed radial data files and extract velocity data at each crank angle from 0° to 180° at 30° steps. The "Phase" program stored this information in a new data file that could be graphed using any spreadsheet type program. These files enabled us to graph velocity profiles across the radius of the pipe as the system oscillated through one cycle.

The first velocity profiles were produced for the apparatus in December 1992. These profiles are shown in Figure 4.1. The immediate concern that they raised was why does the flow in the negative direction indicate slower core velocities than the near wall velocities as compared with the flow in the positive direction. The only acceptable explanation for this asymmetry was the possible presence of a gas leak from the test section. This appeared to be the only asymmetry within the flow effecting the axial flow within the test section. Up to this point, smoke had been observed leaking out of the stuffing box located at bottom dead center of the undriven compressor. This smoke was exhausted during each compression stroke of this compressor. It was obvious that the packing within the stuffing box was leaking, but due to the bounce volume connecting the space underneath the piston in one compressor to this same space in the other compressor, it was not readily known which piston was leaking smoke past its rings. To determine which piston was leaking, the stuffing box on the driven compressor was

loosened to see if smoke was discharged along the piston rod at that end of the system. No smoke emerged. All attention was then focused on the undriven compressor.

After removing the head of the compressor as well as the piston, it was found that the two piston rings were severely worn and incapable of sealing the piston whatsoever. Additionally, it was discovered that the cylinder liner was worn at the top and bottom and formed a shallow hourglass shape. Due to the wear of the cylinder liner, replacing both piston rings with new rings would not properly seal the piston. Instead, we chose to replace one worn ring with a new ring from Joy Technologies, and replace the other worn ring with an Buna rubber O-ring. The O-ring would contract and expand with the shape of the cylinder liner to seal the piston while the new steel ring centered the piston's motion within the cylinder. Since the piston ring groove was too deep for the O-ring, Greene Rubber Company in Cambridge, MA manufactured a 0.25-inch thick rectangular ring that filled the bottom of the groove underneath the O-ring.

After the undriven compressor was reassembled, new velocity profiles were collected at $Re_w=69.36$. These profiles are shown in Figure 4.2 and clearly indicate that the flow is now axially symmetric. The maximum centerline velocity in the positive direction very closely matches the maximum centerline velocity in the negative direction at each crank angle. These excellent results demonstrate that the gas leak had been repaired and that the experiment could continue to the next stage where periodic heat transfer data would be collected.

4.2 Comparison of Velocity Data With That of Other Research Teams.

4.2.1 Uchida and White's Analytic Velocity Profiles.

In F. White's book *Viscous Fluid Flow* (1991), he provides a simplified result of S. Uchida's (1956) solution to the Navier-Stokes' equation for laminar flow in a pipe with

an oscillatory pressure gradient. White initiates his solution of Uchida's earlier work by repeating Uchida's first step in writing the Navier-Stokes' equation in cylindrical coordinates:

$$\frac{\partial u}{\partial t} + u \frac{\partial u}{\partial x} + v \frac{\partial u}{\partial r} = -\frac{1}{\rho} \frac{\partial p}{\partial x} + \nu \left(\frac{\partial^2 u}{\partial x^2} + \frac{\partial^2 u}{\partial r^2} + \frac{1}{r} \frac{\partial u}{\partial r} \right) \quad (4.1)$$

$$\frac{\partial v}{\partial t} + u \frac{\partial v}{\partial x} + v \frac{\partial v}{\partial r} = -\frac{1}{\rho} \frac{\partial p}{\partial r} + \nu \left(\frac{\partial^2 v}{\partial x^2} + \frac{\partial^2 v}{\partial r^2} + \frac{1}{r} \frac{\partial v}{\partial r} - \frac{v}{r^2} \right) \quad (4.2)$$

Both White and Uchida then assumed that the flow was unidirectional along the x axis of the pipe which resulted in no radial (v) component of velocity. The continuity equation simplified to:

$$\frac{\partial u}{\partial x} + \frac{\partial v}{\partial r} + \frac{u}{r} = 0 \Rightarrow \frac{\partial u}{\partial x} = 0 \quad (4.3)$$

and they wrote:

$$u = u(r, t) \quad (4.4)$$

Uchida noted that having a velocity in only the x direction was an assumption valid solely for fully developed laminar flow. When he substituted v=0 into his Navier-Stokes' equations, he found that pressure is uniform across the cross section of the pipe and is only a function of x location and time. With these simplifications, Uchida was left with the following differential equation:

$$\frac{\partial u}{\partial t} = -\frac{1}{\rho} \frac{\partial p}{\partial x} + \nu \left(\frac{\partial^2 u}{\partial r^2} + \frac{1}{r} \frac{\partial u}{\partial r} \right) \quad (4.5)$$

White assumed at this point that the pressure gradient is sinusoidal and could be expressed as:

$$-\frac{1}{\rho} \frac{\partial p}{\partial x} = K \cos \alpha x \quad (4.6)$$

where K is a constant and equals:

$$K = \frac{u_{\max}(4\nu)}{R}$$

White then produced the following solution to Uchida's Equation 4.5:

$$u(r,t) = \frac{K}{i\omega} e^{i\omega t} \left[1 - \frac{J_0\left(r \sqrt{\frac{-i\omega}{\nu}}\right)}{J_0\left(R \sqrt{\frac{-i\omega}{\nu}}\right)} \right] \quad (4.7)$$

where he uses the following nondimensional terms:

$$r^* = \frac{r}{R}; \quad Re_\omega = \frac{\omega R^2}{\nu}; \quad u^* = \frac{u}{u_{\max}}$$

When White simplified Uchida's Bessel function he found that for:

$Re_\omega < 4$:

$$u^* = (1 - Re_\omega^2) \cos \alpha x + \frac{Re_\omega}{16} (r^{*4} + 4r^{*2} - 5) \sin \alpha x + \vartheta(Re_\omega^2) \quad (4.8)$$

$Re_\omega > 4$:

$$u^* = \frac{4}{Re_\omega} \left[\sin \alpha x - \frac{e^{-B}}{\sqrt{r^*}} \sin(\alpha x - B) \right] + \vartheta(Re_\omega^{-2}) \quad (4.9)$$

where the higher order terms, $\vartheta()$, can be neglected to produce an even simpler result.

White defined a nondimensional distance from the wall as B which equals:

$$B = (1-r^*) \sqrt{\frac{Re_{\omega}}{2}}$$

By using White's simplified solution of Uchida's solution and the "White" program found in Appendix B, paragraph B.5, oscillating velocity profiles are graphed in Figures 4.4, 4.5, and 4.6 for selected crank angles at three differing frequencies. We can see that at a low frequency of 0.005 Hz and $Re_{\omega}=1.0$, the flow resembles Poiseuille flow because the pressure gradient is in phase with the flow (White, 1991, pp 135-136). As we increase the frequency to 0.151 Hz and $Re_{\omega}=30.0$, we see that the flow begins to slow down in the center as compared to the wall region and that back flow occurs for the first time around 150° where there is a velocity inversion in the center as compared to the wall flow inside the viscous boundary layer. As we further increase the frequency to 5.0 Hz and $Re_{\omega}=991$, our flow now trails the pressure gradient by 90° (White, 1991, pp 135-136). It is of interest to note that as the frequency increases, the centerline velocity decreases due to the flow reversing too quickly for it to have a chance to fully develop in either positive or negative x-direction.

4.2.2 Experimental Studies by Hino et al and Akhavan et al.

Hino et al (1976) conducted an experimental study of the transition to turbulence of a periodic gas flow in a pipe using a hot wire anemometer and found that the flow transitions to turbulence late in each acceleration stroke where turbulent bursts suddenly and violently occur close to the peak velocity of that stroke. This turbulence continues during each deceleration stroke until close to the end of that stroke where it dies out only to return again with great energy late in the next accelerating stroke. Figure 4.7 illustrates this occurrence for what Hino et al classify as conditionally turbulent flow (n in the figure

refers to the radial position and $n=0$ is the centerline of the pipe). We can clearly see the appearance of these turbulent bursts within the cycle.

Akhavan, Kamm, and Shapiro examined a liquid flow's transition to turbulence with a LDV as the fluid oscillated within a pipe. They found experimentally that for laminar flow, their results agreed well with Womersley (1955) and Uchida (1956) as depicted earlier with White's oscillating velocity profiles (Fig.4.4). As the stream transitioned to turbulence, however, Akhavan et al's results quickly departed from White's profiles and the back flow along the wall was no longer pronounced. As did Hino et al, Akhavan et al found that the stream transitioned from laminar to turbulent flow late in the acceleration phase and remained turbulent though the majority of the deceleration phase of every cycle. Akhavan then predicted that the laminar accelerating flow behaves more as flow undergoing start-up from rest of an oscillating flow in a pipe than what Womersley and Uchida had predicted with their solution modelling continuously oscillating flow (Akhavan et al, 1991, pg. 401). Figure 4.8 illustrates the difference between Akhavan et al's data (shown with empty circle symbols) and Uchida's laminar theoretical profiles (Akhavan et al, 1991). For their study, Akhavan et al used the following nondimensional parameters:

$$Re^{\delta} = \frac{U_0 \delta}{\nu} \quad \text{and} \quad \Lambda = \frac{R}{\delta}$$

where U_0 is the cross-sectional mean velocity and R is their pipe radius which was 2.0 cm.

4.2.3 Comparison of Experimental Velocity Profiles with Previous Findings.

In order to compare our results with those predicted by White and Uchida's laminar theory solutions as well as the experimental results generated by Akhavan et al, we produced the velocity profiles at $Re_{\omega}=69.52$ already shown in Figure 4.2. The

frequency (0.35 Hz) of this run was chosen because it was the minimum RPM for our apparatus and would most closely approach laminar flow. We can clearly see in comparing Figure 4.2's profiles with White's profiles in Figures 4.4, 4.5, and 4.6 that even our slowest flow is much more turbulent than White's model in Figure 4.6 despite our Re_w being much smaller than White's in this case. Our results clearly indicate that within our turbulent flow no backflow along the wall occurs as White and Uchida had predicted with laminar theory. Consequently, our profiles in Figure 4.2 closely correspond with the nondimensional profiles generated by Akhavan et al in Figure 4.8.

4.3 Initial Examination of the Onset of Turbulence Within the Experimental Apparatus.

Only a preliminary investigation was undertaken to see when the flow within the experimental apparatus transitioned to turbulence. Further work in this area needs to be completed to better understand the phenomena and how the onset of turbulence effects the heat transfer.

At the time when the first velocity profiles were collected in December 1992, the oscillating velocity plots at each location across the test section showed that the spiked appearance of turbulence during a cycle appeared and disappeared symmetrically about the peak of the velocity fluctuations in both positive and negative directions as depicted in Figure 4.9. This arrival and departure of turbulent bursts did not agree with the data collected by Hino et al (1976) nor Akhavan et al (1991). As mentioned previously, these two other research groups found that turbulence bursts occurred violently toward the end of the acceleration stroke and did not diminish until late in the following deceleration stroke. The only explanation for the difference of our results was the same gas leak that was effecting the symmetrical flow pattern.

After the undriven piston was repaired as previously described, new time history velocity data were collected in the test section. Figure 4.10 was generated from data collected after the piston leak was repaired. This figure shows that indeed the turbulence occurs late in the acceleration stroke and remains until late in the deceleration stroke which is further emphasized by Figure 4.11 which graphs the smoothed velocity curve against turbulent bursts which were determined by subtracting the same smoothed data from the raw velocity data. The removal of the leak enabled our results to agree with those found by both Hino and Akhavan and signalled that we were ready to undertake the study of periodic heat transfer.

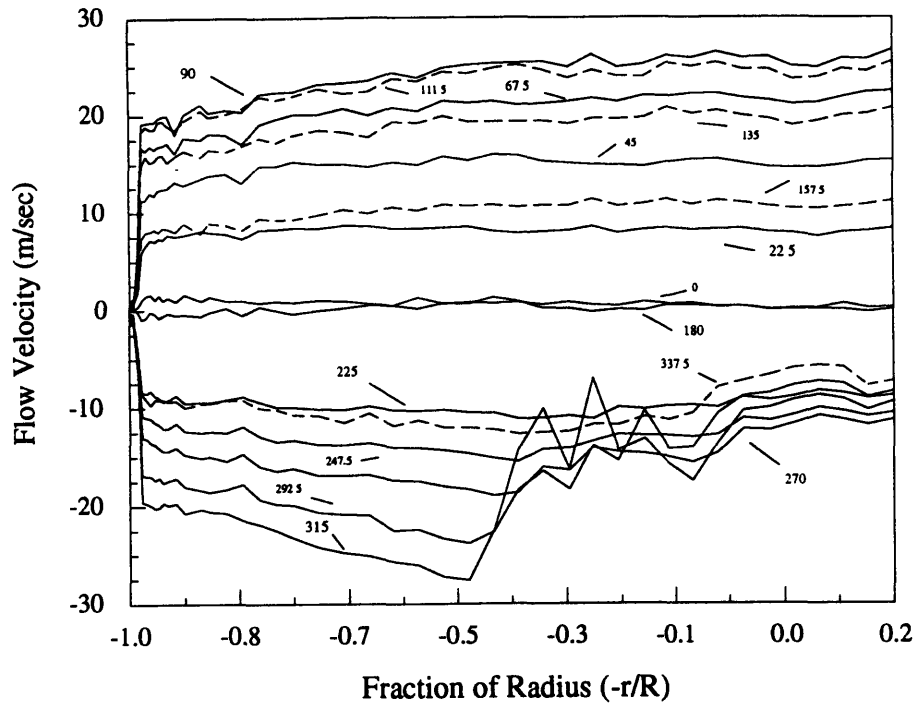


Figure 4.1 Initial Velocity Profiles at $Re_{\omega}=69.36$, $\Psi=180^{\circ}$

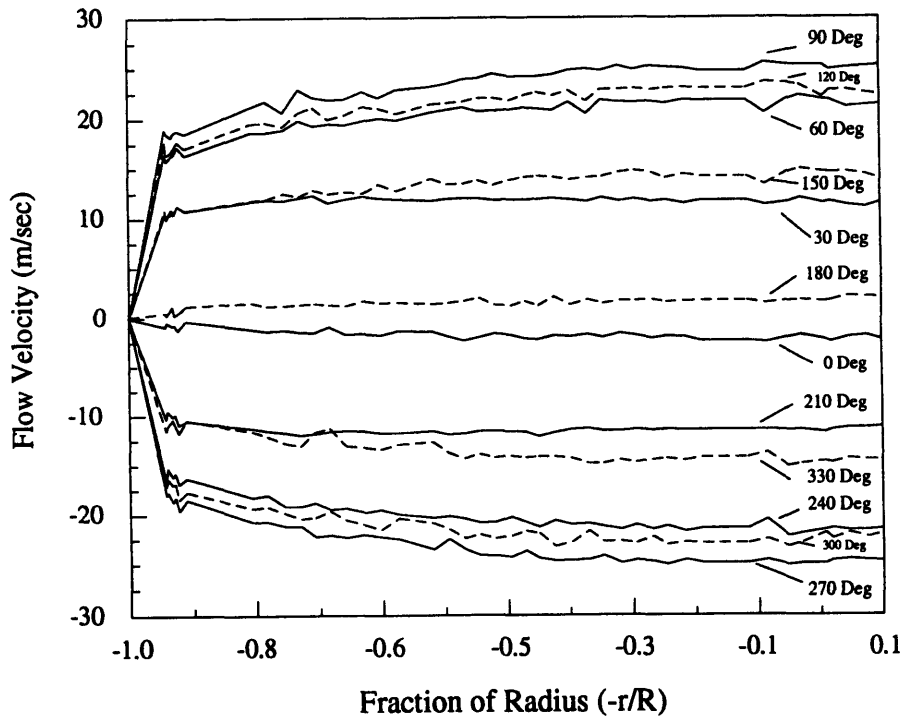


Figure 4.2 Improved Instantaneous Velocity Profiles at $Re_{\omega}=69.52$, $\Psi=180^{\circ}$

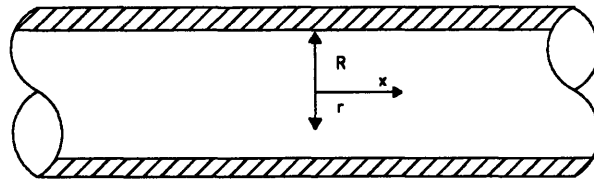


Figure 4.3 Coordinate System for a General Pipe

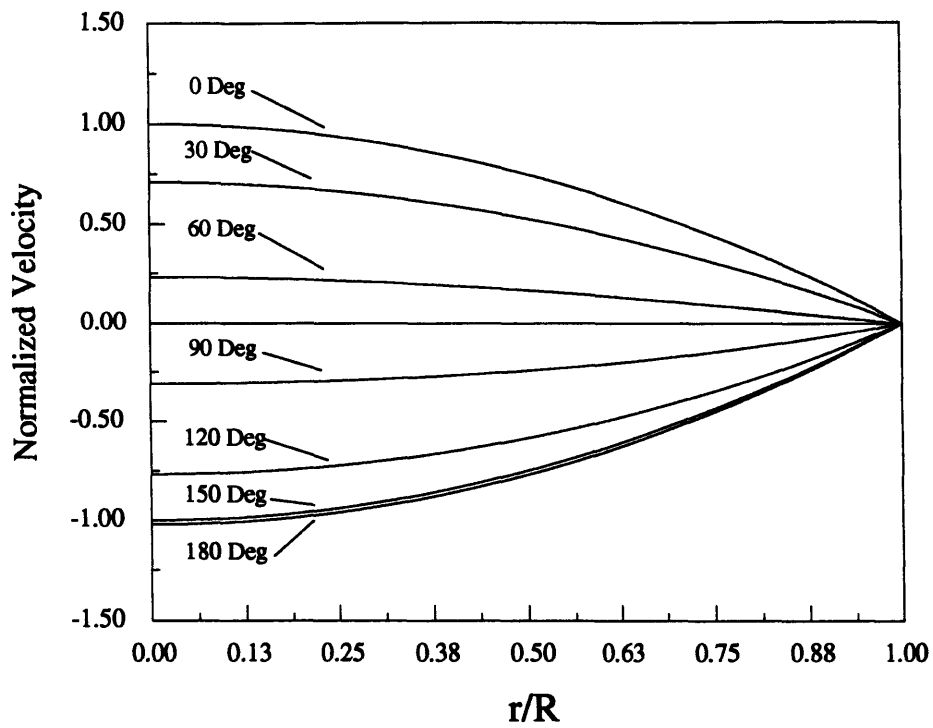


Figure 4.4 Laminar Theoretical Profiles, $f=0.005$ Hz, $Re_{\omega}=1.0$

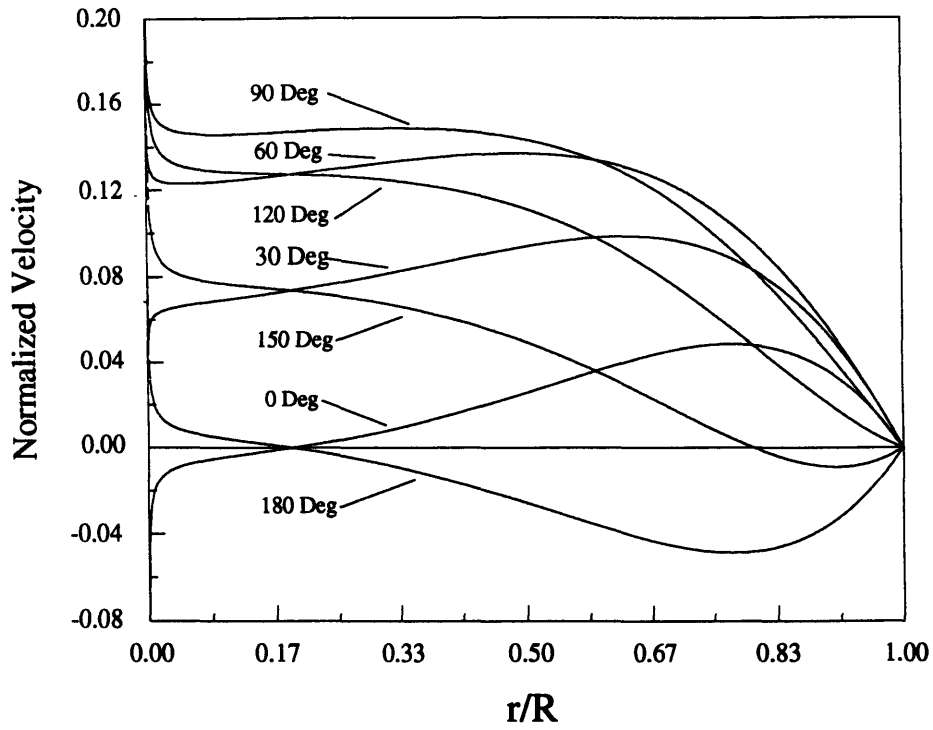


Figure 4.5 Laminar Theoretical Profiles, $f=0.151$ Hz, $Re_{\omega}=30.0$

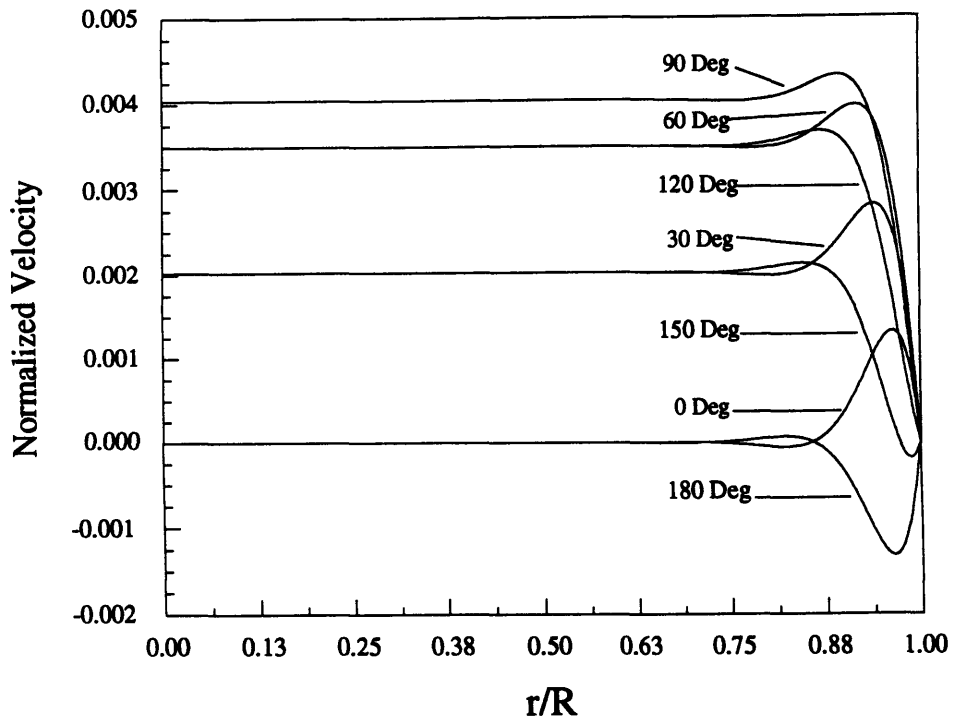


Figure 4.6 Laminar Theoretical Profiles, $f=5.0$ Hz, $Re_{\omega}=991$

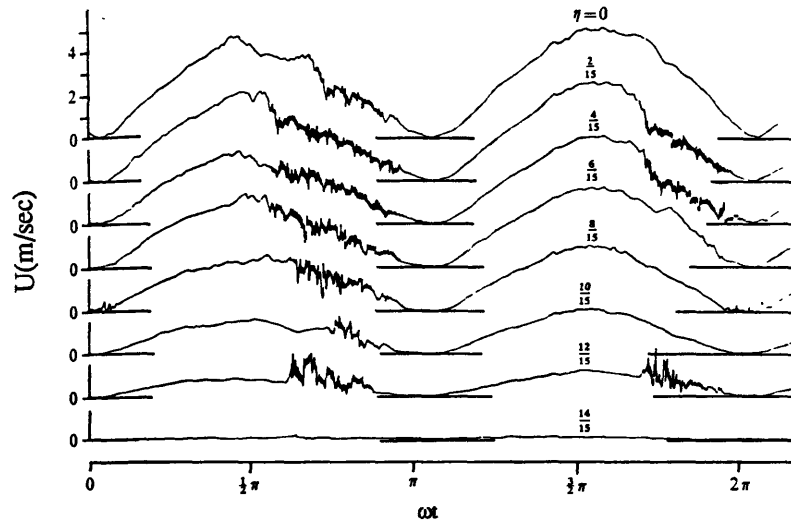


Figure 4.7 Hino's Oscillating Velocity Time History at $f=0.33$ Hz, $Re_\omega=0.0344$, $D=.00145$ m

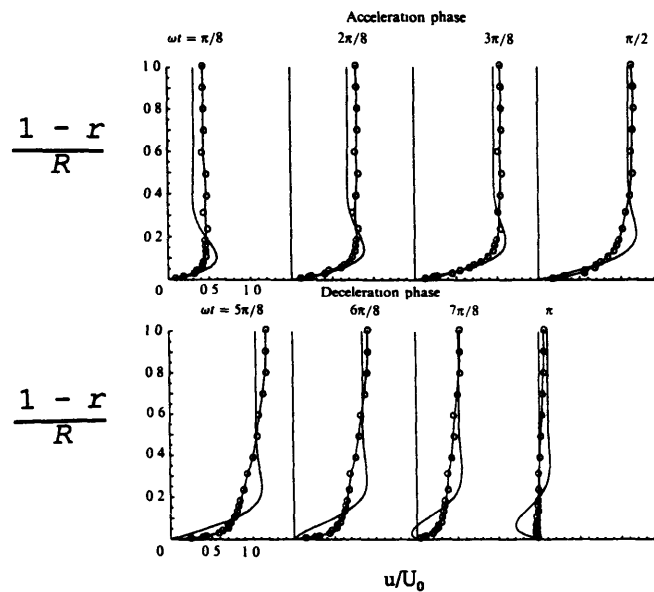


Figure 4.8 Akhavan et al's Oscillating Velocity Profiles at $Re_\delta=1080$ and $\Lambda=10.60$

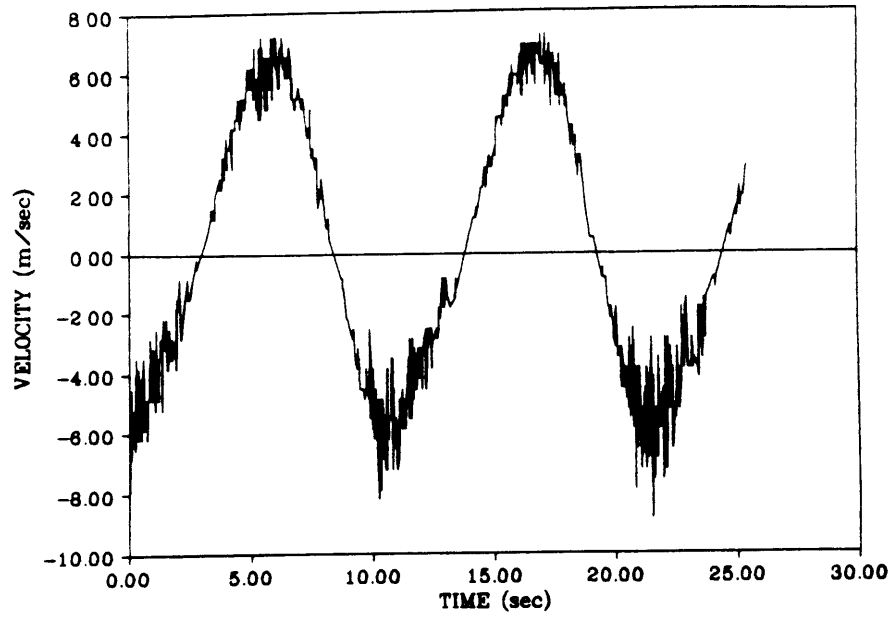


Figure 4.9 Initial Centerline Periodic Velocity, $Re_{\omega}=15.85$, $\Psi=180^{\circ}$

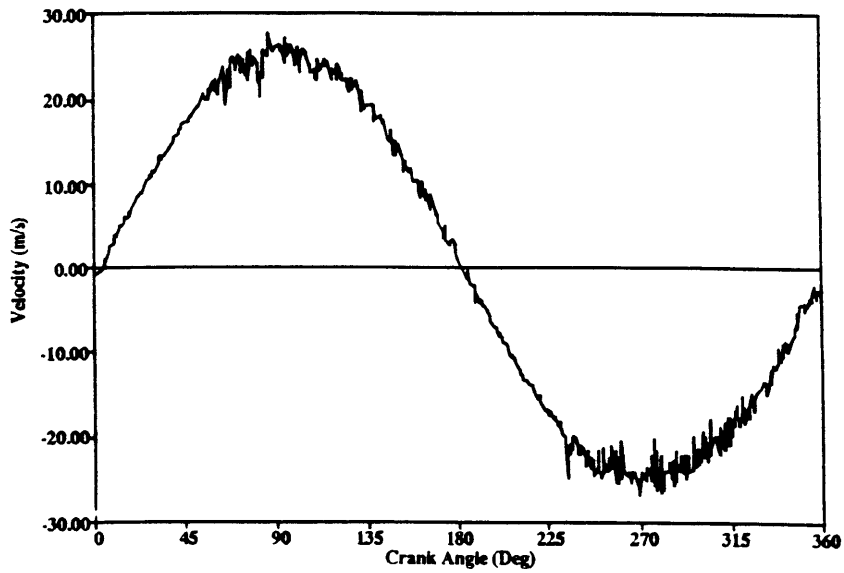


Figure 4.10 Corrected Centerline Periodic Velocity, $Re_{\omega}=69.52$, $\Psi=180^{\circ}$

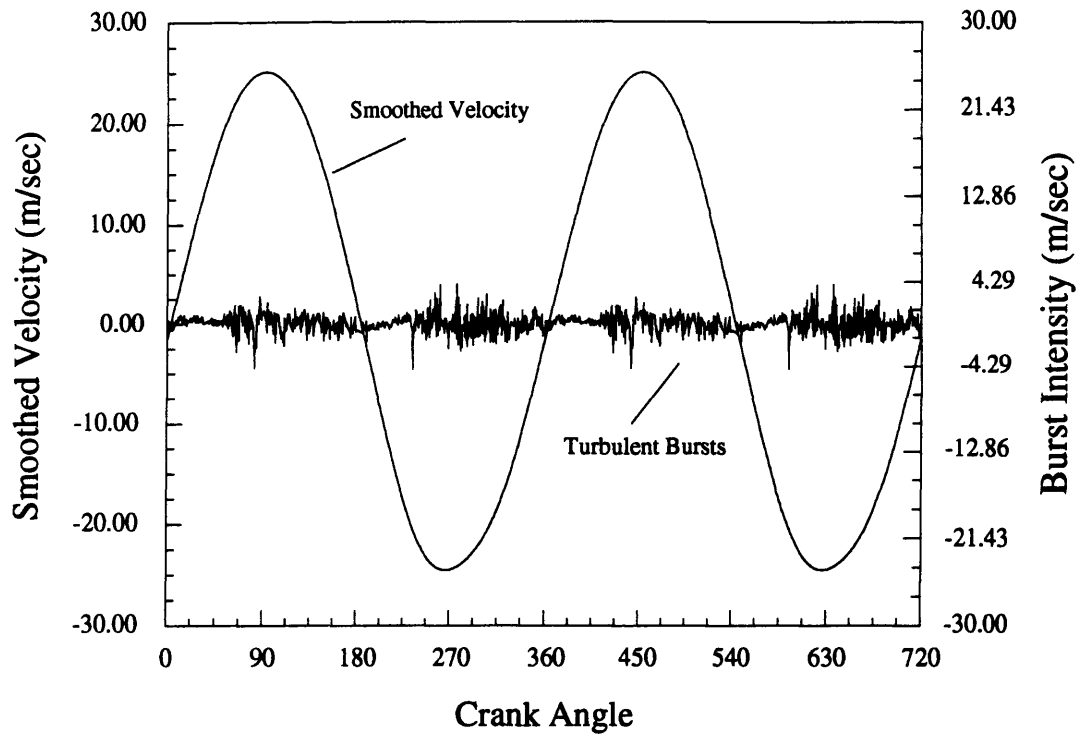


Figure 4.11 Turbulent Bursts at Centerline, $Re_{\omega}=69.52$, $\Psi=180^{\circ}$

Chapter 5

Experimentally Determined Heat Transfer Under Conditions of Oscillating Pressure and Flow

In 1991, Ho recorded baseline heat transfer data for the Phase 1 experimental apparatus. His correlations for complex Nusselt numbers and related phase shifts between heat flux and ΔT were obtained by first collecting pressure, wall temperature, centerline temperature, and crank angle data and then using this with the first law of thermodynamics to obtain the heat transferred from the gas to the wall of the test section.

$$\text{First Law } \oint \delta Q = -PdV - dU \quad (5.1)$$

(where heat and work are (+) out the system)

Ho's solution for the complex Nusselt numbers followed Kornhauser's approach (1989). As a result, his baseline data and related heat flux, complex Nusselt numbers, and phase shift between heat flux and ΔT are the product of a combination of real data and fundamental thermodynamic equations for an ideal gas. It can only be assumed that the gas leak (Chap. 4) past the piston rings in the undriven compressor was present during Ho's experiments and may have effected his baseline data.

The Phase 2 and Phase 3 improvements to the apparatus have eliminated the need to solve any equations for the heat transfer. The resulting complex-valued Nusselt numbers and the phase shifts between heat flux and ΔT are highly reliable and will greatly assist in code development for predicting this type of heat transfer.

5.1 Revised Complex Nusselt Number Model.

To develop the means of correlating the heat flux to determine the complex-valued Nusselt number and the phase shift between heat flux and ΔT , we shall proceed by a

loose analogy to AC circuit theory. In reactive AC systems, voltage and current (V and I) are out of phase, yet they can be represented by complex-valued phasors related by a complex-valued admittance ($I=YV$). In our case, heat flux takes the role of current, while temperature difference ($T_{CL}-T_w$) takes the role of voltage. The heat transfer coefficient is an admittance. Since admittance is generally frequency dependent, we expect that the appropriate heat transfer coefficient will not only be complex-valued, but will also take on a different value for each harmonic of the flow.

In complex form, convective heat flux can be written as:

$$q_c = h_c \Delta T_c \quad (5.2)$$

In terms of the complex Nusselt number this becomes:

$$q_c = \frac{k}{D} Nu_c \Delta T_c \quad (5.3)$$

In order to solve for the complex Nusselt number, the complex heat flux and the complex temperature difference between the bulk gas temperature and the wall temperature are expressed in the following harmonic forms:

$$q_c = \sum_{n=0}^N q_n \cos(2\pi n\omega t - \phi_{q_n}) = \sum_{n=0}^N q_n e^{i(2\pi n\omega t - \phi_{q_n})} \quad (5.4)$$

($q_c > 0$ denotes heat transfer to the wall)

$$\Delta T_c = T_{CL} - T_w = \sum_{n=0}^N \Delta T_n \cos(2\pi n\omega t - \phi_{T_n}) = \sum_{n=0}^N \Delta T_n e^{i(2\pi n\omega t - \phi_{T_n})} \quad (5.5)$$

where for each harmonic we can write:

$$h_{c_n} = \frac{q_{c_n}}{\Delta T_{c_n}} = \frac{q_n e^{i(2\pi\alpha t - \phi_{qn})}}{\Delta T_n e^{i(2\pi\alpha t - \phi_{Tn})}} = \frac{q_n}{\Delta T_n} e^{-i(\phi_{qn} - \phi_{Tn})} \quad (5.6)$$

Note that q_n , ϕ_{qn} , ΔT_n , and ϕ_{Tn} are obtained by harmonic decomposition of our measurements. With these definitions, we can solve for the complex heat transfer coefficient, h_{c_n} , for each harmonic:

$$\text{where } h_{c_n} = h_{r_n} + ih_{i_n}$$

$$h_{c_n} = \frac{q_n}{\Delta T_n} \cos(\phi_{qn} - \phi_{Tn}) + i \frac{q_n}{\Delta T_n} \sin(\phi_{qn} - \phi_{Tn}) \quad (5.7)$$

Our last step is to solve for the complex Nusselt number:

$$Nu_{c_n} = \frac{D}{k} h_{c_n} \quad (5.8)$$

This complex Nusselt number can be written as a sum of its real and imaginary parts:

$$Nu_{c_n} = \frac{D}{k} \left[\frac{q_n}{\Delta T_n} \cos(\Delta\phi_n) + i \frac{q_n}{\Delta T_n} \sin(\Delta\phi_n) \right] \quad (5.9)$$

$$\text{where the } n\text{-th harmonic phase shift is } \Delta\phi_n = \phi_{qn} - \phi_{Tn}$$

A negative $\Delta\phi_n$ denotes heat flux leading ΔT , whereas a positive $\Delta\phi_n$ indicates the opposite. These harmonically decomposed equations for complex heat transfer and complex Nusselt number were first derived by Yagy and Smith (1991) and provide a means of determining for each harmonic the magnitude of the complex Nusselt number and its associated phase angle through smoothing and Fourier transformation of the experimental heat flux and ΔT data.

We can express any Fourier series in the following form, where C is any quantity:

$$C = a_0 + \sum_{n=1}^N a_n \cos n\phi + \sum_{n=1}^N b_n \sin n\phi \quad (5.10)$$

The "Smoothy" program in Appendix B, paragraph B.1, determines the Fourier series coefficients for all measured data. Once the heat flux and ΔT Fourier series coefficients are known for each of the first five harmonics, we can write each of the harmonic series for these dependent variables in the following phasor form:

$$C(n) = Amp_n (\cos 2\pi n\omega t \pm \phi_{Cn}) \quad (5.11)$$

We can determine the amplitude Amp_n for each harmonic and the phase angle ϕ_n for each harmonic in the following manner:

$$Amp_n = \sqrt{a_n^2 + b_n^2} \quad (5.12)$$

$$\text{and } \phi_{Cn} = \tan^{-1} \left[\frac{b_n}{a_n} \right] \quad (5.13)$$

The "Nuc1" program in Appendix B, paragraph B.2, takes the values of the amplitudes and phase angles for each of the five harmonics for heat flux and ΔT and first converts their phasor equations to the following exponential form:

$$C(n) = Amp_n e^{-i(2\pi n\omega t \pm \phi_{Cn})} \quad (5.14)$$

which yields:

$$q(n) = q_n e^{i(2\pi n\omega t - \phi_q)} \quad (5.15)$$

$$\Delta T(n) = \Delta T_n e^{i(2\pi n\omega t - \phi_{Tn})} \quad (5.16)$$

and then computes the complex-valued Nusselt through simple arithmetic:

$$Nu(n) = \frac{D \left[\frac{q(n)}{\Delta T(n)} \right]}{k} = \frac{D \left[\frac{q_n}{\Delta T_n} \right]}{k} e^{-i(\phi_q - \phi_T)} \quad (5.17)$$

This form yields for each of the five harmonics the real and imaginary components of the complex Nusselt number as well as the phase shift between heat flux and ΔT :

$$(Nu_n)_r = \frac{D \left[\frac{q_n}{\Delta T_n} \right]}{k} \cos(\phi_{q_n} - \phi_{T_n}) \quad (5.18)$$

$$(Nu_n)_i = \frac{D \left[\frac{q_n}{\Delta T_n} \right]}{k} \sin(\phi_{q_n} - \phi_{T_n}) \quad (5.19)$$

and finally for each harmonic we can write:

$$Nu_c = \sqrt{(Nu_r)^2 + (Nu_i)^2} \quad (5.20)$$

$$\text{where } \phi_n = \phi_{q_n} - \phi_{T_n}$$

as was defined with Equation 5.9.

5.2 Experimental Procedure for Collecting Baseline Heat Transfer Data.

The initial step in acquiring the baseline data was to apply power to the auto transformer connected to the 25 HP DC motor as well as to the air compressor, the laser Doppler velocimeter, and the instrumentation. The air compressor supplied house air at 120 psi to the pressure regulator attached to the mineral oil smoke generator which limited the pressure to 40 psi. The instruments and the laser were given at least thirty minutes to warm up before they were calibrated for data collection. The laser and each

data acquisition instrument needed time to settle once they were turned on. Half an hour was found to be sufficient.

After the warmup period, each instrument was checked to ensure that it was properly calibrated to measure its respective ambient reading prior to the DC motor being turned on. The resistance temperature device (RTD) measuring the wall temperature, was checked for its output voltage at room temperature. The room temperature was first measured with an alcohol thermometer that measured in degrees centigrade. This temperature was converted to degrees Fahrenheit and then the RTD's calibration equation was solved backwards for voltage:

$$RTD \text{ Output Voltage} = \frac{Room \text{ Temp } [^{\circ}F]}{13.1333} \quad (5.21)$$

where

$$^{\circ}F = \frac{9}{5}^{\circ}C + 32$$

With this voltage known, the potentiometer associated with the RTD's amplifier was adjusted so that the output voltage from the amplifier (read with a multimeter) equalled the same quantity.

The Kulite pressure transducer was checked to ensure that it was reading zero gage pressure at ambient conditions. The output voltage from the pressure transducer's amplifier was converted to psi using the following polynomial:

$$P_{gage} = (-0.00104)V^2 + (5.671395)V + 34.06621 \quad (5.22)$$

where V is the output voltage. Due to the -6 volt offset given by the amplifier's 200 gain, the potentiometer was adjusted to read -6 volts on the multimeter. Output voltages could then be converted to absolute pressures [kPa] in the following manner:

$$P = \left[P_{gauge} + \frac{P_{baro}(14.696 \text{ psia})}{(29.92 \text{ in Hg/atm})} \right] \left(\frac{6.895 \text{ kPa}}{1 \text{ psia}} \right) \quad (5.23)$$

The ambient pressure P_{baro} was read off an analog engineers' barometer.

The RdF heat flux sensor was calibrated at the factory for a wall temperature of 70°F. For wall temperatures above or below 70° F, the output of the gage is calibrated by multiplying by a factor associated with the room temperature as depicted in Figure 5.1. The equation for this curve is:

$$\text{Calibration Factor} = K + AT + BT^2 + CT^3 + DT^4 + ET^5 \quad (5.24)$$

where

$$\begin{aligned} K &= 1.1 \\ A &= -1.59946 \times 10^{-3} \\ B &= 2.77577 \times 10^{-6} \\ C &= -4.28754 \times 10^{-9} \\ D &= -9.08604 \times 10^{-12} \\ E &= 2.95572 \times 10^{-14} \end{aligned}$$

For the baseline experiments the sensor's amplifier was set to a gain of 10,000 by cascading the output signal through two amplifiers, one set for a gain of 1000 and the next set for a gain of 10. Heat flux voltage measurements were converted to W/m^2 with the following equation:

$$q = \frac{(\text{Output Voltage})}{(A \times 10^{-6} \frac{\text{Volts}}{\text{BTU/ft}^2\text{hr}})} \cdot (3.155 \frac{\text{W/m}^2}{\text{BTU/ft}^2\text{hr}}) \cdot (\frac{1}{\text{Gain}}) \quad (5.25)$$

where "A" is RdF's sensor calibration constant supplied with each sensor. A is always close to 0.20. Due to the large amplifications associated with these heat flux measurements, the sensors tend to collect 60 Hz background noise of equipment within the laboratory. The sensors must therefore be carefully grounded to prevent this noise from degrading the quality of the data.

The Beckman Type E traversing thermocouple was checked to ensure that the resistance across the two leads coming directly off the thermocouple read close to 132 Ohms which ensured that both the instrument was working and that it was calibrated with the standard Type E thermocouple polynomials. The thermocouple's output voltages were converted to degrees centigrade in the following manner:

$$T = -5.7670 \times 10^{-5} V^4 + 5.4809 \times 10^{-3} V^3 + -0.2210 V^2 + 17.0225 V \quad (5.26)$$

where V is again the output voltage of the instrument measured after amplification by a multimeter. For all baseline measurements, the thermocouple was stationed at the geometric center of the test section to read centerline temperatures. Due to the turbulent mixing in the flow, the centerline temperature was assumed to be nearly equal to the mixed mean temperature.

The laser was the last instrument to be prepared before data was collected. It was essential that the two beams emitting from the transceiver generated the same amount of power. Their individual power levels were adjusted both at the fiber optic coupler within the fiber drive and with the Bragg cell driver using its carrier control knob. Each beam emitting from the transceiver was first checked with the power meter to ensure that it was at its maximum power by carefully adjusting its fiber optic coupler (see App. A.2) and monitoring the power meter. When both beams were maximized at their respective fiber optic coupler, the Bragg cell driver was adjusted so that the beams had equal power in respect to one another as indicated on the power meter. Aerometrics engineers found that upon emitting from the transceiver, these beams once properly adjusted should balance around 12 mW each. For baseline data, the point of intersection of these two beams was set to the geometric center of the test section.

With all instruments set for data collection, the compressor phase angle Ψ was adjusted for the experiments. This was done by first loosening the bolts on the shrink disks at the driven compressor end of the drive tube, thus freeing the driven compressor inertial sheave from the undriven compressor's inertial sheave (Fig. 5.2). With the motion

of the two compressors free of one another, the undriven compressor was set to bottom dead center by turning its inertial sheave until a dial indicator touching the crosshead showed that the crosshead was as low as possible. Next the software for the Digital Signal Analyzer (DSA) was turned on and set to the Alt-F2 page for monitoring the signals coming into the External Input device. Here the count coming from the optical shaft encoder on the driven compressor's crank shaft could be read (1200 counts/360°) as the driven compressor's inertial sheave was turned by hand. This sheave was then rotated until the appropriate compressor angle Ψ was attained. The driven compressor was always set to lead the undriven compressor. Once both compressors were properly aligned, the bolts on the shrink discs were re-tightened to 50 foot-pounds torque.

At this point the only remaining step to be taken before the DC motor could be started was to seed the LDV. Smoke from the mineral oil smoke generator was passed through the test section from the undriven end to the driven end. Once smoke discharged from a valve connected to the head of the driven compressor, the smoke generator was turned off. It was important to not over seed the flow and at times it was essential that smoke be released from the test section in order to collect particle velocity data. Smoke line valves were closed to prevent these 3/8-inch copper smoke lines from adding to the dead volume of the experiment.

The DC motor was next turned on and its voltage was set on the auto transformer. The frequency of a run depended upon the belt setting coming off the output shaft of the motor as well as the motor's applied voltage. These belts have two settings. The low belt setting was capable of producing piston frequencies ranging between 0.08 and .98 Hz. The approximate frequency for a particular voltage applied in the low belt mode can be determined by:

$$f = [0.52693 + (0.20385)Volts] \cdot \left(\frac{1 \text{ Hz}}{60 \text{ RPM}} \right) \quad (5.27)$$

The high belt setting is in turn capable of producing piston frequencies between 1.5 and 8.25 Hz. In the high belt mode, the approximate frequency for a particular voltage setting is:

$$f = [-10.352 + (2.1334) \text{ Volts}] \cdot \left(\frac{1 \text{ Hz}}{60 \text{ RPM}} \right) \quad (5.28)$$

The actual frequencies for a particular voltage setting were determined after one set of data was collected and the DSA's software had a chance to perform a fast Fourier transformation (FFT) of the data. At times, this FFT was the best method to determine whether or not velocity data was acceptable or rendered useless by noise.

The data was recorded by making two collection runs at each voltage setting for a particular compressor phase angle. For the first run the pressure transducer's BNC was connected to Channel 2 of the external input device. The heat flux sensor's BNC was connected to Channel 3 and Channel 1 always recorded the optical encoder position. The DSA software was then adjusted to record clean velocity measurements for at least two cycles, preferably with several hundred data points per cycle. This data was then saved. The pressure transducer's BNC was replaced with the traversing thermocouple's BNC and the heat flux sensor's BNC was exchanged with the wall RTD's BNC. A second set of data was collected at this point for at least two cycles and once again this data was saved. After all data was collected for a particular voltage, the auto transformer was adjusted to the next desired voltage at which point the data collection procedure was repeated. When all data had then been taken for a compressor phase angle, the phase angle was changed for the next set of data. If it were found that the compression ratio for a particular compressor phase angle setting was not producing compression ratios close to 2.0, then the ratio would be corrected by adjusting the variable volumes attached to the head of each compressor. For Ψ equal to 0° , 45° , and 90° the variable volumes at valve ports 1 were left fully open and those at valve ports 4 were left fully closed (Fig. 5.3). For $\Psi = 135^\circ$, all variable volumes were completely closed. Valve port 2 always remained

connected to the test section pipe while valve port 3 was always closed off with no attached variable volume.

Once the various frequency data were collected at the four compressor phase angles of 0°, 45°, 90°, and 135°, the collection of baseline data for the apparatus was complete. The next step was to smooth all data and to determine the Fourier series coefficients. The "Smoothy" program found in Appendix C, paragraph C.1, performed the following functions:

- Smoothed all data over one cycle by averaging all data points for a particular instrument within forty-eight windows, each 7.5° wide.
- Conducted a discrete Fourier transformation of all data to determine the Fourier series coefficients out to five harmonics.
- Combined the smoothed data from the two data files taken at a particular frequency and compressor phase angle into one smoothed .DAT file having all data for one cycle.
- Combined the smoothed data coefficients from the two data files taken at a particular frequency and compressor phase angle into one smoothed .COF file having all Fourier series coefficients for one cycle.
- Moves all raw data ASCII text files from the \DSA subdirectory into the \RAW subdirectory so that the much larger non-ASCII test files within the \DSA directory could be deleted to free storage space within the computer's hard drive.

With the .DAT files assembled, graphs of the smoothed data, as shown in section 5.3, were made. Additionally, the coefficients within the .COF files were analyzed by the "Nuc1" program in Appendix B to determine for each harmonic the complex Nusselt

numbers and the phase shift between ΔT and heat flux.

5.3 Discussion of Baseline Heat Transfer Data.

5.3.1 General Description of Results.

Baseline experimental data were collected at frequencies ranging from .35 Hz to 8.25 Hz and at compressor phase angle settings of $\Psi=0^\circ$, $\Psi=45^\circ$, $\Psi=90^\circ$, and $\Psi=135^\circ$. Figure 5.4 is a graph of raw heat flux data taken over one cycle, its smoothed curve, and the fitted Fourier series curves for one and five harmonics. The raw heat flux data shows that the sensor is picking up 60 Hz noise from equipment within the laboratory. The smoothed data, however, demonstrates that this noise has been minimized prior to conducting the Fourier transformation. In order to determine the magnitude of the complex Nusselt number and its corresponding phase angle for this data as well as all other data, the discrete Fourier transform was applied to smooth the data to five harmonics. The objective in using five harmonics was to smooth the data accurately without introducing noise; five harmonics proved satisfactory for this purpose. It should be noted that except for Figure 5.4, all graphs in this section show smoothed data and not raw data.

The data taken at $\Psi=0^\circ$ generally agree with Pfriem and Lee's analytic findings that at low frequencies ΔT and heat flux are in phase with each other (Figure 5.5), and that at high frequencies ΔT lags heat flux (Figure 5.6). At this compressor phase angle the maximum cyclic heat flux increases gradually as a function of Pe_ω as can be seen in Figure 5.7, while the maximum ΔT remains almost the same at all values of Pe_ω (Fig. 5.8). The phase shift difference generally increases with Pe_ω as will be discussed in section 5.3.2.

When data were collected at $\Psi=45^\circ$ a new phase phenomena emerged. At low

frequencies ΔT leads heat flux (Figure 5.9) whereas at higher frequencies heat flux leads ΔT (Figure 5.10). At this compressor phase angle, considerably more heat flux is generated than is the case at $\Psi=0^\circ$. More heat is transferred when $\Psi=45^\circ$ due to the suspected influence of the turbulent gas stream mixing the flow and equalizing the temperature across the core, giving a greater temperature gradient near the wall. We can refer again to Figure 5.7 to see this comparison graphically. Once again the maximum cyclic ΔT at $\Psi=45^\circ$ remains generally constant across the experimental range of Pe_∞ (Fig. 5.8) and almost equal to that experienced at all compressor phase angles.

Advancing the compressor phase angle to $\Psi=90^\circ$ and then to $\Psi=135^\circ$ reveals a trend in the relationship between heat flux and ΔT for all of the compressor phase angles tested. Simply stated, at $\Psi=0^\circ$ heat flux leads ΔT with large phase shifts between the two; as Ψ is increased to 45° we see a tendency for ΔT to lead heat flux at low frequencies but not at high frequencies with the phase shifts remaining close to half the values of those found at $\Psi=0^\circ$; when Ψ is further increased to 90° and 135° , we see that ΔT always leads heat flux yet the phase shifts between ΔT and heat flux approach zero degrees (heat flux and ΔT are almost in phase). We can see in Figures 5.11 and 5.12 the relationship between heat flux and ΔT at $\Psi=90^\circ$ and again in Figures 5.13 and 5.14 for $\Psi=135^\circ$. When we increase the compressor phase angle, we can see in Figure 5.7 that maximum cyclic heat flux correspondingly rises. This rise in cyclic heat flux does not continue with all higher compressor phase angles because at $\Psi=180^\circ$ the compressors merely shuttle the gas from one compressor to the other with no gas pressure rise, thus no temperature rise, and consequently no heat transfer. At some compressor phase angle between 135° and 180° the rise in cyclic heat transfer peaks and then begins to fall sharply to nothing at 180° .

5.3.2 Phase Angle Relationships.

As mentioned in Chapter 1, Pfriem had predicted that heat transfer would lead the core temperature by 45° at high frequencies when $\Psi=0^\circ$ (Pfriem,1943). The present experiments show, however, that the phase shift varies with frequency and the phase angle between pistons. Figures 5.15 and 5.16 demonstrate the change in the phase shift between heat flux and ΔT for the first and second harmonics respectively as Pe_ω increases. It can easily be seen that when $\Psi=0^\circ$, both the first and second harmonic phase shifts clearly surpass 45° for most values of Pe_ω . When the compressor phase angle is increased to $\Psi=45^\circ$, the phase shift never attains 45° for the first harmonic and only passes 45° with the second harmonic. As Ψ is further increased to 90° and 135° , both first and second harmonic phase shifts tend to remain close to 0° . Clearly these results do not agree with Pfriem's earlier work nor the recent work with gas springs reported by Kornhauser (1989) which was described briefly in Chapter 1. The reasons for these trends are at present illusive yet the trends are certainly affected by the role of the turbulent stream as well as the phase angle relationship of heat flux and ΔT with the pressure wave. As the compressor phase angle is increased from $\Psi=0^\circ$ to $\Psi=180^\circ$, an increase in mass transport within the test section results. Most mass flow occurs at $\Psi=180^\circ$ where the pistons shuttle a constant volume of air. At $\Psi=0^\circ$ the velocity at the test section, located midway between the two compressors, is negligible and the apparatus models a gas spring with this center point of the test section representing the closed end of the cylinder. We can therefore see that as Ψ increases so does the mass flow and not only is this suspected in aiding the increase in maximum cyclic heat transfer by increasing the temporal dT/dt term in Equation 8 (pg. 15), but is also suspected in varying the phase angle relationships between heat flux and ΔT .

5.3.3 Complex Nusselt Number Relationships.

Figures 5.17 and 5.18 demonstrate the change in the magnitude of the complex Nusselt numbers, Nu_c , as Pe_ω is increased for the first and second harmonics respectively. These graphs point out two trends. The data points indicate a general linear increase in Nu_c with Pe_ω for each compressor phase angle. Least square linear fits were made of these data points and the resulting lines are provided below.

$\Psi=0^\circ$:

1st Harmonic Fit: $Nu_c = (0.1896)Pe_\omega - 1.7844$

2nd Harmonic Fit: $Nu_c = (0.2333)Pe_\omega - 20.4801$

$\Psi=45^\circ$:

1st Harmonic Fit: $Nu_c = (0.2337)Pe_\omega + 22.7823$

2nd Harmonic Fit: $Nu_c = (0.2423)Pe_\omega + 27.9304$

$\Psi=90^\circ$:

1st Harmonic Fit: $Nu_c = (0.2337)Pe_\omega + 2.0971$

2nd Harmonic Fit: $Nu_c = (0.3868)Pe_\omega - 41.5308$

$\Psi=135^\circ$:

1st Harmonic Fit: $Nu_c = (0.2066)Pe_\omega + 22.4789$

2nd Harmonic Fit: $Nu_c = (0.2065)Pe_\omega + 1.8129$

These fitted lines are very parallel to one another for the first harmonic and almost as parallel for the second harmonic. The data for the second harmonic Nusselt numbers are slightly more scattered than for the first harmonic.

The second trend seen in Figures 5.17 and 5.18 is that for small values of Pe_ω (< 200), values for Nu_c generally remain between 0 and 75 for both harmonics. As Pe_ω is increased above 200, however, Nu_c increases linearly as mentioned previously, but attains its highest values with the second harmonic.

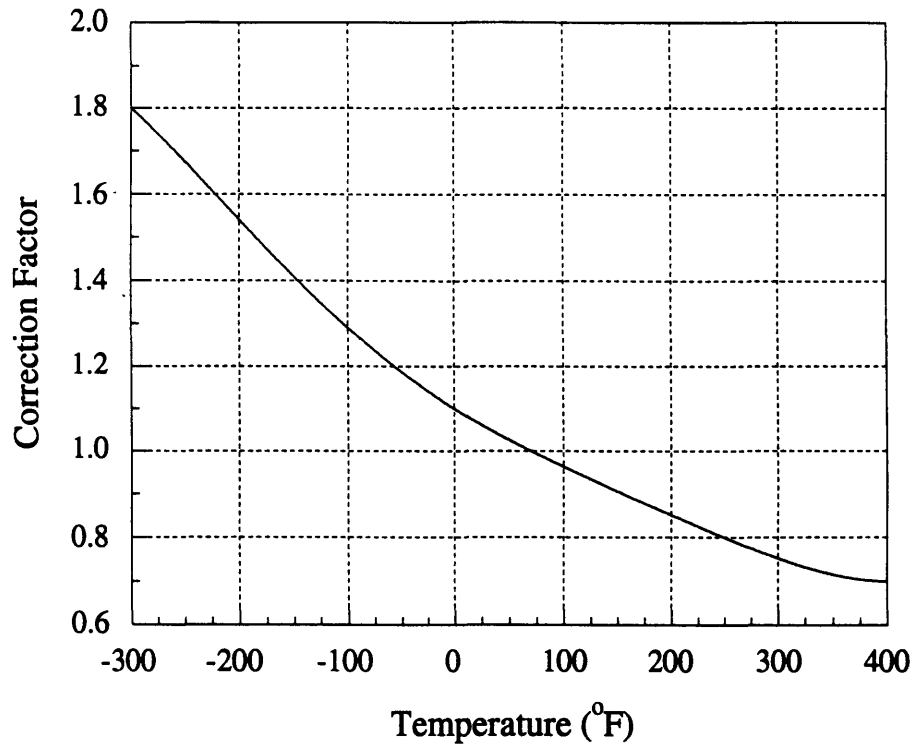


Figure 5.1 RdF Heat Flux Sensor Calibration Curve

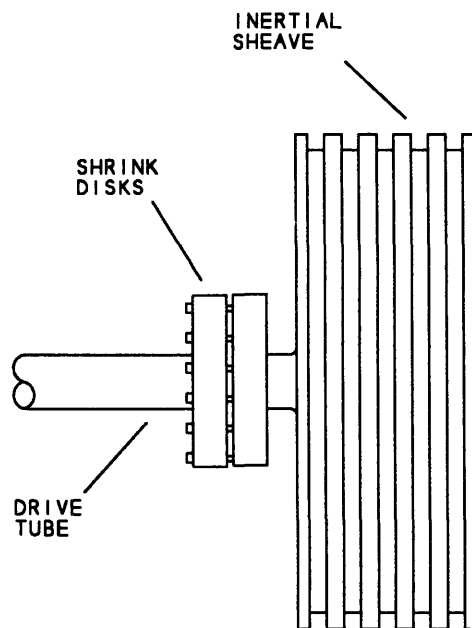


Figure 5.2 Diagram of Drive Tube Connection to Inertial Sheaves

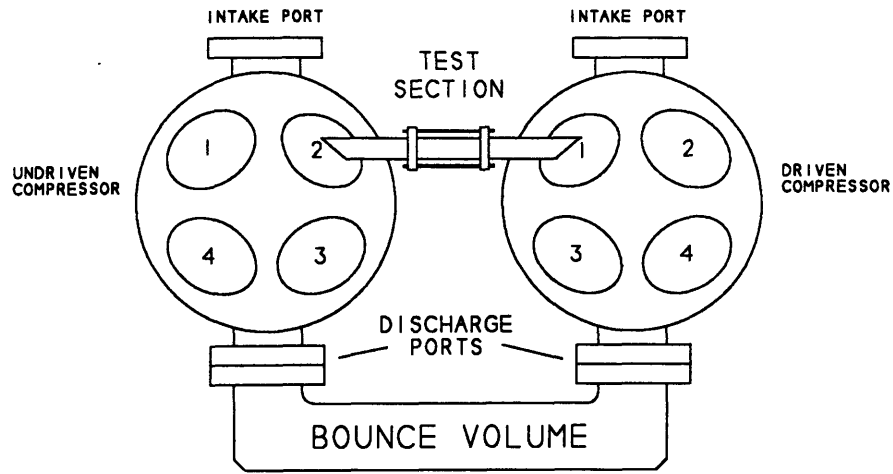


Figure 5.3 Diagram of Compressor Variable Volumes

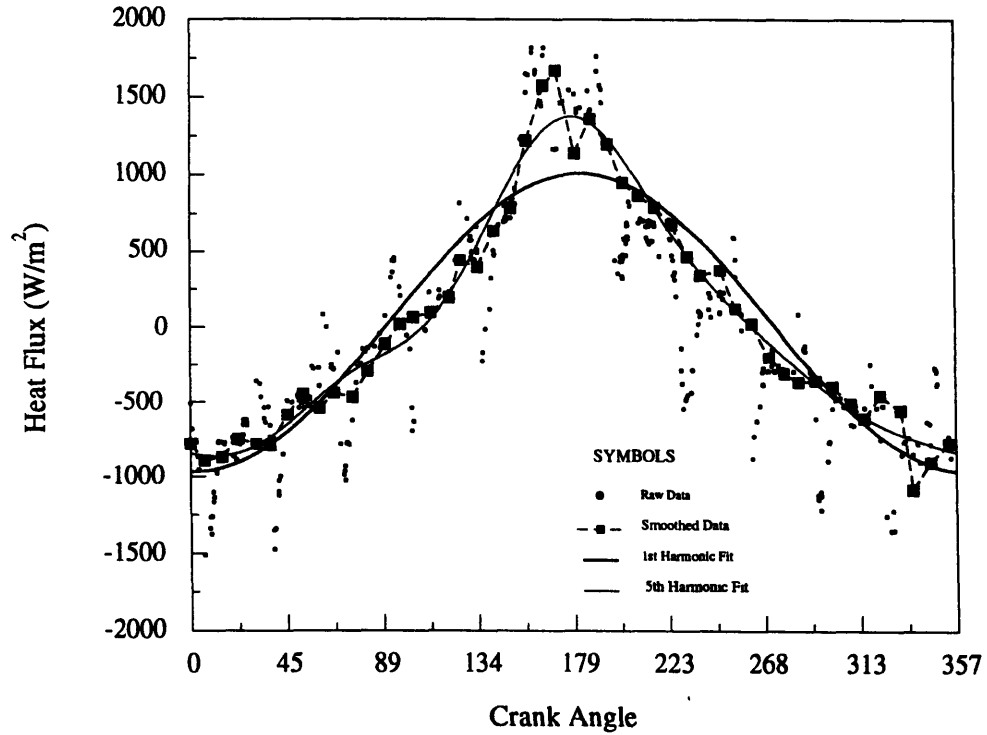


Figure 5.4 Raw and Smoothed Heat Flux Data, $f=5.07$ Hz, $Re_{\omega}=1044.8$, $\Psi=0^{\circ}$

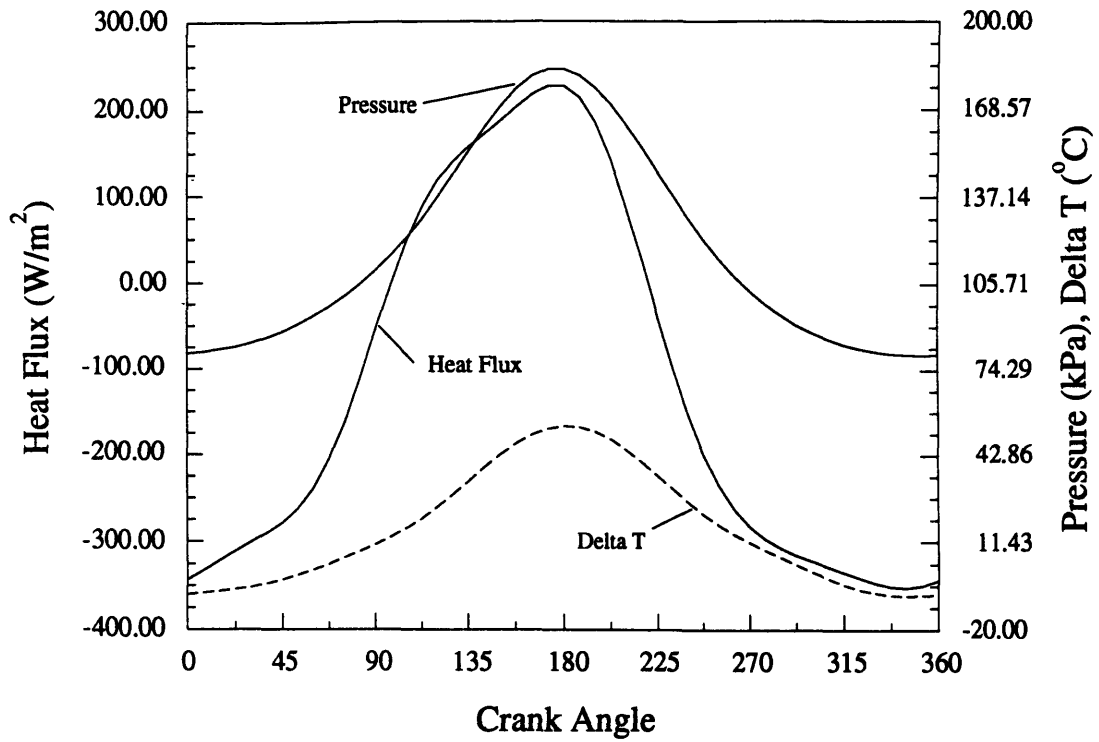


Figure 5.5 Low Frequency Oscillations, $f=0.33$ Hz, $Re_{\omega}=65.4$, $\Psi=0^{\circ}$

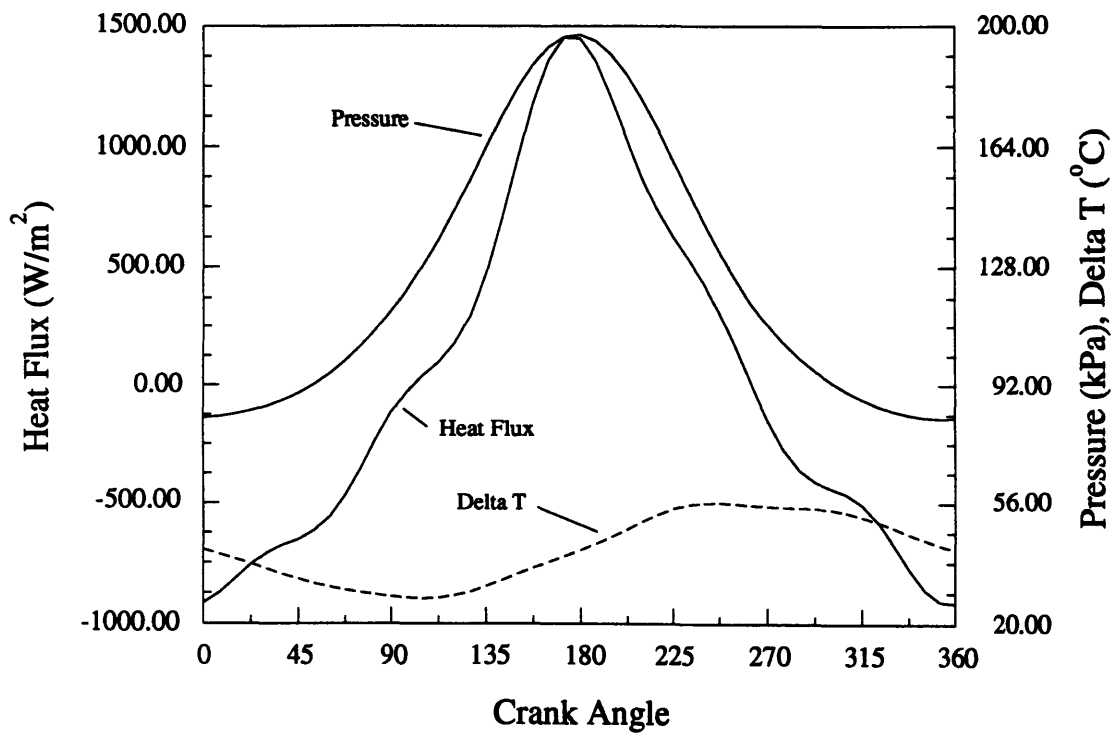


Figure 5.6 Higher Frequency Oscillations $f=5.07$ Hz, $Re_{\omega}=1004.8$, $\Psi=0^{\circ}$

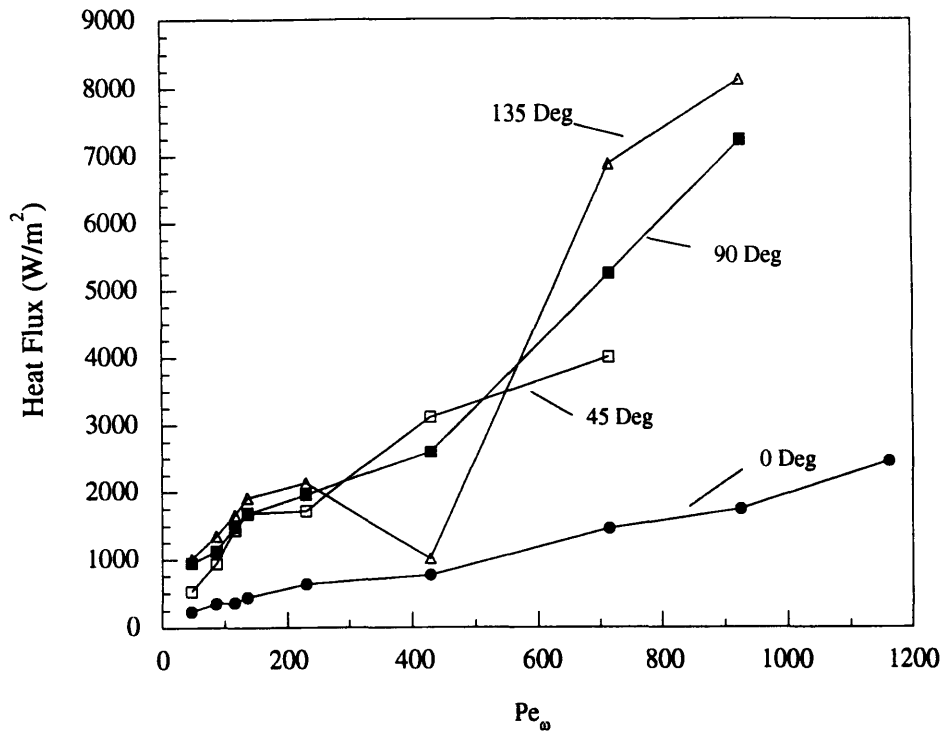


Figure 5.7 Maximum Cyclic Heat Flux as a Function of Ψ and Pe_{∞}

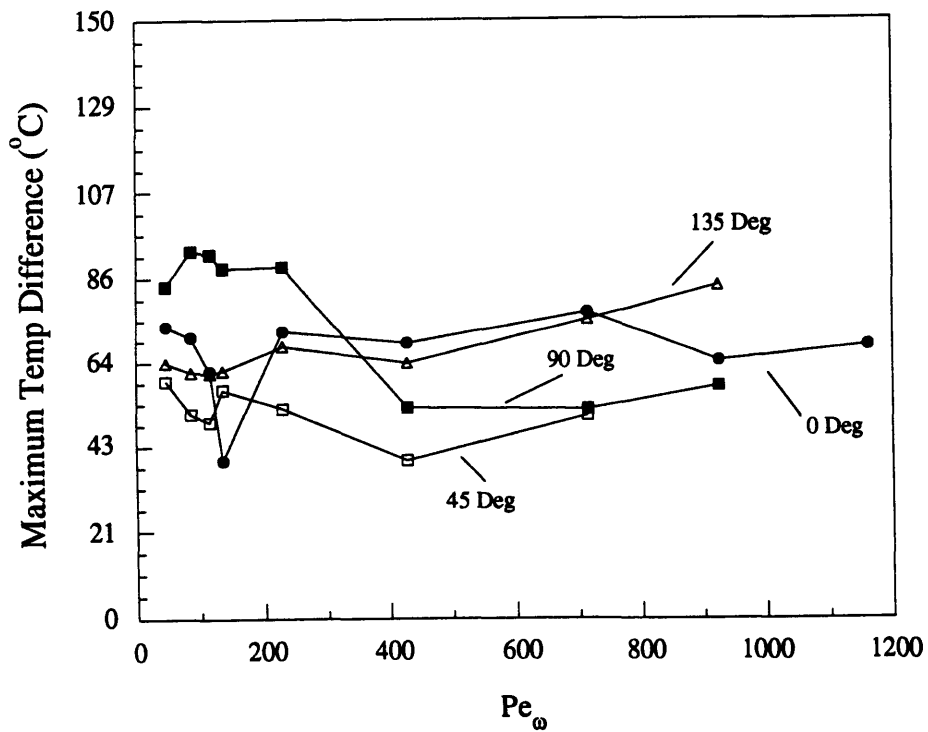


Figure 5.8 Maximum Cyclic ΔT as a Function of Ψ and Pe_{∞}

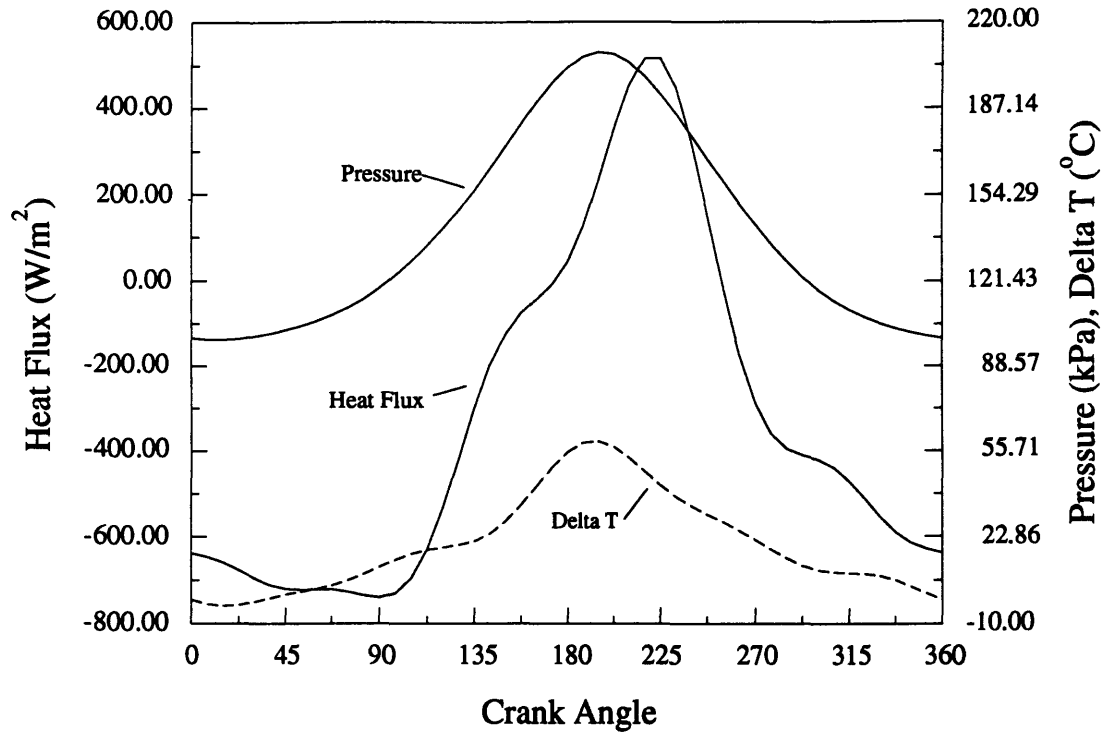


Figure 5.9 Low Frequency Oscillations, $f=0.33$ Hz, $Re_{\omega}=65.4$, $\Psi=45^{\circ}$

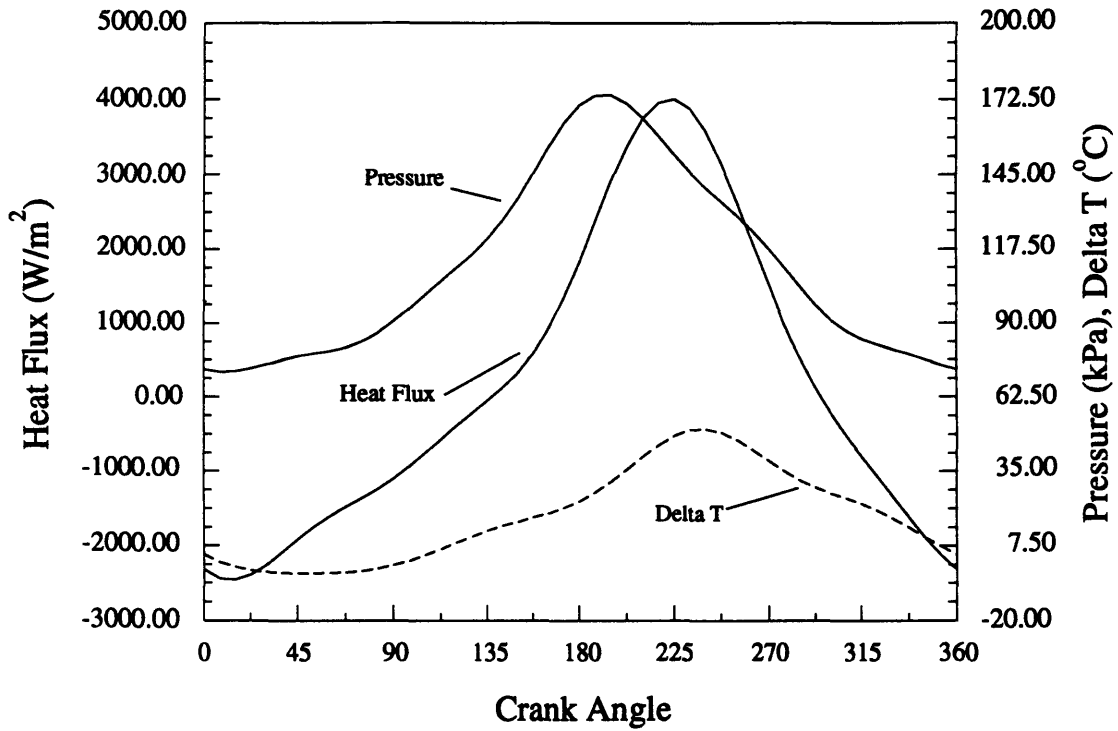


Figure 5.10 Higher Frequency Oscillations, $f=5.07$ Hz, $Re_{\omega}=1004.8$, $\Psi=45^{\circ}$

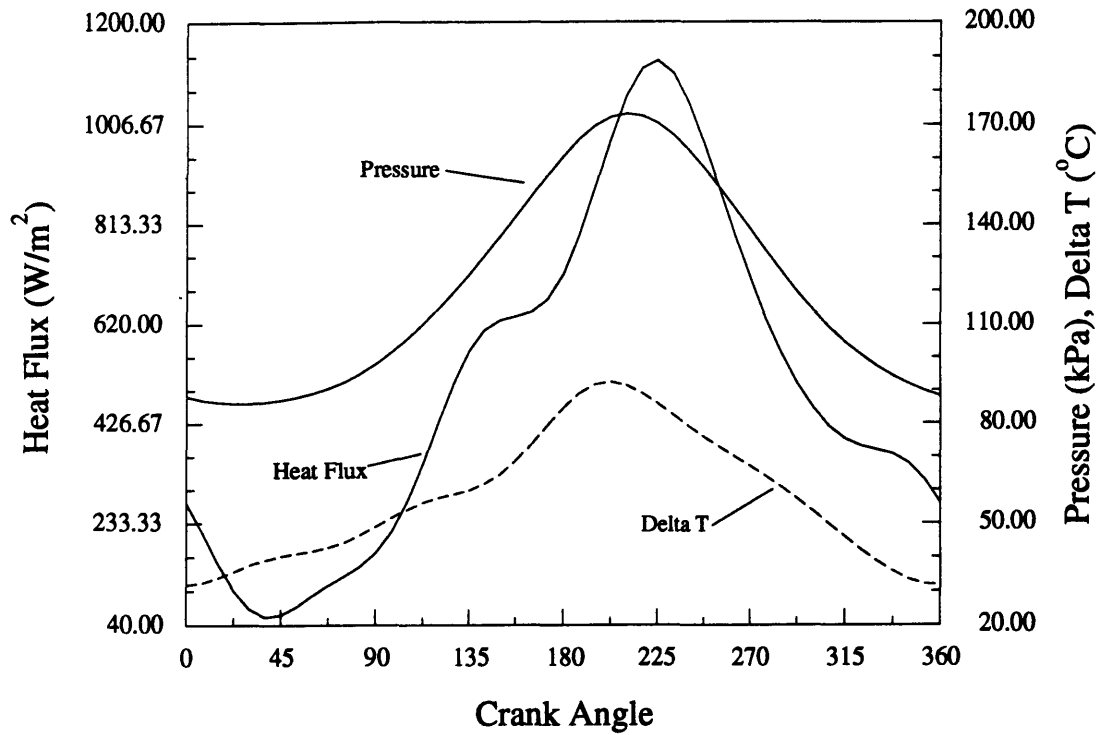


Figure 5.11 Low Frequency Oscillations, $f=0.32$ Hz, $Re_{\omega}=64.42$, $\Psi=90^{\circ}$

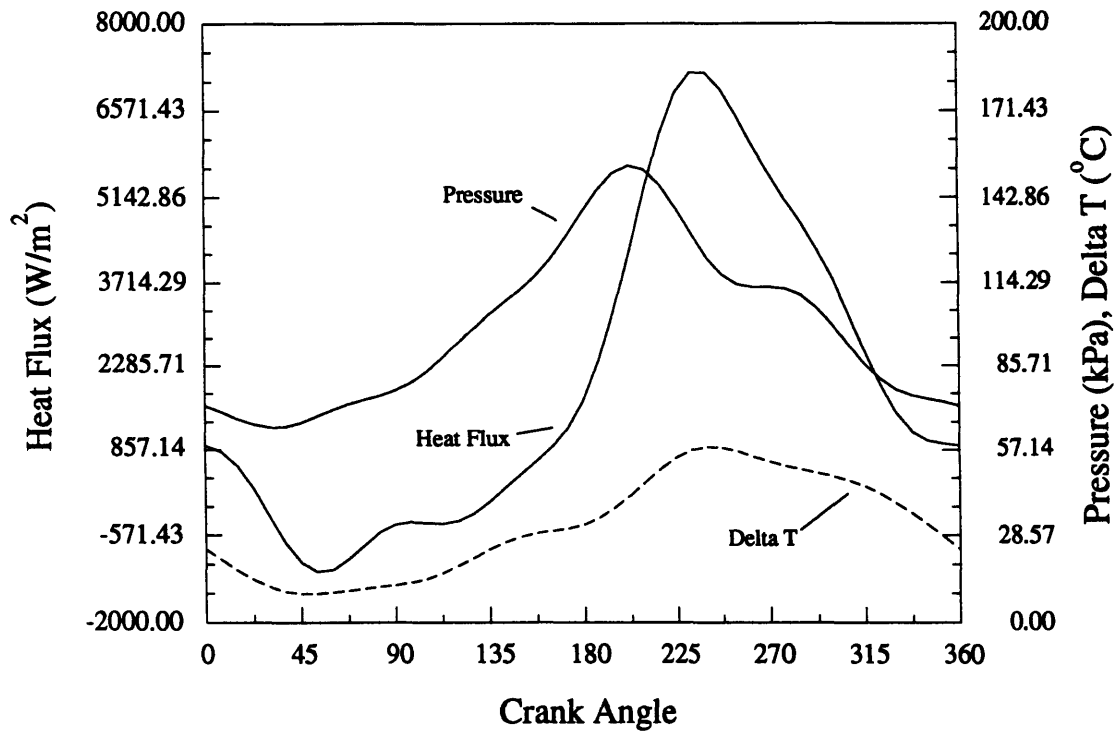


Figure 5.12 Higher Frequency Oscillations, $f=6.02$ Hz, $Re_{\omega}=1193.08$, $\Psi=90^{\circ}$

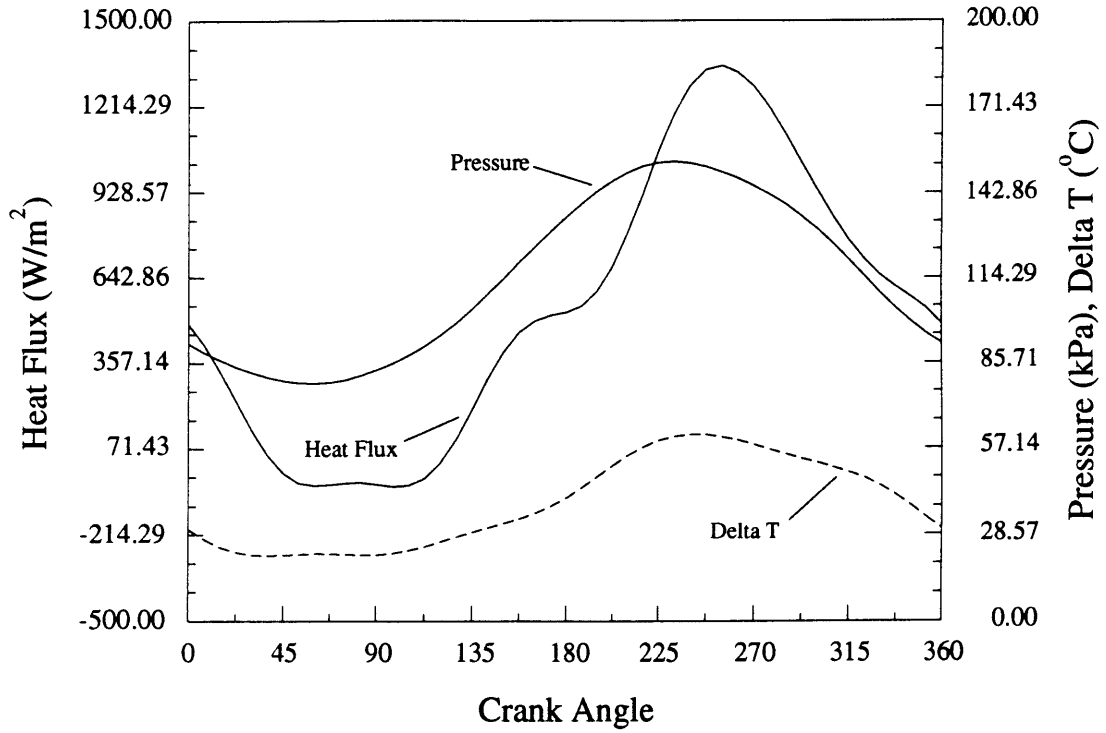


Figure 5.13 Low Frequency Oscillations, $f=0.23$ Hz, $Re_{\omega}=45.58$, $\Psi=135^{\circ}$

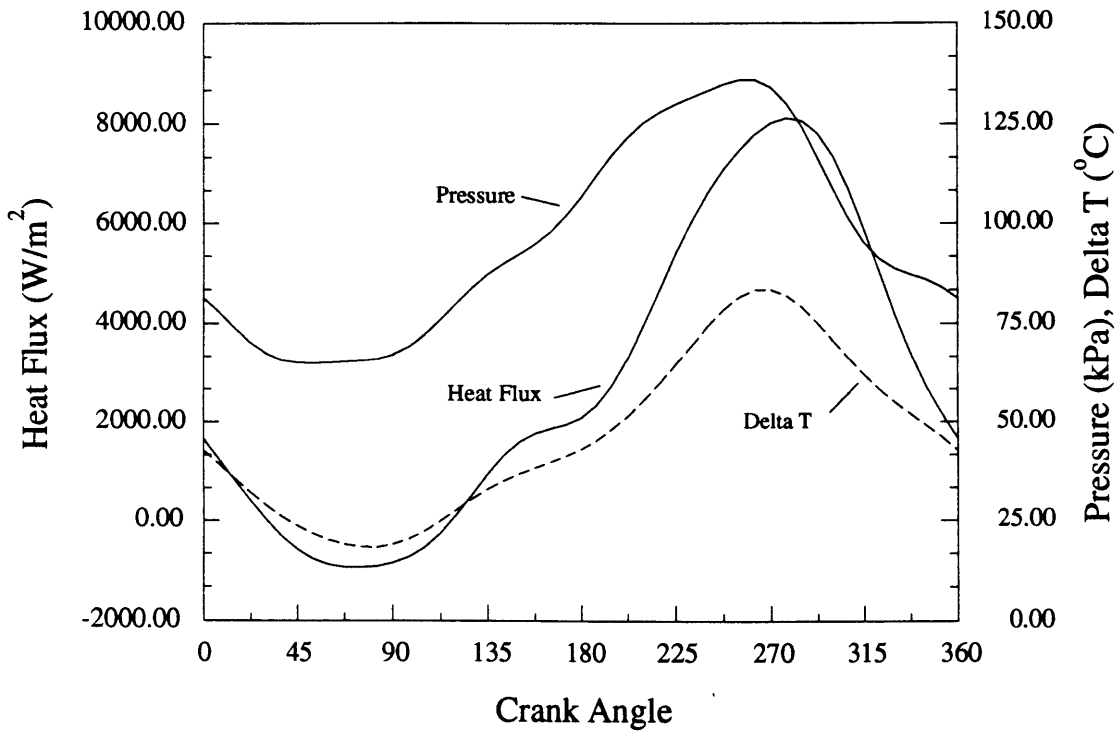


Figure 5.14 Higher Frequency Oscillations, $f=6.81$ Hz, $Re_{\omega}=1349.6$, $\Psi=135^{\circ}$

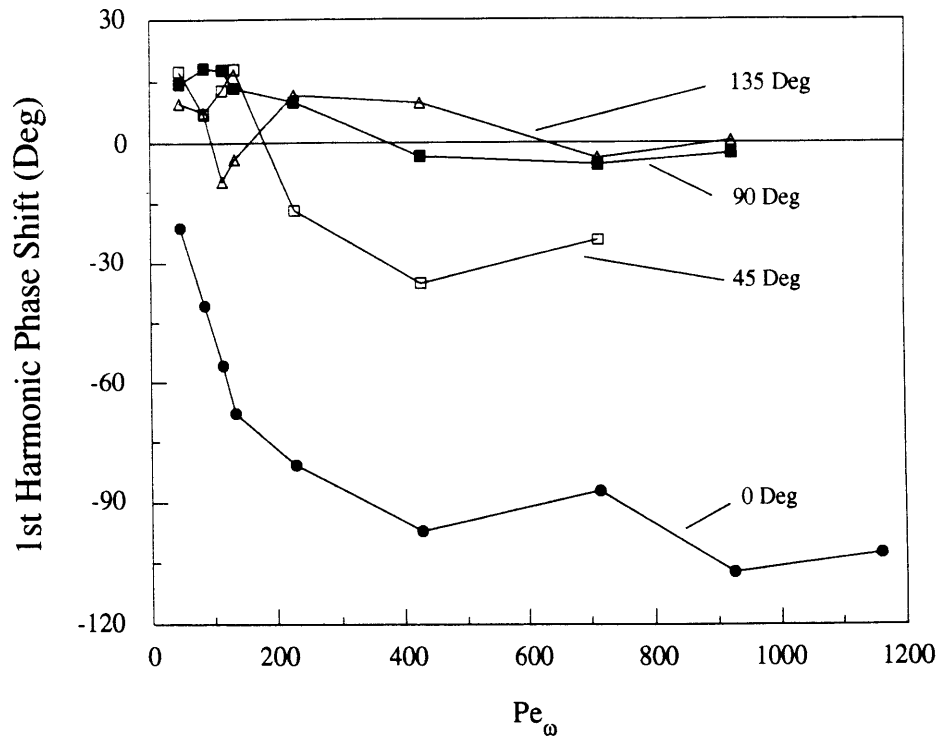


Figure 5.15 1st Harmonic Phase Shift as a Function of Pe_ω

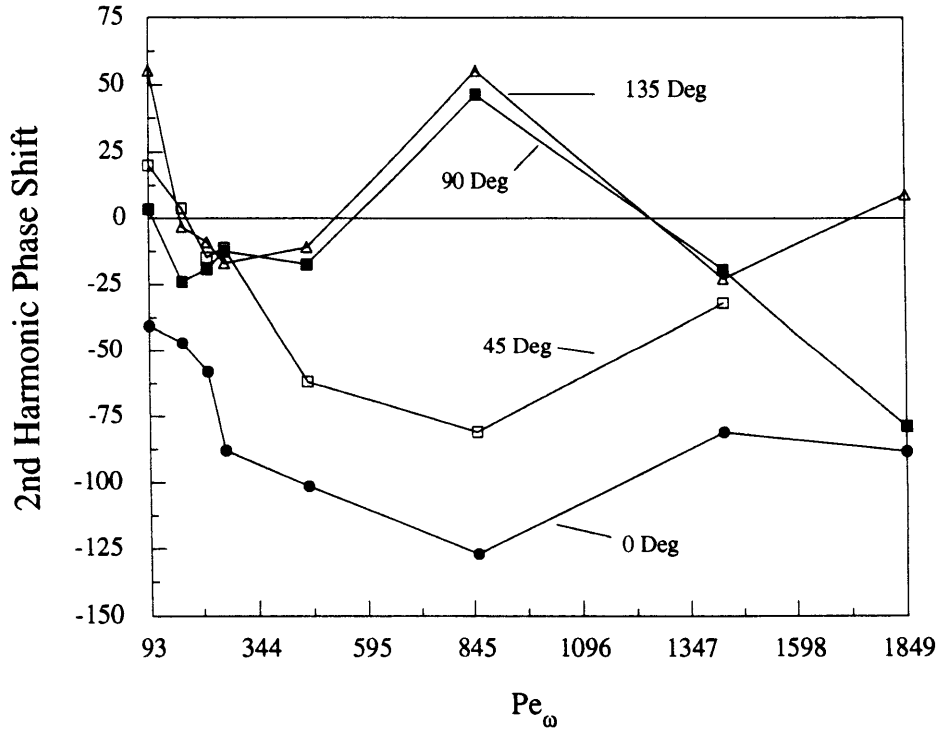


Figure 5.16 2nd Harmonic Phase Shift as a Function of Pe_ω

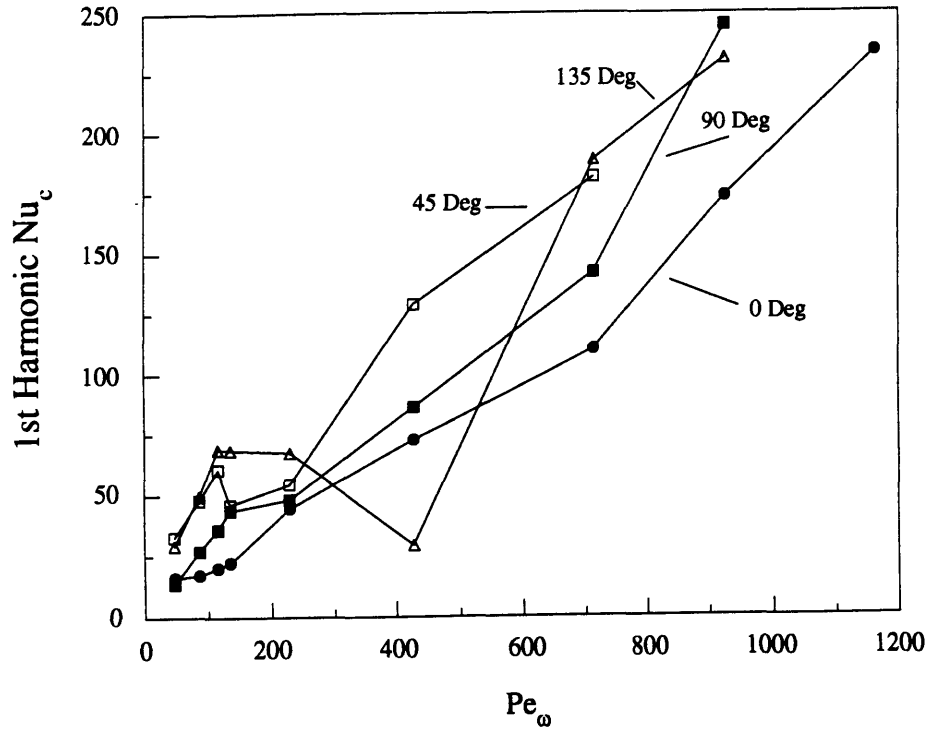


Figure 5.17 1st Harmonic Complex Nusselt Numbers as a Function of Pe_ω

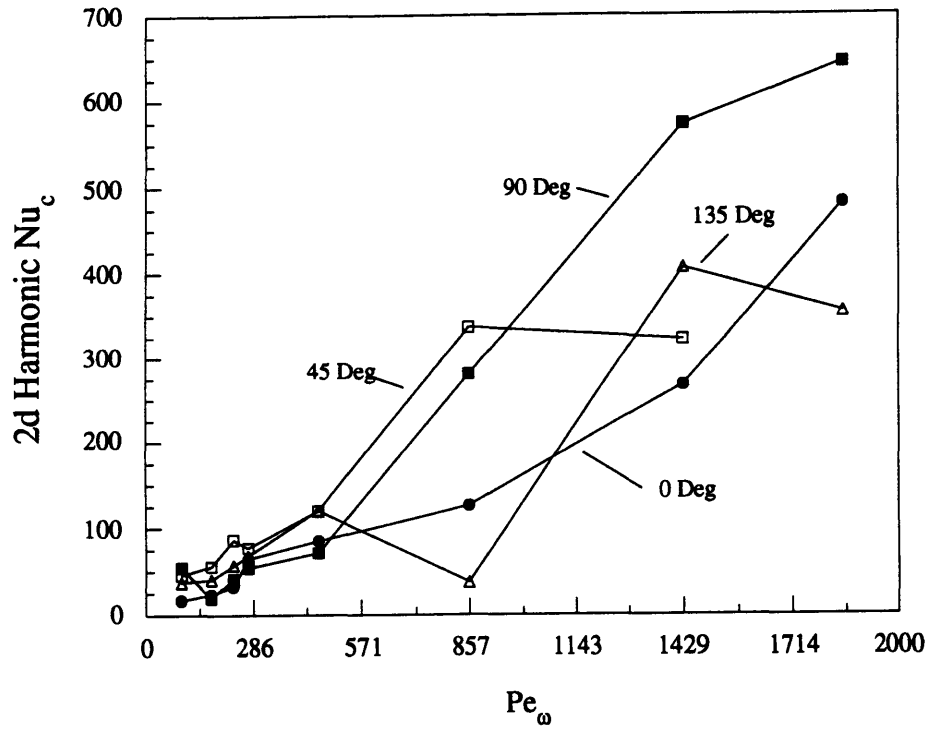


Figure 5.18 2nd Harmonic Complex Nusselt Numbers as a Function of Pe_ω

Chapter 6

Conclusion

6.1 Summary of the Study.

These experiments have confirmed the occurrence of a phase shift between heat transfer and temperature differences in a gas under conditions of oscillating flow and pressure. The complex Nusselt number serves as a means of modelling this type of heat transfer. The most significant findings from this experiment are:

1. The experimental results demonstrate the relationship between pressure, heat flux, and ΔT in a gas subjected to both oscillating pressure and flow. The phase shift between heat flux and ΔT is a function of Pe_{ω} and compressor phase angle Ψ . The phase shift increases to 102° at $Pe_{\omega}=1161$ when the compressor phase angle is $\Psi=0^{\circ}$, only attains 35° at $Pe_{\omega}=427.8$ when the compressor phase angle is set to $\Psi=45^{\circ}$, and remains close to 0° for compressor phase angles of $\Psi=90^{\circ}$ and $\Psi=135^{\circ}$.

2. First and second harmonic Nusselt numbers indicate distinctive linear trends as a function of Pe_{ω} and Ψ . Third and higher harmonic Nusselt numbers, however, become too noisy to demonstrate any significant patterns.

3. When the compressor phase angle is set to $\Psi=45^{\circ}$ or higher, ΔT leads heat flux when the frequency of oscillation is kept below 1 Hz. This contradicts existing theory and data from other types of experiments that show ΔT and heat flux to be in phase at low frequencies.

The findings discussed in this thesis are only the initial results obtained from the new experimental apparatus described. More detailed measurements are in progress. This study should significantly advance the engineering community's understanding of this

complicated heat transfer process and assist in producing program codes that can predict the effects of this type of flow on heat transfer in Stirling engine regenerators.

6.2 Recommendations for Future Work.

6.2.1 Equipment Recommendations.

In order to record accurate heat flux measurements, the sensor must be better insulated against background noise. The 60 Hz noise within the laboratory was found to easily disturb the sensor's output and it is this noise that must be directly targeted to improve the overall performance of the instrument.

The two areas that delayed the progress of this research and will hinder future work with the same experimental apparatus were the difficulty in maintaining proper laser beam to fiber optic coupler alignment and the difficulty in accessing the inside of the test section to clean the optical window and to replace the heat flux sensor when it became damaged.

(a) Laser Beam Optical Alignment.

After the two laser beams within the fiber drive are properly aligned with their respective fiber optic coupler, they remain aligned for only a short period of time. The vibrations from the two compressors probably cause these beams to move out of alignment. The only way to stabilize the optics is to mount the optical breadboard on vibration absorbers. This correction should be made as soon as possible to eliminate future delays caused by poor beam alignment within the fiber drive.

(b) Access to Inside of Test Section.

It is essential that the center piece of the three piece test section be redesigned so that the researcher has quick access to the inside of this piece of the system. We found that the smoke from the mineral oil smoke generator rendered the optical window dirty over a period of a week or so of moderate operation. An additional reason to have quick access to the inside of the test section is to replace heat flux sensors when they fail. With the test section in its current configuration, it took upwards of 1.5 hours for two people to remove the center piece, clean it of oil, and reassemble the apparatus.

A new design for the center section of the three piece test section is depicted in Figure 6.1. This design allows for a flat window lens to be dropped down into a recessed port in the test section from the outside. This flat window can then be removed for cleaning from the outside without disassembling the apparatus. The window would be held in position with a window bracket as pictured in Figure 6.2. This bracket bolts onto the outside of the test section and uses an O-ring to seal the area of the window against gas leakage.

The design also provides a heat flux sensor port that bolts onto the outside of the test section and uses glue to secure the heat flux sensor to its underside. The heat flux sensor port is shown in Figure 6.3. With this port, the sensor can be removed as was done with the optical window to service the gage. The remanufacture of the center section of the three piece test section will save countless hours in the future spent servicing this piece of equipment. This design may, however, produce undesirable experimental results that are determined by the flow disturbance caused by the change in wall contour near the heat flux sensor and the laser's probe volume.

6.2.2 Experimental Recommendations.

A great deal of work still needs to be completed before this study of periodic heat transfer under conditions of oscillating pressure and flow is complete. The overall goal of the project remains to determine numerical correlations for this type of heat transfer based upon frequency, pressure ratio, geometric parameters, and phase angle between the pressure wave and velocity wave. In order take the study from its present position to the final determination of these equations, the following work is recommended:

- Expand the baseline data collection by examining other compressor phase angles between those already studied and as an extension to this study, vary the pressure ratios for all compressor phase angles to see how heat transfer varies numerically with pressure ratio.
- Examine the phase angle relationship between pressure and velocity and observe how it relates to the phase angle ϕ between ΔT and heat flux.
- Complete a detailed study of the flow's transition to turbulence and determine what happens to the heat transfer as this transition occurs at varying compressor phase angles and pressure ratios.
- Take all data from the above steps and analyze it with a computer code that will arrive at the final equations for modelling heat transfer under conditions of oscillating pressure and flow.

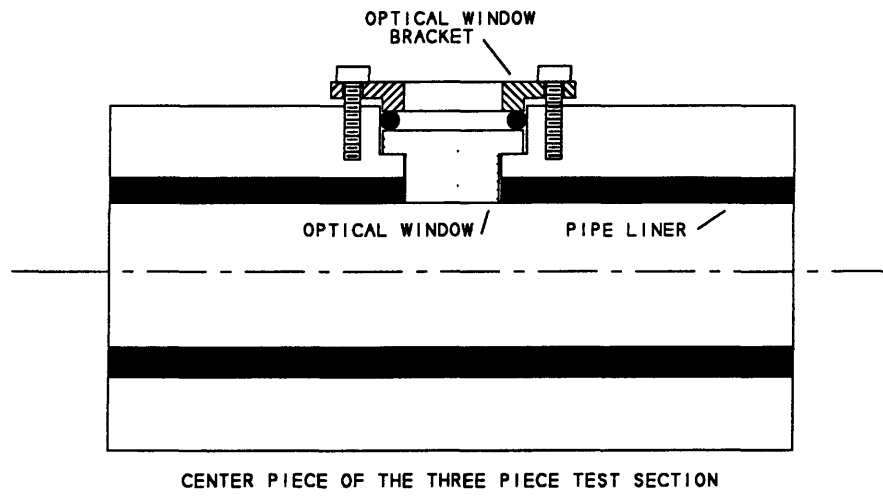


Figure 6.1 Improved Test Section Design

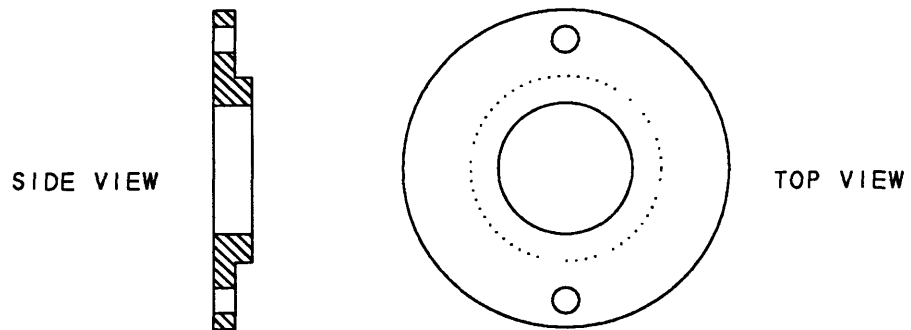


Figure 6.2 Optical Window Bracket

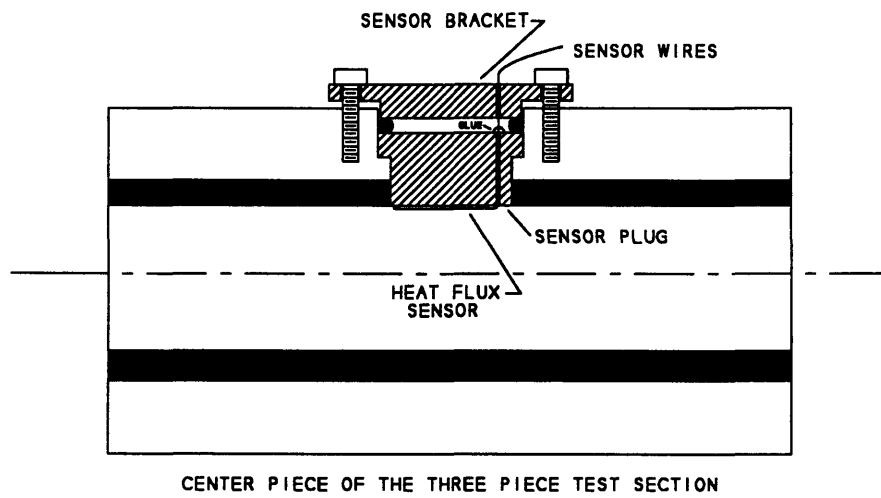


Figure 6.3 Heat Flux Sensor Port

Appendix A

Aligning the Laser Doppler Velocimeter

This appendix outlines the necessary steps for aligning the LDV optics for data acquisition. The topics and the hardware covered are described in geographic order as one follows the path of the laser beam from the Omnichrome laser to the test section. Laser protective goggles must be worn during all optical adjustments.

A.1 External and Internal Mirror Adjustment.

Two external mirrors are used to guide the reference laser beam from the Omnichrome laser to the Aerometrics fiber drive. Each external mirror has two knurled brass adjustment knobs on its corner surface. The top knob adjusts the reflected laser beam up and down, while the bottom knob adjusts the reflected laser beam left and right. Before the knobs on either external mirror are adjusted, however, the two alignment ports inside the fiber drive's right most chamber (as depicted in Fig. A.1) must be closed so that their alignment pinholes are exposed to the laser beam. The objective in aligning the external mirrors is to adjust the first external mirror so that the laser beam reflects off the second mirror and through the pinhole in the first port in the fiber drive. The second internal mirror is then adjusted so that the beam passes through the second port's pinhole and directly into the center of the hole on the end of the Bragg cell. Patience is a necessity as one adjusts these knurled knobs, but once the task has been completed, the two ports should be fully opened to enable the full width of the laser beam to pass from the laser to the Bragg cell.

As the reference beam departs the laser, its power is at a maximum of 300 mW. Caution should be taken with this beam because it can easily burn skin, paper, plastic, and wood. After the pinholes are slid away from the laser, the second port will have a light

filter exposed to the beam. This filter separates all wavelengths of light except the green 514 nm light that passes through the filter and into the Bragg cell. The laser beam should have close to 100 mW of power as it enters the Bragg cell.

The Bragg cell should never need positional adjustment within the fiber drive. Its position was set in the factory and should remain aligned. If adjustments are required to the Bragg cell's position, Aerometrics should be called first.

Chapter 3 describes how the Bragg cell produces two laser beams from the one reference beam that entered it. As these two laser beams depart the Bragg cell, they strike two internal mirrors that reflect these two beams back to the prismatic rhomboid. The internal mirrors should not need adjusting, as mentioned for the Bragg cell, but if need be, they can be realigned with a 0.050-inch hexagonal wrench. The researcher should look at the upstream face of the rhomboid to see if the two beams are striking it equidistantly on either side of the center line that separates its two facets. If the beams are not evenly spaced left and right of this line, then the bottom adjustment knob on the second external mirror should be turned slightly to space these beams evenly. Once the two beams are properly aligned on the rhomboid's face, the adjustment of all mirrors is complete. After the two laser beams pass through the rhomboid, they should each possess close to 28 mW of power before they strike the fiber optic cables.

A.2 Fiber Optic Coupler Alignment.

Perhaps the most difficult adjustment of the optics associated with the LDV is adjusting the fiber optic couplers. These couplers enable the two beams passing through air to properly enter the optical fibers that then transport these beams to the transceiver. As each beam passes through the rhomboid, it is focused and directed to its respective

coupler. Each coupler is used to position the end of its fiber optic cable so that the exposed end of the cable will intersect the associated laser beam at the beam's focal point.

Before any adjustments are made on the fiber optic couplers, however, the power level on the Bragg cell carrier control box should be set to 5.0, its mid-range.

The fiber optic coupler has two adjustment directions. The three X-Y adjustment screws are used to squeeze an O-ring, aligning the axis of the optical fiber within the coupler with the axis of the laser beam. The Z adjustment screw is used to move the end of the optical fiber either closer to or further away from the rhomboid to permit the focal point of the beam to strike directly upon the end of the fiber. How well the Z direction is adjusted is referred to as beam "efficiency." The first step in adjusting these screws is to very gently turn the X-Y adjustment screws until the power of each beam is maximized as it departs the transceiver at the other end of the fiber optic cable. In order to measure the power of a beam as one turns its adjustment screws, both the transceiver and the mount for the power meter's detector should be clamped to the lab bench so that the beam directly strikes the face of the detector. Once the X-Y adjustments have been made, then the Z adjust screws are loosened and the black drum containing the Z adjust set is gently turned in either direction to even further increase the power of the beam departing the transceiver. A good power meter reading of each beam as it exits the transceiver is 12 mW. After the first beam's power has been maximized, then the second beam is aligned identically.

A.3 Laser Beam Polarization Alignment.

In order for the laser beams to produce a proper fringe pattern within the probe volume, their respective polarization must be aligned in parallel with one another's. Aerometric's standard is that the beams cannot be more than 15° out of parallel for good

results. Place a target in front of the transceiver so that the beams can be seen striking its surface. Next hold a polarization filter between the transceiver and the target. As you slowly rotate the filter, the beams will get brighter and duller. When they almost disappear they are said to be "extinguished." The key then is to get these two beams to extinguish at the same time as the filter is turned. If they extinguish at different times, then they must be adjusted at the silver knurled nut that joins each yellow optical fiber to its fiber optic coupler. Adjust one cable at a time by slightly loosening the silver knurled nut on one fiber optic coupler, then gently turn the silver cylinder within the nut while you consecutively turn the polarization filter between the transceiver and the target. If turning one cable is enough to have the two beams extinguish together, then re-tighten the knurled nut. If the turning of one yellow cable is not enough, then get the first cable to its best position, tighten down its nut, then loosen the other cable's nut and repeat the procedure with the second cable until the two beams extinguish together. Once the polarization is set, recheck to ensure that each beam registers its maximum power as it departs the transceiver; the X-Y adjustment screws on the fiber optic coupler may need to be realigned.

A.4 Equalizing Dual Beam Power.

In order to record the most data with the least possible noise, the two beams emitting from the transceiver must have the same power level (close to 12 mW). This is verified with the power meter and should be checked at the beginning and at some point during a day's collection of data. Most likely these beams will have different power levels, but these settings can be adjusted by turning the black knob on the face of the Bragg cell carrier control box, which was previously set to 5.0. This knob shares the power between the two beams, resulting in any adjustment increasing the power in one beam while reducing the power in the other beam. By gently turning this knob in each direction, the powers of the two beams can be balanced on the power meter by reading one beam's power at a time.

A.5 Laser Beam Intersection and Transceiver Flexure Alignment.

From time to time the intersection point of the two laser beams should be checked to ensure that the beams are intersecting and to verify that they intersect at their focal points. The focusing lens within the transceiver has a 250 mm focal length which means that 250 mm in front of the transceiver these two beams should intersect. The same target that was used to adjust the polarization can be used again but this time place the small end of the microscope objective at the intersection point and view its image on the target. Gently move the microscope objective toward and away from the transceiver and watch the two beams pass through intersection. If at some point they do not intersect at a fine point, they must be adjusted.

To adjust the intersection of the two laser beams we must first determine where a point is that lies 250 mm directly in front of the center of the focusing lens. To do this, open the top cover of the blue photodetector and carefully remove the orange return optical fiber from the box. Within this box the ceramic end of the orange optical fiber is held by a set screw to the top of the photodetector. Once this set screw is loosened the end of the optic cable will easily pull out. With the end of the orange optical fiber removed from the photodetector, clamp it with a lab stand directly in the path of the laser beam as it departs the second external mirror and heads for the fiber drive. The laser beam will travel through the orange cable backwards and will emit through the center of the transceiver's focusing lens and strike the target. Tape a piece of paper onto the target. Move the target closer to and further away from the transceiver until the target is at the local point of the beam. At this location the beam will be most intense and yet the smallest in width as seen on the target. Carefully mark where this beam strikes the target with a pencil and even go so far as to tape the target to the table so that it cannot be easily bumped out of position. Now remove the orange fiber away from the reference beam and allow the two beams to once again depart the Bragg cell and emit from the

transceiver. Block one of these beams between the transceiver and the target so that you can align one beam at a time onto the pencil mark on the target. A single strip of transparent "Scotch" tape across the end of the transceiver will sufficiently block the beam.

Each fiber optic cable terminates inside the conical back of the transceiver at an optical flexure. These flexures are used to adjust where the beams intersect. Each flexure has four X-Y adjustment screws and one Z adjustment screw. The Z adjustment screw should not be touched. The X-Y adjustment screws work in opposite pairs. Place a 0.050" hexagonal wrench in each of two opposite screws. As you gently turn one clockwise, turn the other counterclockwise. Watch the movement of the beam on the target. Work both sets of opposite pairs of screws in this way until the beam is positioned directly on the pencil mark. Now block this beam and repeat the procedure for the other beam. Once completed, move the target further away from the transceiver and use the microscope objective to ensure that these beams properly intersect. Two or three iterations may be necessary as one learns this procedure.

A.6 Laser Beam to Test Window Alignment.

As mentioned in Chapter 3, the laser beams must be properly aligned with the long axis of the test window. The easiest way to do this is to mount the transceiver above the window and to then turn it by hand so that the two beams appear to be on line with the long axis of the window. Next try to collect data with the laser. As the data is collected, gently turn the transceiver to try to get the highest percent validation rate possible. This procedure usually takes two people and has generally proven that the initial visual alignment was about as good an alignment as one will get.

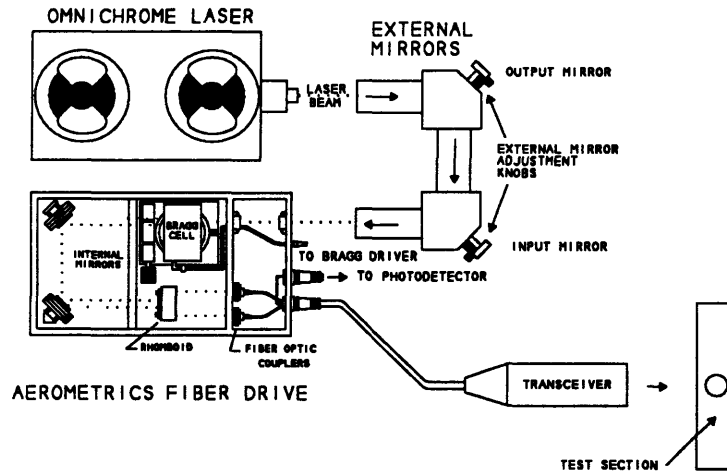


Figure A.1 Schematic Diagram of Laser Beam Path

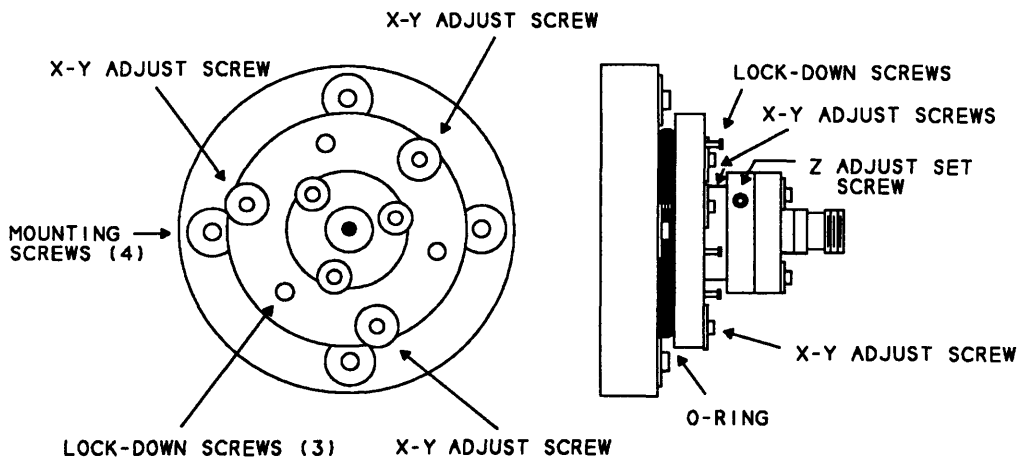


Figure A.2 Fiber Optic Coupler

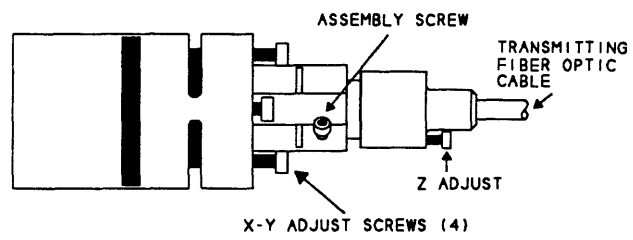


Figure A.3 Transceiver Flexure Coupling

Appendix B

Computer Programs

B.1 Data Smoothing and Fourier Decomposition Program, "Smoothy".

```
*****
*
* This program was written in FORTRAN by William A. Grassmyer. It smooths all *
* raw data collected by the instruments mounted in the test section and then *
* conducts a Fourier series decomposition of the smoothed data to determine *
* the Fourier series coefficients for five harmonics. *
*
*****
```

```
CHARACTER*32 INPUT,DI
CHARACTER*12 CH,DV,CR1,CR2
CHARACTER AUTO*1,RUN*2,OUT*7,VOLT*3,FL*4,PH*3
```

```
DIMENSION V(4000),T(4000),EX1(4000),EX2(4000),KEN(4000),CH(2),
*VN(4000),TN(4000),EX1N(4000),EX2N(4000),KENN(4000),EN(4000),
*XSIN(200),XCOS(200),A(20),B(20),A1(20),B1(20),A2(20),B2(20)
*IC(50),XX(20),V1(361),CX1(361),CX2(361),XV(361),XC1(361),
*XC2(361),VT(361)
```

```
WRITE(*,*)'INPUT BAROMETRIC PRESSURE(IN. HG):'
READ(*,*) BARO
WRITE(*,*)
```

```
83 WRITE(*,14)
14 FORMAT(/,5X,'COMBINE TWO FILES? ',/9X,'1) NO ',/9X,'2) YES' /)
READ(*,*) LF
IF(LF.NE.1.AND.LF.NE.2) GOTO 83
```

```
WRITE(*,*)
WRITE(*,*)'INPUT THE VOLTAGE OF RUN(EX 050):'
READ(*,*(A3)) VOLT
```

```
WRITE(*,*)
WRITE(*,*)'INPUT POSITION IN FLOW(EX 0200):'
READ(*,*(A4)) FL
WRITE(*,*)
```

```

OUT=VOLT//FL
WRITE(*,*) OUT
C   WRITE(*,*)'INPUT NAME OF OUTPUT FILE(EX 0500200):'
C   READ(*,517) OUT
517 FORMAT(A7)

WRITE(*,*)
WRITE(*,*) 'PHASE ANGLE (EX. 045):'

READ(*,'(A3)') PH
WRITE(*,*) 'PHASE ANGLE (EX 45.):'
READ(*,'(F6.2)') PHI

WRITE(*,*) 'HEAT FLUX AMPLIFICATION:'
READ(*,*) HFA

WRITE(*,*) 'OTHER INFO ON DATA (32 CHARACTER MAX):'
READ(*,511) DI
511 FORMAT(A32)

OPEN(UNIT=7,FILE='C:\COEF\PH\^\'//OUT//'.COF',
*STATUS='UNKNOWN')
OPEN(UNIT=9,FILE='C:\CYCLE\PH\^\'//OUT//'.DAT',
*STATUS='UNKNOWN')

DO 377 MF=1,LF
WRITE(*,*)'INPUT NUMBER OF AUTO DIRECTORY (EX 3)'
READ(*,'(A1)') AUTO
518 FORMAT(A11)
WRITE(*,*)

WRITE(*,*)'INPUT RUN NUMBER OF FILE (EX 07):'
READ(*,'(A2)') RUN
WRITE(*,*)

OPEN(UNIT=3,FILE='C:\DSA4\DSADATA\ASME\AUTO\^\'//AUTO\^\'
*//RUN\^\'//RUN\^\'//DSARAW.TXT',STATUS='OLD')
READ(3,*)

WRITE(*,*)'C:\RAW\A\^\'//AUTO\^\'//R\^\'//RUN\^\'//.RAW'

OPEN(UNIT=21,FILE='C:\RAW\A\^\'//AUTO\^\'//RUN\^\'//RUN\^\'//.RAW',
*STATUS='UNKNOWN')

2  FORMAT(/,5X,'ENTER THE CORRECT #:',/10X,'1) PRESSURE',
*/,10X,'2) HEAT FLUX',/10X,'3) TEMP THERMOCOUPLE',/10X
*,'4) TEMP RTD',/10X,'5) NO CALIBRATION')
WRITE(*,2)

```

```

WRITE(*,3)
3  FORMAT(/,5X,'FOR EXT INPUT #2:')
   READ(*,*) KX1
4  FORMAT(/,5X,'FOR EXT INPUT #3:')
   WRITE(*,4)
   READ(*,*) KX2
19  FORMAT(5F12.5)

NP=1

5  READ(3,*,END=8) V(NP),EN(NP),EX1(NP),EX2(NP),T(NP)
   WRITE(21,19) V(NP),EN(NP),EX1(NP),EX2(NP),T(NP)
   NP=NP+1
   GOTO 5

8  NP=NP-1

DO 88 I=1,NP
88  KEN(I)=EN(I)

NOP=NP

CALL SMOOTH(V,EX1,EX2,T,KEN,NP,VN,TN,EX1N,EX2N,KENN)

C  DO 27 I=1,NP
C 27 WRITE(*,*) KENN(I),VN(I)
C   PTO=NOP-NP
C   WRITE(*,*) PTO,NP
C   PAUSE

JT=0
DO 20 IT=2,NP
IF (KEN(IT)+10.LT.KEN(IT-1)) THEN
  JT=JT+1
  IC(JT)=IT
ENDIF
20  CONTINUE

IF(JT.GE.2) GOTO 474

IF(JT.EQ.1) THEN
  DO 59 I=IC(1),NP
  IF(KEN(2).LE.KEN(I)) THEN
    PERA=T(I)-T(2)
    GOTO 889
  ENDIF
59  CONTINUE
ENDIF
WRITE(*,*) 'ERROR: ONE FULL PERIOD OF DATA WAS NOT TAKEN'
GOTO 701

```

```

474 PS=0
    DO 63 I=2,JT
        I1=IC(JT-1)
        I2=IC(JT)
        PER=T(I2)-T(I1)
63   PS=PS+PER
        PERA=PS/REAL(JT-1)

889 CONTINUE

C   WRITE(*,*) JT

C   CALL TADJ(

WRITE(*,*) 'LEAVE ME ALONE DAMMIT! IM SORTING'
CALL SORT(V,EX1,EX2,NP,T,KEN)

CALL GROUP(NP,V,EX1,EX2,T,KEN,NW,VN,EX1N,EX2N,TN,KENN)

CALL CONVRT(KX1,KX2,NW,EX1N,EX2N,CH,BARO,HFA)

M=5
TIME=1200

CALL FORIER(NW,M,TIME,VN,KENN,A0,A,B,XSIN,XCOS)

CALL FORIER(NW,M,TIME,EX1N,KENN,A01,A1,B1,XSIN,XCOS)

CALL FORIER(NW,M,TIME,EX2N,KENN,A02,A2,B2,XSIN,XCOS)

```

c CALCULATE VOLUME

```

DO 118 I=1,NW
    POS=REAL(KENN(I))/1200.
    PI=3.1415927
    RAD=2.*PI*POS
    VL=PI*11.**2./8.*(30.+9.*(1.+COS(RAD))-SQRT(
* (9.*COS(RAD))**2+819.))
    VR=PI*11.**2./8.*(30.+9.*(1.+COS(RAD-PHI))-SQRT(
* (9.*COS(RAD-PHI))**2+819.))
    VTS=371.21+(2.00*16.84)
    VFDV=(2.*726.)*1.6387*10.**(-5)
    VADV=0.
    VTDV=VFDV+VADV
118  VT(I)=(VL+VR+VTS)*1.6387*10.**(-5)+VTDV

```

C*****OUTPUT*****


```

716 FORMAT(/,5X,'DIRECTORY = AUTO',A1,'^RUN',A2,/)
WRITE(7,716) AUTO,RUN
IF(MF.EQ.1) THEN
WRITE(7,717) VOLT,FL,PH,VTDV,BARO,DI
ENDIF

717 FORMAT(5X,'VOLTAGE = ',A6/,5X,'FLOW POSN = ',A6/,5X,
*'PHASE ANGLE= ',A6/,5X,'DEAD VOLUME= ',F7.5/,5X,
*'BARO PRESS = ',F7.3/,5X,'NOTE = ',A32)

WRITE(7,555) CH(1),CH(2)
555 FORMAT(/,25X,'FOURIER COEFFICIENTS',/,2X,'HARMONIC',8X,
*'VELOCITY',10X,A12,10X,A12,/,16X,'A',7X,'B',12X,'A',9X,'B',
*12X,'A',8X,'B')

I=0
WRITE(7,566) I,A0,A01,A02
566 FORMAT(4X,I2,6X,F7.3,13X,F9.3,12X,F10.3)

DO 700 I=1,M
700 WRITE(7,699) I,A(I),B(I),A1(I),B1(I),A2(I),B2(I)

699 FORMAT(4X,I2,6X,F7.3,2X,F7.3,4X,F9.3,1X,F9.3,2X,F10.3,2X,F10.3)

WRITE(7,577) PERA
577 FORMAT(/,5X,'PERIOD=',F7.4,' SEC')

C*****OUTPUT TO *.DAT FILE*****

DO 12 I=1,NW
POS=REAL(KENN(I))/1200.
TIM=POS*PERA
V1(I)= CURV(POS,A0,A,B,M,XX)
CX1(I)= CURV(POS,A01,A1,B1,M,XX)
12 CX2(I)= CURV(POS,A02,A2,B2,M,XX)

IF(LF.EQ.1) GOTO 323

C*****COMBINING TWO RUNS*****

IF(MF.EQ.1) THEN
CR1=CH(1)
CR2=CH(2)
XPER=PERA
DO 43 I=1,NW
XV(I)=V1(I)

```

```

XC1(I)=CX1(I)
43  XC2(I)=CX2(I)
    ELSE
      WRITE(9,61) CR1,CR2,CH(1),CH(2)
61  FORMAT(4X,'DEGS',1X,'TIME',5X,'VEL',2X,'VOL',4X,
*  A9,1X,A9,4X,A9,1X,A9,/)

    PERM=(XPER+PERA)/2.
    I=0
    DEG=0.
    TIM=0
    VA=(XV(NW)+V1(NW))/2.

    WRITE(9,89) DEG,TIM,VA,VT(NW),XC1(NW),XC2(NW),CX1(NW),CX2(NW)
    DO 47 I=1,NW
      POS=REAL(KENN(I))/1200.
      DEG=POS*360.
      TIM=POS*PERM
      VA=(XV(I)+V1(I))/2.
47  WRITE(9,89) DEG,TIM,VA,VT(I),XC1(I),XC2(I),CX1(I),CX2(I)
    ENDIF
89  FORMAT(2X,F5.1,F7.3,F8.3,F8.4,F10.4,F11.4,2F10.4)

    GOTO 377
C*****JUST ONE FILE*****

323 WRITE(9,921) CH(1),CH(2)
921 FORMAT(1X,'ENC POS',9X,'TIME',9X,'VELOCITY',7X,A12
* ,3X,A12,/)

    TIM=0
    I=0
    WRITE(9,422) I,TIM,V1(NW),CX1(NW),CX2(NW)
    DO 324 I=1,NW
      POS=REAL(KENN(I))/1200.
      TIM=POS*PERA
324 WRITE(9,422) KENN(I),TIM,V1(I),CX1(I),CX2(I)

422 FORMAT(2X,I5,4F15.4)

377 CONTINUE

701 WRITE(*,485)
485 FORMAT(/,5X,'WANT TO RUN AGAIN?',/9X,'1) YES',/9X,'2) NO',/)
    READ(*,*) NNN
    IF(NNN.EQ.1) GOTO 83

    END

```

C*****SUBROUTINES START HERE*****

```

SUBROUTINE SMOOTH(V,EX1,EX2,T,KEN,NP,VN,TN,EX1N,EX2N,KENN)

DIMENSION V(NP),T(NP),EX1(NP),EX2(NP),KEN(NP),VN(NP),TN(NP)
*,EX1N(NP),EX2N(NP),KENN(NP)

IN=NP/10.
NC=-9
KC=0

DO 25 K=1,IN-1
NC=NC+10
VS=0.
DV=0.

DO 35 L=NC,NC+9
35 VS= VS+V(L)
VA=VS/10.

DO 45 L=NC,NC+9
45 DV= DV+(V(L)-VA)**2
SIG3=(ABS(1./9.*DV))**.5*2.

DO 54 L=NC,NC+9
DEV= ABS(VA-V(L))
IF (DEV.LT.SIG3) THEN
KC=KC+1
VN(KC)=V(L)
TN(KC)=T(L)
EX1N(KC)=EX1(L)
EX2N(KC)=EX2(L)
KENN(KC)=KEN(L)
ENDIF
54 CONTINUE
25 CONTINUE
DO 99 KK=1,KC
V(KK)=VN(KK)
T(KK)=TN(KK)
EX1(KK)=EX1N(KK)
EX2(KK)=EX2N(KK)
99 KEN(KK)=KENN(KK)
NP=KC
RETURN

END

```

```

SUBROUTINE SORT (F1,F2,F3,NP,F4,KEN)
DIMENSION F1(NP),F2(NP),F3(NP),F4(NP),KEN(NP)

IS=NP/2

```

```

100 DO 10 J=1,IS
    DO 20 I=J,NP-IS
        K=I
        NT=KEN(I+IS)
        T1=F1(I+IS)
        T2=F2(I+IS)
        T3=F3(I+IS)
        T4=F4(I+IS)

30 IF (K.GE.J) THEN
    IF(NT.GE.KEN(K)) GO TO 60
    KEN(K+IS)=KEN(K)
    F1(K+IS) =F1(K)
    F2(K+IS) =F2(K)
    F3(K+IS) =F3(K)
    F4(K+IS) =F4(K)
    K=K-IS
    GOTO 30
ENDIF

60 KEN(K+IS)=NT
    F1(K+IS)=T1
    F2(K+IS)=T2
    F3(K+IS)=T3
    F4(K+IS)=T4
    K=K-IS
20 CONTINUE
10 CONTINUE

IS=IS/2
IF(IS.GE.1) GOTO 100
RETURN
END

SUBROUTINE GROUP(NP,F1,F2,F3,F4,KEN,NW,F1N,F2N,F3N,F4N,KENN)
DIMENSION F1(NP),F2(NP),F3(NP),F4(NP),KEN(NP),F1N(NP/5)
*,F2N(NP/5),F3N(NP/5),F4N(NP/5),KENN(NP/5)

NF=0
LL=0
II=0

LW=25
NW=1200/LW
IP=LW/2

75 II=II+1
IF(KEN(II).LE.IP) THEN
    GOTO 75
ENDIF
II=II-1

```

```

DO 60 LL=1,NW-1
F1S=0
F2S=0
F3S=0
F4S=0
J=0

40 IP=IP+LW

30 II=II+1
IF(II.GT.NP) GOTO 67
IF (KEN(II).LE.IP) THEN
  J=J+1
  GOTO 30
ELSE
  IF(J.EQ.0) THEN
    NF=NF+1
    KENN(LL)=IP-LW/2

    GOTO 60
  ENDIF
ENDIF

67 II=II-1
IT=II-J+1

DO 80 K=IT,II
  F1S=F1S+F1(K)
  F2S=F2S+F2(K)
  F3S=F3S+F3(K)
80  F4S=F4S+F4(K)

F1N(LL)=F1S/REAL(J)
F2N(LL)=F2S/REAL(J)
F3N(LL)=F3S/REAL(J)
F4N(LL)=F4S/REAL(J)
KENN(LL)=IP-LW/2

IF(NF.GT.0) THEN
  IB=LL-NF
  IF(IB.EQ.0) THEN
    WRITE(*,*)'DATA TOO SPARCE'

  ENDIF

  SLP1=(F1N(LL)-F1N(IB-1))/REAL(LW)/REAL(NF+1)
  SLP2=(F2N(LL)-F2N(IB-1))/REAL(LW)/REAL(NF+1)
  SLP3=(F3N(LL)-F3N(IB-1))/REAL(LW)/REAL(NF+1)
  SLP4=(F4N(LL)-F4N(IB-1))/REAL(LW)/REAL(NF+1)

```

```

DO 90 K=IB,LL-1
F1N(K)=F1N(K-1)+SLP1*REAL(LW)
F2N(K)=F2N(K-1)+SLP2*REAL(LW)
F3N(K)=F3N(K-1)+SLP3*REAL(LW)
90 F4N(K)=F4N(K-1)+SLP4*REAL(LW)
NF=0
ENDIF

60 CONTINUE

JJ=0
F1S=0
F2S=0
F3S=0
F4S=0

KENN(NW)=1200
DO 111 NN=1,NP
IF (KEN(NN).LE.LW/2.OR.KEN(NN).GE.1200-LW/2) THEN
F1S=F1S+F1(NN)
F2S=F2S+F2(NN)
F3S=F3S+F3(NN)
F4S=F4S+F4(NN)
JJ=JJ+1
ENDIF
111 CONTINUE

F1N(NW)=F1S/REAL(JJ)
F2N(NW)=F2S/REAL(JJ)
F3N(NW)=F3S/REAL(JJ)
F4N(NW)=F4S/REAL(JJ)

RETURN
END

SUBROUTINE FORIER(N,M,TIME,X,KT,AZERO,A,B,XSIN,XCOS)
DIMENSION X(N),KT(N),A(M),B(M),XSIN(N),XCOS(N)
PI=3.1416
SUMZ=0.0
DO 100 I=1,N
100 SUMZ=SUMZ+X(I)
AZERO=SUMZ/REAL(N)
DO 300 II=1,M
SUMS=0.0
SUMC=0.0
DO 200 I=1,N
THETA=2.*PI*REAL(KT(I))*REAL(II)/TIME
XCOS(I)=X(I)*COS(THETA)
XSIN(I)=X(I)*SIN(THETA)
SUMS=SUMS+XSIN(I)

```

```

SUMC=SUMC+XCOS(I)
200 CONTINUE
A(I)=2.*SUMC/REAL(N)
B(I)=2.*SUMS/REAL(N)
300 CONTINUE
RETURN
END

SUBROUTINE CONVRT(KX1,KX2,NW,EX1,EX2,CH,BARO,HFA)
DIMENSION EX1(NW),EX2(NW),CH(2)
CHARACTER*12 CH

JJ=1
GOTO (10,20,30,40) KX1

CH(JJ)='VOLTS'
GOTO 100

5 JJ=2
GOTO (10,20,30,40) KX2

CH(JJ)='VOLTS'
GOTO 100

10 CH(JJ)='PRESSURE'

CC=34.06621+BARO*14.696/29.92
DO 15 I=1,NW
IF(JJ.EQ.2) THEN
EX2(I)= (-.00104*ABS(EX2(I))**2.+5.671395*EX2(I)+CC)*6.895
ELSE
EX1(I)= (-.00104*ABS(EX1(I))**2.+5.671395*EX1(I)+CC)*6.895
ENDIF
15 CONTINUE
GOTO 100

20 CH(JJ)='HEAT FLUX'
DO 25 I=1,NW
IF(JJ.EQ.2) THEN
EX2(I)=-1./(.201*10.**(-6))*EX2(I)*3.154/HFA
ELSE
EX1(I)=-1./(.201*10.**(-6))*EX1(I)*3.154/HFA
ENDIF
25 CONTINUE
GOTO 100

30 CH(JJ)='TEMP (THRM)'
DO 35 I=1,NW
IF(JJ.EQ.2) THEN
EX2(I)= EX2(I)*17.022525+EX2(I)**2*(-.2209724)+
* EX2(I)**3*(5.48093E-3)+ EX2(I)**4*(-5.76699E-5)

```

```

ELSE
  EX1(I)= EX1(I)*17.022525+EX1(I)**2*(-.2209724)+
  * EX1(I)**3*(5.48093E-3)+ EX1(I)**4*(-5.76699E-5)
ENDIF
35 CONTINUE
GOTO 100

40 CH(JJ)='TEMP (RTD)'
DO 45 I=1,NW
  IF(JJ.EQ.2) THEN
    EX2(I)=5./9.*(13.13337*EX2(I))-160./9.
  ELSE
    EX1(I)=5./9.*(13.13337*EX1(I))-160./9.
  ENDIF
45 CONTINUE

100 IF (JJ.EQ.1) GOTO 5
RETURN
END

FUNCTION CURV(POS,A0,A,B,M,X)
DIMENSION A(M),B(M),X(M)
CURV=0

DO 20 I=1,M

  X(I)=A(I)*COS(REAL(I)*(6.283185*POS))
  * + B(I)*SIN(REAL(I)*(6.283185*POS))

20 CURV=CURV+X(I)
CURV=CURV+A0
RETURN
CONTINUE
END

```


B.2 Complex Nusselt Number and Phase Shift Program, "NuC1".

```
*****
*
* This program was written in FORTRAN by William A. Grassmyer. It uses the
* equations in Chapter 5 to determine for five harmonics the real and imaginary
* components of the complex-valued Nusselt number and corresponding phase shift
* between heat flux and gas to wall temperature difference.
*
*****
```

```
      DIMENSION V(4000),P(4000),Q(4000),TC(4000),TW(4000),DT(4000)
* ,DTC(4000),DTW(4000),DDT(4000),A(50),B(50),A1(50),B1(50),
* A2(50),B2(50),A3(50),B3(50),A4(50),B4(50),AV1(50),AV2(50),
* BV1(50),BV2(50),XX(50),X(50),A5(50),B5(50),ZQ(50),ZT(50),
* ZH(50),PQ(50),PT(50),DP(50),DPD(50),CNUR(50),CNUI(50)
```

```
      CHARACTER OUT*7,VOLT*3,FL*4,PH*3,D*12
```

```
83 M=5
   CP=1005.
   DEN=1.141
   DK= .0280

   PI=3.14159
   DH=.04445
   QB=-1000000.
   QS=1000000.
   TB=-100000.
   TS=100000.
   DTB=-100000.
   DTS=10000.
```

```
      WRITE(*,*)
      WRITE(*,*)'INPUT THE VOLTAGE OF RUN(EX 050):'
      READ(*,'(A3)') VOLT
```

```
      WRITE(*,*)
      WRITE(*,*)'INPUT POSITION IN FLOW(EX 0200):'
      READ(*,'(A4)') FL
      WRITE(*,*)
      OUT=VOLT//FL
      WRITE(*,*) OUT
```

517 FORMAT(A7)

```
WRITE(*,*)  
WRITE(*,*) 'PHASE ANGLE (EX. 045):'
```

```
READ(*,'(A3)') PH
```

```
OPEN(UNIT=8,FILE='B\COEF\PH\*\*\OUT\*.COF',  
*STATUS='UNKNOWN')
```

```
READ(8,'(////////////////)')
```

```
READ(8,*) JJ,AV10,A01,A02
```

```
C WRITE(*,'(I2,3F9.3)') JJ,AV10,A01,A02
```

```
DO 30 I=1,5
```

```
30 READ(8,*) JJ,AV1(I),BV1(I),A1(I),B1(I),A2(I),B2(I)
```

```
C WRITE(*,'(I2,6F9.3)') JJ,AV1(I),BV1(I),A1(I),B1(I),A2(I),B2(I)
```

```
READ(8,*)
```

```
READ(8,'(A12,F7.4)') D,P1
```

```
C WRITE(*,'(F9.4)') P1
```

```
READ(8,'(////////////////)')
```

```
READ(8,*) JJ,AV20,A03,A04
```

```
C WRITE(*,'(I2,3F9.3)') JJ,AV20,A03,A04
```

```
DO 40 I=1,5
```

```
40 READ(8,*) JJ,AV2(I),BV2(I),A3(I),B3(I),A4(I),B4(I)
```

```
C WRITE(*,'(I2,6F9.3)') JJ,AV2(I),BV2(I),A3(I),B3(I),A4(I),B4(I)
```

```
READ(8,*)
```

```
READ(8,'(A12,F7.4)') D,P2
```

```
C WRITE(*,'(F9.4)') P2
```

```
A0=(AV10+AV20)/2.
```

```
DO 50 I=1,5
```

```
A05=A03-A04
```

```
A5(I)=A3(I)-A4(I)
```

```
B5(I)=B3(I)-B4(I)
```

```
A(I)=(AV1(I)+AV2(I))/2.
```

```
50 B(I)=(BV1(I)+BV2(I))/2.
```

```
PERA=(P1+P2)/2.  
W=1./PERA  
PEW=0.
```

```
DO 12 I=1,1800  
POS=REAL(I)/1800.  
TIM=POS*PERA
```

```
V(I)= CURV(POS,A0,A,B,M,XX)  
P(I)= CURV(POS,A01,A1,B1,M,XX)  
Q(I)= CURV(POS,A02,A2,B2,M,XX)  
TC(I)= CURV(POS,A03,A3,B3,M,XX)  
TW(I)= CURV(POS,A04,A4,B4,M,XX)  
DT(I)=TC(I)-TW(I)
```

```
IF(TC(I).GT.TB) THEN  
  TB=TC(I)  
ENDIF
```

```
IF(TC(I).LT.TS) THEN  
  TS=TC(I)  
ENDIF
```

```
IF(Q(I).GT.QB) THEN  
  QB=Q(I)  
  MQ=I  
ENDIF
```

```
IF(Q(I).LT.QS) THEN  
  QS=Q(I)  
  NQ=I  
ENDIF
```

```
IF(DT(I).GT.DTB) THEN  
  DTB=DT(I)  
  MDT=I  
ENDIF
```

```
IF(DT(I).LT.DTS) THEN  
  DTS=DT(I)  
  NDT=I  
ENDIF
```

```
12 CONTINUE
```

```
QMAX=REAL(MQ)/1800.*360.  
QMIN=REAL(NQ)/1800.*360.  
DTMX=REAL(MDT)/1800.*360.  
DTMN=REAL(NDT)/1800.*360.  
PSMX=DTMX-QMAX
```

```
PSMN=DTMN-QMIN
PEW=PEW/1800.
```

```
REW=W*DH**2/4./(1.566*10.**(-5))
PR =.7
PEW=REW*PR
```

```
WRITE(*,'(/)')
WRITE(*,*)'FREQ= ',W
WRITE(*,*)'PEW = ',PEW
WRITE(*,25) QB,QMAX,QS,QMIN,DTB,DTMX,DTS,DTMN
WRITE(*,26) PSMX,PSMN
```

```
25 FORMAT(/,2X,'QMAX =',F9.3,' AT ',F6.2,' DEG',/,2X,'QMIN =',
*,F9.3,' AT ',F6.2,' DEG',/,2X,'DTMAX=',F9.3,' AT ',F6.2,' DEG'
*,/,2X,'DTMIN=',F9.3,' AT ',F6.2,' DEG')
```

```
26 FORMAT(/,2X,'PHASE SHIFT(MAX)= ',F7.2/,2X,
**'PHASE SHIFT(MIN)= ',F7.2)
```

C*****HARMONIC ANALYSIS OF Q AND DT*****

```
WRITE(*,*)' HARMONIC   PS(DEG)   NUr   NUi   NUC'
```

```
DO 70 I=1,M
```

```
IF(A5(I).EQ.0.) THEN
  A5(I)= 1*10.**(-4)
  WRITE(*,*)'ERROR'
ENDIF
```

```
ZQ(I)= SQRT(A2(I)**2+B2(I)**2)
PQ(I)= ATAN(B2(I)/A2(I))
IF(A2(I).LT.0..AND.B2(I).GT.0.) THEN
  PQ(I)=PQ(I)+PI
ENDIF
IF(A2(I).LT.0..AND.B2(I).LT.0.) THEN
  PQ(I)=PQ(I)-PI
ENDIF
```

```
ZT(I)= SQRT(A5(I)**2+B5(I)**2)
PT(I)= ATAN(B5(I)/A5(I))
```

```
IF(A5(I).LT.0..AND.B5(I).GT.0.) THEN
  PT(I)=PT(I)+PI
ENDIF
```

```

IF(A5(I).LT.0..AND.B5(I).LT.0.) THEN
  PT(I)=PT(I)-PI
ENDIF

```

```

DP(I)= (PQ(I)-PT(I))
IF(DP(I).LT.-PI) THEN
  DP(I)=2.*PI+DP(I)
ENDIF
IF(DP(I).GT.PI) THEN
  DP(I)=DP(I)-2.*PI
ENDIF

```

```

ZH(I)= ZQ(I)/ZT(I)*DH/DK
CNUR(I)= ZH(I)*COS(DP(I))
CNUI(I)= ZH(I)*SIN(DP(I))
DPD(I)=360./(2.*PI)*DP(I)
70 WRITE(*,33) I,DPD(I),CNUR(I),CNUI(I),ZH(I)

```

```

33 FORMAT(6X,I2,4F10.3)

```

```

701 WRITE(*,485)
485 FORMAT(/,5X,'WANT TO RUN AGAIN? ',9X,'1) YES ',9X,'2) NO ',/)
  READ(*,*) NNN
  IF(NNN.EQ.1) GOTO 83

```

```

END

```

```

C*****

```

```

FUNCTION CURV(POS,A0,A,B,M,X)
DIMENSION A(M),B(M),X(M)
PI=3.141593
CURV=0

```

```

DO 20 I=1,M

```

```

  X(I)=A(I)*COS(REAL(I)*(2*PI*POS))
  * + B(I)*SIN(REAL(I)*(2*PI*POS))

```

```

20 CURV=CURV+X(I)
  CURV=CURV+A0
  RETURN
END

```

```

FUNCTION DCRV(POS,A0,A,B,M,DX,W)
DIMENSION A(M),B(M),DX(M)

```

```
PI=3.141593
DCRV=0

DO 20 I=1,M

DX(I)= -A(I)*REAL(I)*2.*PI*W*SIN(REAL(I)*(2.*PI*POS))+
* B(I)*REAL(I)*2.*PI*W*COS(REAL(I)*(2.*PI*POS))

20 DCRV=DCRV+DX(I)
RETURN
END
```

B.3 Turbulence Study Program, "Turb".

```
*****
*
* This program was written in FORTRAN by William A. Grassmyer and takes raw
* velocity data and subtracts the smoothed velocity data determined by "Smoothy"
* and calculates the RMS velocities to enable the researcher to make a study
* of how these velocities are effected by frequency.
*
*****
```

```
CHARACTER*32 INPUT,DI
CHARACTER*12 CH,DV,CR1,CR2
CHARACTER AUTO*11,RUN*5,OUT*7,VOLT*3,FL*4,PH*3
```

```
DIMENSION V(4000),T(4000),EX1(4000),EX2(4000),KEN(4000),CH(2),
*VN(4000),TN(4000),EX1N(4000),EX2N(4000),KENN(4000),EN(4000),
*XSIN(200),XCOS(200),A(20),B(20),A1(20),B1(20),A2(20),B2(20)
*IC(50),XX(20),V1(361),CX1(361),CX2(361),XV(361),XC1(361),
*XC2(361),VS(4000),TURB(4000)
```

```
WRITE(*,*)'INPUT BAROMETRIC PRESSURE(IN. HG):'
READ(*,*) BARO
WRITE(*,*)
```

```
83 WRITE(*,14)
14 FORMAT(/,5X,'COMBINE TWO FILES? ',9X,'1) NO ',9X,'2) YES' ,/)
READ(*,*) LF
IF(LF.NE.1.AND.LF.NE.2) GOTO 83
```

```
WRITE(*,*)
WRITE(*,*)'INPUT THE VOLTAGE OF RUN(EX 050):'
READ(*,'(A3)') VOLT
```

```
WRITE(*,*)
WRITE(*,*)'INPUT POSITION IN FLOW(EX 0200):'
READ(*,'(A4)') FL
WRITE(*,*)
OUT=VOLT//FL
WRITE(*,*) OUT
```

```
C WRITE(*,*)'INPUT NAME OF OUTPUT FILE(EX 0500200):'
C READ(*,517) OUT
517 FORMAT(A7)
```

```
WRITE(*,*)
WRITE(*,*) 'PHASE ANGLE:'
```

```

READ(*,'(A3)') PH
WRITE(*,*) 'DEAD VOLUME:'
READ(*,517) DV
WRITE(*,*) 'OTHER INFO ON DATA (32 CHARACTER MAX):'
READ(*,511) DI
511 FORMAT(A32)

OPEN(UNIT=7,FILE='C:\COEF\PH\^\'//OUT//'.COF',
*STATUS='UNKNOWN')
OPEN(UNIT=9,FILE='C:\CYCLE\PH\^\'//OUT//'.DAT',
*STATUS='UNKNOWN')
OPEN(UNIT=11,FILE='C:\TURB\PH\^\'//OUT//'.DAT',
*STATUS='UNKNOWN')

DO 377 MF=1,LF
WRITE(*,*) 'INPUT NUMBER OF AUTO DIRECTORY (EX 3)'
READ(*,'(A1)') AUTO
518 FORMAT(A11)
WRITE(*,*)

WRITE(*,*) 'INPUT RUN NUMBER OF FILE (EX 07):'
READ(*,'(A2)') RUN
WRITE(*,*)

OPEN(UNIT=3,FILE='C:\DSA4\DSADATA\ASME\AUTO//AUTO//^'
*//RUN//RUN//^DSARAW.TXT',STATUS='OLD')
READ(3,*)

2 FORMAT(/,5X,'ENTER THE CORRECT #:',/,10X,'1) PRESSURE',
*,10X,'2) HEAT FLUX',/,10X,'3) TEMP THERMOCOUPLE',/,10X
*,4) TEMP RTD',/,10X,'5) NO CALIBRATION')
WRITE(*,2)
WRITE(*,3)
3 FORMAT(/,5X,'FOR EXT INPUT #2:')
READ(*,*) KX1
4 FORMAT(/,5X,'FOR EXT INPUT #3:')
WRITE(*,4)
READ(*,*) KX2

NP=1

5 READ(3,*,END=8) V(NP),EN(NP),EX1(NP),EX2(NP),T(NP)
NP=NP+1
GOTO 5

8 NP=NP-1

```



```

      DO 88 I=1,NP
88  KEN(I)=EN(I)

      NOP=NP

      CALL SMOOTH(V,EX1,EX2,T,KEN,NP,VN,TN,EX1N,EX2N,KENN)

C   DO 27 I=1,NP
C 27 WRITE(*,*) KENN(I),VN(I)
C   PTO=NOP-NP
C   WRITE(*,*) PTO,NP
C   PAUSE

      JT=0
      DO 20 IT=2,NP
      IF (KEN(IT)+10.LT.KEN(IT-1)) THEN
          JT=JT+1
          IC(JT)=IT
      ENDIF
20  CONTINUE

      IF(JT.GE.2) GOTO 474

      IF(JT.EQ.1) THEN
          DO 59 I=IC(1),NP
              IF(KEN(2).LE.KEN(I)) THEN
                  PERA=T(I)-T(2)
                  GOTO 889
              ENDIF
59  CONTINUE
      ENDIF
      WRITE(*,*) 'ERROR: ONE FULL PERIOD OF DATA WAS NOT TAKEN'
      GOTO 701

474  PS=0
      DO 63 I=2,JT
          I1=IC(JT-1)
          I2=IC(JT)
          PER=T(I2)-T(I1)
63  PS=PS+PER
          PERA=PS/REAL(JT-1)

889  CONTINUE

C   WRITE(*,*) JT
C   CALL TADJ(

      WRITE(*,*) 'LEAVE ME ALONE DAMMIT! IM SORTING'
      CALL SORT(V,EX1,EX2,NP,T,KEN)

```

```
CALL GROUP(NP,V,EX1,EX2,T,KEN,NW,VN,EX1N,EX2N,TN,KENN)
```

```
CALL CONVRT(KX1,KX2,NW,EX1N,EX2N,CH,BARO)
```

```
M=5  
TIME=1200
```

```
CALL FORIER(NW,M,TIME,VN,KENN,A0,A,B,XSIN,XCOS)
```

```
CALL FORIER(NW,M,TIME,EX1N,KENN,A01,A1,B1,XSIN,XCOS)
```

```
CALL FORIER(NW,M,TIME,EX2N,KENN,A02,A2,B2,XSIN,XCOS)
```

```
C*****OUTPUT*****  
C*****OUTPUT TO 7
```

```
716 FORMAT(/,5X,'DIRECTORY = AUTO',A1,'^RUN',A2,)  
WRITE(*,716) AUTO,RUN  
IF(MF.EQ.1) THEN  
WRITE(*,717) VOLT,FL,PH,DV,BARO,DI  
ENDIF
```

```
717 FORMAT(5X,'VOLTAGE = ',A6/,5X,'FLOW POSN = ',A6/,5X,  
*'PHASE ANGLE= ',A6/,5X,'DEAD VOLUME= ',A10/,5X,  
*'BARO PRESS = ',F7.3/,5X,'NOTE = ',A32)
```

```
WRITE(*,555) CH(1),CH(2)  
555 FORMAT(/,25X,'FOURIER COEFFICIENTS' /,2X,'HARMONIC',8X,  
*'VELOCITY',10X,A12,10X,A12/,16X,'A',7X,'B',12X,'A',8X,'B',  
*12X,'A',8X,'B')
```

```
I=0  
WRITE(*,566) I,A0,A01,A02  
566 FORMAT(4X,I2,6X,F7.3,13X,F8.3,14X,F8.3)
```

```
DO 700 I=1,M  
700 WRITE(*,699) I,A(I),B(I),A1(I),B1(I),A2(I),B2(I)
```

```
699 FORMAT(4X,I2,6X,F7.3,2X,F7.3,4X,F8.3,2X,F8.3,4X,F8.3,2X,F8.3)
```

```
WRITE(*,577) PERA  
577 FORMAT(/,5X,'PERIOD=',F7.4,' SEC')
```

```
C*****OUTPUT TO *.DAT FILE*****
```

```

DO 12 I=1,NW
POS=REAL(KENN(I))/1200.
TIM=POS*PERA
V1(I)= CURV(POS,A0,A,B,M,XX)
CX1(I)= CURV(POS,A01,A1,B1,M,XX)
12 CX2(I)= CURV(POS,A02,A2,B2,M,XX)

```

```

IF(LF.EQ.1) GOTO 323

```

```

C*****COMBINING TWO RUNS*****

```

```

IF(MF.EQ.1) THEN
  CR1=CH(1)
  CR2=CH(2)
  XPER=PERA
  DO 43 I=1,NW
    XV(I)=V1(I)
    XC1(I)=CX1(I)
43   XC2(I)=CX2(I)
  ELSE
    WRITE(9,61) CR1,CR2,CH(1),CH(2)
61   FORMAT(4X,'ENCP',1X,'TIME',7X,'VEL',4X,
*   A10,1X,A10,4X,A10,1X,A10,)

    PERM=(XPER+PERA)/2.
    I=0
    TIM=0
    VA=(XV(NW)+V1(NW))/2.

    WRITE(9,89) I,TIM,VA,XC1(NW),XC2(NW),CX1(NW),CX2(NW)
    DO 47 I=1,NW
      POS=REAL(KENN(I))/1200.
      TIM=POS*PERM
      VA=(XV(I)+V1(I))/2.
47   WRITE(9,89) KENN(I),TIM,VA,XC1(I),XC2(I),CX1(I),CX2(I)
    ENDIF
89   FORMAT(2X,I5,F7.3,5F11.4)

```

```

GOTO 377

```

```

C*****JUST ONE FILE*****

```

```

C*****OUTPUT TO 9*****

```

```

323 WRITE(*,921) CH(1),CH(2)
921 FORMAT(1X,'ENC POS',9X,'TIME',9X,'VELOCITY',7X,A12
*,3X,A12,)

```

```

TIM=0
I=0
WRITE(*,422) I,TIM,V1(NW),CX1(NW),CX2(NW)
DO 324 I=1,NW
POS=REAL(KENN(I))/1200.

```

```

      TIM=POS*PERA
324  WRITE(*,422) KENN(I),TIM,V1(I),CX1(I),CX2(I)

422  FORMAT(2X,I5,4F15.4)

377  CONTINUE

C*****TURBULANCE STUDY*****

585  FORMAT(/,5X,'TURBULANCE STUDY?',/9X,'1) YES',/9X,'2) NO' /)
      WRITE(*,585)
      READ(*,*) NTB
      IF(NTB.EQ.2) GOTO 701

      WRITE(11,716) AUTO,RUN
      FRQ=1./PERA
      WRITE(11,987) FRQ
987  FORMAT(5X,'FREQUENCY= ',F7.5,' HZ' /)
      WRITE(11,922)
922  FORMAT(1X,'ENC POS',9X,'TIME',9X,'TURBULANCE',3X,
      *'VELOCITY REAL',3X,'VELOCITY SMTH' /)
      DO 121 I=1,NP
      POS=REAL(KEN(I))/1200.
      TIM=POS*PERA
      VS(I)= CURV(POS,A0,A,B,M,XX)
      TURB(I)= V(I)-VS(I)
      DEG=.30*REAL(KEN(I))
121  WRITE(11,423) DEG,TIM,TURB(I),V(I),VS(I)

423  FORMAT(2X,F5.1,4F15.4)

701  WRITE(*,485)
485  FORMAT(/,5X,'WANT TO RUN AGAIN?',/9X,'1) YES',/9X,'2) NO' /)
      READ(*,*) NNN
      IF(NNN.EQ.1) GOTO 83

      END

```

C*****SUBROUTINES START HERE*****

```

      SUBROUTINE SMOOTH(V,EX1,EX2,T,KEN,NP,VN,TN,EX1N,EX2N,KENN)

      DIMENSION V(NP),T(NP),EX1(NP),EX2(NP),KEN(NP),VN(NP),TN(NP)
      *,EX1N(NP),EX2N(NP),KENN(NP)

      IN=NP/10.
      NC=-9
      KC=0

```

```

DO 25 K=1,IN-1
NC=NC+10
VS=0.
DV=0.

DO 35 L=NC,NC+9
35 VS= VS+V(L)
VA=VS/10.

DO 45 L=NC,NC+9
45 DV= DV+(V(L)-VA)**2
SIG3=(ABS(1./9.*DV))**.5*2.

DO 54 L=NC,NC+9
DEV= ABS(VA-V(L))
IF (DEV.LT.SIG3) THEN
KC=KC+1
VN(KC)=V(L)
TN(KC)=T(L)
EX1N(KC)=EX1(L)
EX2N(KC)=EX2(L)
KENN(KC)=KEN(L)
ENDIF
54 CONTINUE
25 CONTINUE
DO 99 KK=1,KC
V(KK)=VN(KK)
T(KK)=TN(KK)
EX1(KK)=EX1N(KK)
EX2(KK)=EX2N(KK)
99 KEN(KK)=KENN(KK)
NP=KC
RETURN

END

SUBROUTINE SORT (F1,F2,F3,NP,F4,KEN)
DIMENSION F1(NP),F2(NP),F3(NP),F4(NP),KEN(NP)

IS=NP/2

100 DO 10 J=1,IS
DO 20 I=J,NP-IS
K=I
NT=KEN(I+IS)
T1=F1(I+IS)
T2=F2(I+IS)
T3=F3(I+IS)
T4=F4(I+IS)

```

```

30 IF (K.GE.J) THEN
    IF(NT.GE.KEN(K)) GO TO 60
    KEN(K+IS)=KEN(K)
    F1(K+IS) =F1(K)
    F2(K+IS) =F2(K)
    F3(K+IS) =F3(K)
    F4(K+IS) =F4(K)
    K=K-IS
    GOTO 30
ENDIF

```

```

60 KEN(K+IS)=NT
F1(K+IS)=T1
F2(K+IS)=T2
F3(K+IS)=T3
F4(K+IS)=T4
K=K-IS
20 CONTINUE
10 CONTINUE

```

```

IS=IS/2
IF(IS.GE.1) GOTO 100
RETURN
END

```

```

SUBROUTINE GROUP(NP,F1,F2,F3,F4,KEN,NW,F1N,F2N,F3N,F4N,KENN)
DIMENSION F1(NP),F2(NP),F3(NP),F4(NP),KEN(NP),F1N(NP/5)
*,F2N(NP/5),F3N(NP/5),F4N(NP/5),KENN(NP/5)

```

```

NF=0
LL=0
II=0

```

```

LW=25
NW=1200/LW
IP=LW/2

```

```

75 II=II+1
IF(KEN(II).LE.IP) THEN
    GOTO 75
ENDIF
II=II-1

```

```

DO 60 LL=1,NW-1
F1S=0
F2S=0
F3S=0
F4S=0
J=0

```

```

40 IP=IP+LW

```

```

30 II=II+1

  IF (KEN(II).LE.IP) THEN
    J=J+1
    GOTO 30
  ELSE
    IF(J.EQ.0) THEN
      NF=NF+1
      KENN(LL)=IP-LW/2

      GOTO 60
    ENDIF
  ENDIF

  II=II-1
  IT=II-J+1

  DO 80 K=IT,II
    F1S=F1S+F1(K)
    F2S=F2S+F2(K)
    F3S=F3S+F3(K)
80  F4S=F4S+F4(K)

  F1N(LL)=F1S/REAL(J)
  F2N(LL)=F2S/REAL(J)
  F3N(LL)=F3S/REAL(J)
  F4N(LL)=F4S/REAL(J)
  KENN(LL)=IP-LW/2

  IF(NF.GT.0) THEN
    IB=LL-NF
    SLP1=(F1N(LL)-F1N(IB-1))/REAL(LW)/REAL(NF+1)
    SLP2=(F2N(LL)-F2N(IB-1))/REAL(LW)/REAL(NF+1)
    SLP3=(F3N(LL)-F3N(IB-1))/REAL(LW)/REAL(NF+1)
    SLP4=(F4N(LL)-F4N(IB-1))/REAL(LW)/REAL(NF+1)

    DO 90 K=IB,LL-1
      F1N(K)=F1N(K-1)+SLP1*REAL(LW)
      F2N(K)=F2N(K-1)+SLP2*REAL(LW)
      F3N(K)=F3N(K-1)+SLP3*REAL(LW)
90  F4N(K)=F4N(K-1)+SLP4*REAL(LW)
    NF=0
  ENDIF

60 CONTINUE

  JJ=0
  F1S=0
  F2S=0
  F3S=0

```

```

F4S=0

KENN(NW)=1200
DO 111 NN=1, NP
IF (KEN(NN).LE.LW/2.OR.KEN(NN).GE.1200-LW/2) THEN
  F1S=F1S+F1(NN)
  F2S=F2S+F2(NN)
  F3S=F3S+F3(NN)
  F4S=F4S+F4(NN)
  JJ=JJ+1
ENDIF
111 CONTINUE

F1N(NW)=F1S/REAL(JJ)
F2N(NW)=F2S/REAL(JJ)
F3N(NW)=F3S/REAL(JJ)
F4N(NW)=F4S/REAL(JJ)

RETURN
END

SUBROUTINE FORIER(N,M,TIME,X,KT,AZERO,A,B,XSIN,XCOS)
DIMENSION X(N),KT(N),A(M),B(M),XSIN(N),XCOS(N)
PI=3.1416
SUMZ=0.0
DO 100 I=1,N
100 SUMZ=SUMZ+X(I)
AZERO=SUMZ/REAL(N)
DO 300 II=1,M
SUMS=0.0
SUMC=0.0
DO 200 I=1,N
THETA=2.*PI*REAL(KT(I))*REAL(II)/TIME
XCOS(I)=X(I)*COS(THETA)
XSIN(I)=X(I)*SIN(THETA)
SUMS=SUMS+XSIN(I)
SUMC=SUMC+XCOS(I)
200 CONTINUE
A(II)=2.*SUMC/REAL(N)
B(II)=2.*SUMS/REAL(N)
300 CONTINUE
RETURN
END

SUBROUTINE CONVRT(KX1,KX2,NW,EX1,EX2,CH,BARO)
DIMENSION EX1(NW),EX2(NW),CH(2)
CHARACTER*12 CH

JJ=1
GOTO (10,20,30,40) KX1

```



```

CH(JJ)='VOLTS'
GOTO 100

5 JJ=2
GOTO (10,20,30,40) KX2

CH(JJ)='VOLTS'
GOTO 100

10 CH(JJ)='PRESSURE'

CC=34.06621+BARO*14.696/29.92
DO 15 I=1,NW
IF(JJ.EQ.2) THEN
EX2(I)= -.00104*ABS(EX2(I))**2.+5.671395*EX2(I)+CC
ELSE
EX1(I)= -.00104*ABS(EX1(I))**2.+5.671395*EX1(I)+CC
ENDIF
15 CONTINUE
GOTO 100

20 CH(JJ)='HEAT FLUX'
DO 25 I=1,NW
IF(JJ.EQ.2) THEN
EX2(I)=200./222*EX2(I)*3.154
ELSE
EX1(I)=200./222*EX1(I)*3.154
ENDIF
25 CONTINUE
GOTO 100

30 CH(JJ)='TEMP (THRM)'
DO 35 I=1,NW
IF(JJ.EQ.2) THEN
EX2(I)= EX2(I)*17.022525+EX2(I)**2*(-.2209724)+
* EX2(I)**3*(5.48093E-3)+ EX2(I)**4*(-5.76699E-5)
ELSE
EX1(I)= EX1(I)*17.022525+EX1(I)**2*(-.2209724)+
* EX1(I)**3*(5.48093E-3)+ EX1(I)**4*(-5.76699E-5)
ENDIF
35 CONTINUE
GOTO 100

40 CH(JJ)='TEMP (RTD)'
DO 45 I=1,NW
IF(JJ.EQ.2) THEN
EX2(I)=13.13337*EX2(I)
ELSE
EX1(I)=13.13337*EX1(I)
ENDIF
45 CONTINUE

```

```
100 IF (JJ.EQ.1) GOTO 5
    RETURN
    END

    FUNCTION CURV(POS,A0,A,B,M,X)
    DIMENSION A(M),B(M),X(M)
    CURV=0

    DO 20 I=1,M

    X(I)=A(I)*COS(REAL(I)*(6.283185*POS))
    * + B(I)*SIN(REAL(I)*(6.283185*POS))

20 CURV=CURV+X(I)
    CURV=CURV+A0
    RETURN
    END
```

B.4 Velocity Profile Creation Program, "Phase5".

```

*****
*
* This program is written in BASIC by Charles E. Dean. It takes the smoothed
* velocity data that "Smoothy" generates and for each positional file across
* the radius of the test section it extracts the velocity data at each crank
* angle 30° apart for 360°.
*
*****

      CLS
      DIM A(100), B(100), C(100), D(100), E(100), F(100), G(100), H(100), I(100)
40    PRINT "WE WILL NOW CONSTRUCT THE PHASE FILE FOR THIS          VOLTAGE
EXPERIMENT"
49    PRINT ""
      INPUT "TYPE VOLTAGE OF THIS EXPERIMENT (50)"; BB$
50    INPUT "TYPE POSITION OF THIS FILE IN MILS (0200)"; XY$
      INPUT "PLEASE TYPE MIL POSITION AGAIN (0200)"; LM
      OPEN "B:\\" + BB$ + XY$ + ".DAT" FOR INPUT AS #1
      FOR Y = 1 TO 50
        INPUT #1, A(Y), B(Y), C(Y), D(Y), E(Y)
        REM PRINT C(Y), D(Y), E(Y)
      NEXT Y
      REM PRINT A(3), A(5), A(10), A(30), A(44)
      REM 90
      OPEN "B:\\" + BB$ + "PHA.DAT" FOR OUTPUT AS #30
      LET H$ = "#.#####   ##.#####   ##.#####   ##.#####   ##.#####   ##.#####   ##.#####
      ##.#####   ##.#####   ##.#####   ##.#####   ##.#####   ##.#####   "
      PRINT #30, USING H$; LM / 875; A(3), A(7), A(11), A(15), A(19), A(23), A(27),
        A(31), A(35), A(39), A(43), A(47), A(3)
      PRINT USING H$; LM / 875; A(3); A(7); A(11); A(15); A(19); A(23); A(27);
        A(31); A(35); A(39); A(43); A(47); A(3)
      CLOSE #1
      CLOSE #30
      REM END
85    PRINT ""
      INPUT "DO YOU HAVE ANOTHER FILE AT THIS VOLTAGE TO ADD? (1)
        YES, (2) NO"; X
      IF X = 2 GOTO 80
51    INPUT "TYPE POSITION OF THIS FILE IN MILS (0200)"; XY$
      INPUT "PLEASE TYPE MIL POSITION AGAIN (0200)"; LM
      OPEN "B:" + BB$ + XY$ + ".DAT" FOR INPUT AS #1
      FOR Y = 1 TO 50
        INPUT #1, A(Y), B(Y), C(Y), D(Y), E(Y)
        REM PRINT C(Y), D(Y), E(Y)

```

```

NEXT Y
OPEN "B:\\" + BB$ + "PHA.DAT" FOR APPEND AS #30
LET H$ = ".##### ###.#### ###.#### ###.#### ###.#### ###.#### ###.#### ###.####"
#####.#####.#####.#####.#####.#####"
PRINT #30, USING H$; LM / 875; A(3), A(7), A(11), A(15), A(19), A(23), A(27),
A(31), A(35), A(39), A(43), A(47), A(3)
PRINT USING H$; LM / 875; A(3); A(7); A(11); A(15); A(19); A(23); A(27);
A(31); A(35); A(39); A(43); A(47); A(3)
CLOSE #1
CLOSE #30
GOTO 85
80 PRINT ""
PRINT "CONGRATULATIONS! YOU HAVE MADE YOUR PHASE FILE FOR
THIS VOLTAGE"
PRINT ""
INPUT "DO YOU WISH TO MAKE ANOTHER VOLTAGE'S PHASE FILE? (1)
YES, (2) NO"; GF
IF GF = 1 GOTO 49
90 END

```

B.5 Theoretical Velocity Profile Creation Program, "White".

```

*****
*
* This program was written in BASIC by Charles E. Dean. It produces theoretical
* velocity profiles based upon F. White's solution to the momentum equation for
* periodic flow in a pipe 1.75" in inner diameter. The equations came from White's
* book Viscous Fluid Flow (1991).
*
*****

8   CLS
    REM   PROGRAM NAME IS: PROFILE.BAS
    REM   THIS PROGRAM WAS WRITTEN BY CHARLES E. DEAN

    REM           THIS PROGRAM CALCULATES MAX VELOCITIES, NOT
                NORMALIZED ONES

9   PRINT "*****"
10  PRINT "*** THIS PROGRAM PRODUCES THEORETICAL VELOCITY ***"
20  PRINT "*** PROFILES BASED ON F. WHITE'S SOLN OF THE ***"
21  PRINT "*** MOMENTUM EQUATION FOR A 1.75 INCH ID PIPE ***"
22  PRINT "*****"
    PRINT ""
30  INPUT " WHAT FREQ (HZ) DO YOU WANT TO STUDY?"; A
32  INPUT " PLEASE SPECIFY THE FREQ MULT BY 1000"; C$
34  INPUT " WHAT IS THE MAXIMUM CENTERLINE VELOCITY"; Y
40  W = 2 * 3.141593 * A
50  V = 1.566E-05
60  R = .022225
70  REW = W * R ^ 2 / V
80  PRINT "Rew ="; REW; "AT YOUR FREQUENCY OF"; A; "HZ"
90  P = 1 / A
100 T = P / 12
105 E = 0
    REM E = TIME STEP
106 F = -1
    REM F = RADIAL POSITION
110 PRINT "THE SYSTEM WILL COMPLETE ONE OSCILLATION IN"; P;
    "SECONDS"
120 OPEN "b:\" + C$ + "HZ.DAT" FOR OUTPUT AS #1
130 DIM A(2000), B(2000), C(2000), D(2000), E(2000), F(2000), G(2000), H(2000),
    I(2000)
140 IF REW > 4 GOTO 400
150 FOR I = 1 TO 1001
    B(I) = Y * ((1 - ((REW) ^ 2)) * COS(W * E) + (REW / 16) * ((F / R) ^ 4 + 4 * (F / R) ^ 2 - 5)

```

```

* SIN(W * E))
  F = F + .000022225#
  NEXT I
  PRINT E
  E = E + T
  F = 0
160  FOR I = 1 TO 1001
      C(I) = Y * ((1 - ((REW) ^ 2)) * COS(W * E) + (REW / 16) * ((F / R) ^ 4 + 4 * (F / R) ^ 2 - 5)
* SIN(W * E))
      F = F + .000022225#
      NEXT I
      PRINT E
      E = E + T
      F = 0
170  FOR I = 1 TO 1001
      D(I) = Y * ((1 - ((REW) ^ 2)) * COS(W * E) + (REW / 16) * ((F / R) ^ 4 + 4 * (F / R) ^ 2 - 5)
* SIN(W * E))
      F = F + .000022225#
      NEXT I
      PRINT E
      E = E + T
      F = 0
180  FOR I = 1 TO 1001
      E(I) = Y * ((1 - ((REW) ^ 2)) * COS(W * E) + (REW / 16) * ((F / R) ^ 4 + 4 * (F / R) ^ 2 - 5) *
SIN(W * E))
      F = F + .000022225#
      NEXT I
      PRINT E
      E = E + T
      F = 0
190  FOR I = 1 TO 1001
      F(I) = Y * ((1 - ((REW) ^ 2)) * COS(W * E) + (REW / 16) * ((F / R) ^ 4 + 4 * (F / R) ^ 2 - 5) *
SIN(W * E))
      F = F + .000022225#
      NEXT I
      PRINT E
      E = E + T
      F = 0
200  FOR I = 1 TO 1001
      G(I) = Y * ((1 - ((REW) ^ 2)) * COS(W * E) + (REW / 16) * ((F / R) ^ 4 + 4 * (F / R) ^ 2 - 5) *
SIN(W * E))
      F = F + .000022225#
      NEXT I
      PRINT E
      E = E + T
      F = 0
210  FOR I = 1 TO 1001
      H(I) = Y * ((1 - ((REW) ^ 2)) * COS(W * E) + (REW / 16) * ((F / R) ^ 4 + 4 * (F / R) ^ 2 - 5)
* SIN(W * E))
      F = F + .000022225#
      NEXT I

```

```

PRINT E
E = E + T
F = 0
220 REM FOR I = 1 TO 1001
REM I(I) = Y * ((1 - ((REW) ^ 2)) * COS(W * E) + (REW / 16) * ((F / R) ^ 4 + 4 * (F / R) ^ 2 -
5) * SIN(W * E))
REM F = F + .000022225#
REM NEXT I
REM PRINT E
REM E = E + T
REM F = 0
REM 230 FOR I = 1 TO 1001
REM I(I) = (1 - ((REW) ^ 2)) * COS(W * E) + (REW / 16) * ((F / R) ^ 4 + 4 * (F / R) ^ 2 - 5) *
SIN(W * E)
REM F = F + .000022225#
REM NEXT I
REM PRINT E
REM E = E + T
REM F = 0
FOR I = 1 TO 1001
A(I) = -1 + F / R
F = F + .000022225#
NEXT I
FOR I = 1 TO 1001
PRINT #1, A(I), B(I), C(I), D(I), E(I), F(I), G(I), H(I)
REM PRINT A(I); B(I); C(I); D(I); E(I); F(I); G(I); H(I)
NEXT I
CLOSE #1
GOTO 500
400 F = .00001
E = 0

420 FOR I = 1 TO 1001
B = (1 - F / R) * (REW / 2) ^ .5
B(I) = Y * ((4 / REW) * (SIN(W * E) - (EXP(-B) / (F / R) ^ .5) * SIN(W * E - B)))

F = F + .000022225#
NEXT I
PRINT E
E = E + T
F = .00001
430 FOR I = 1 TO 1001
B = (1 - F / R) * SQR(REW / 2)
C(I) = Y * ((4 / REW) * (SIN(W * E) - (EXP(-B) / SQR(F / R)) * SIN(W * E - B)))

F = F + .000022225#
NEXT I
PRINT E
E = E + T
F = .00001
440 FOR I = 1 TO 1001

```

```

B = (1 - F / R) * SQR(REW / 2)
D(I) = Y * ((4 / REW) * (SIN(W * E) - (EXP(-B) / SQR(F / R)) * SIN(W * E - B)))

F = F + .000022225#
NEXT I
PRINT E
E = E + T
F = .00001
450  FOR I = 1 TO 1001
      B = (1 - F / R) * SQR(REW / 2)
      E(I) = Y * ((4 / REW) * (SIN(W * E) - (EXP(-B) / SQR(F / R)) * SIN(W * E - B)))

      F = F + .000022225#
      NEXT I
      PRINT E
      E = E + T
      F = .00001
460  FOR I = 1 TO 1001
      B = (1 - F / R) * SQR(REW / 2)
      F(I) = Y * ((4 / REW) * (SIN(W * E) - (EXP(-B) / SQR(F / R)) * SIN(W * E - B)))

      F = F + .000022225#
      NEXT I
      PRINT E
      E = E + T
      F = .00001
470  FOR I = 1 TO 1001
      B = (1 - F / R) * SQR(REW / 2)
      G(I) = Y * ((4 / REW) * (SIN(W * E) - (EXP(-B) / SQR(F / R)) * SIN(W * E - B)))

      F = F + .000022225#
      NEXT I
      PRINT E
      E = E + T
      F = .00001
480  FOR I = 1 TO 1001
      B = (1 - F / R) * SQR(REW / 2)
      H(I) = Y * ((4 / REW) * (SIN(W * E) - (EXP(-B) / SQR(F / R)) * SIN(W * E - B)))
      F = F + .000022225#

      NEXT I
      PRINT E
      E = E + T
      F = .00001
REM 490  FOR I = 1 TO 1001
      REM  B = (1 - F / R) * SQR(REW / 2)
      REM  I(I) = (4 / REW) * (SIN(W * E) - (EXP(-B) / SQR(F / R)) * SIN(W * E - B))
      REM  F = F + .000022225#
      REM  NEXT I
      REM  PRINT E
      REM  E = E + T

```



```
REM F = 0
  FOR I = 1 TO 1001
    A(I) = -1 + F / R
    F = F + .000022225#
  NEXT I
  FOR I = 1 TO 1001
    PRINT #1, A(I), B(I), C(I), D(I), E(I), F(I), G(I), H(I), I(I)
    REM PRINT A(I); B(I); C(I); D(I); E(I); F(I); G(I); H(I)
  NEXT I
  CLOSE #1
500 INPUT "DO YOU WISH TO CALCULATE ANOTHER PROFILE? (1) YES, (2)
      NO";Z
  IF Z = 1 GOTO 30
  END
```

Appendix C

Calculation of Beam Refractance Due To Window

This appendix determines what distance P the probe volume is either moved away from the transceiver or toward the transceiver due to refractance through the glass window as the probe volume is traversed across the diameter of the glass pipe within the test section. For this analysis the indices of refractance for Pyrex glass and air are assumed to be 1.5 and 1.0, respectively.

If the two beams properly intersect the glass window along its crest as described in Chapter 3, the window appears to each beam as a flat plate of glass, 1.90 mm thick. Figure C.1 depicts the geometry and the nomenclature for this analysis.

By using Snell's First Law, we can determine θ_1 and θ_2 :

$$\text{Snell's First Law : } n_1 \sin\theta_1 = n_2 \sin\theta_2 \quad (\text{C.1})$$

$$\tan\theta_1 = \frac{h}{250} = \frac{20}{250} \Rightarrow \theta_1 = 4.5739^\circ$$

$$\sin\theta_2 = \frac{\sin(\theta_1)}{1.5} \Rightarrow \theta_2 = 3.0475^\circ$$

Furthermore, through the use of simple geometry we can solve for Q and R:

$$\tan\theta_1 = \frac{R}{t} = \frac{R}{1.90\text{mm}} \Rightarrow R = .152 \text{ mm}$$

$$\tan\theta_2 = \frac{Q}{t} = \frac{Q}{1.90\text{mm}} \Rightarrow Q = .10115 \text{ mm}$$

Geometrically we can also write two equations for $\tan\theta_1$:

$$\tan\theta_1 = \frac{Z-R}{L} \quad (\text{C.2})$$

$$\text{similarly, } \tan\theta_1 = \frac{Z-Q}{K} \quad (\text{C.3})$$

We can equate these two equations to get:

$$\frac{Z-R}{L} = \frac{Z-Q}{K} \quad (\text{C.4})$$

From Figure C.1 we can write an equation for length L:

$$L = 250 - B - t = 248.1 - B \quad (\text{C.5})$$

By using Equation C.5 we can rewrite Equation C.4 and solve for length K:

$$\frac{Z-R}{(248.1-B)} = \frac{Z-Q}{K} \Rightarrow K = \frac{(Z-Q)(248.1-B)}{(Z-R)} \quad (\text{C.6})$$

But what we are really after is P as a function of B, so we can write:

$$P = K - L = K - (248.1 - B) = (248.1 - B) \left[\frac{(Z-Q)}{(Z-R)} - 1 \right] \quad (\text{C.7})$$

In Equation C.7, the unknowns are P, B, and Z. By using similar triangles as depicted in Figure C.2, we can solve for Z in terms of B.

$$\text{since } \tan\theta_1 = \tan\theta_1 \Rightarrow \frac{h}{250} = \frac{Z}{250-B}$$

$$Z = \frac{20(250-B)}{250}$$

$$Z = .08(250-B)$$

We can now rewrite Equation C.7:

$$P = (248.1-B) \left[\frac{.08(250-B) - .10115}{.08(250-B) - .15200} - 1 \right] \quad (\text{C.8})$$

Using this result, we find that P remains constant at 6.36 mm (25.0246 thousandths of an inch).

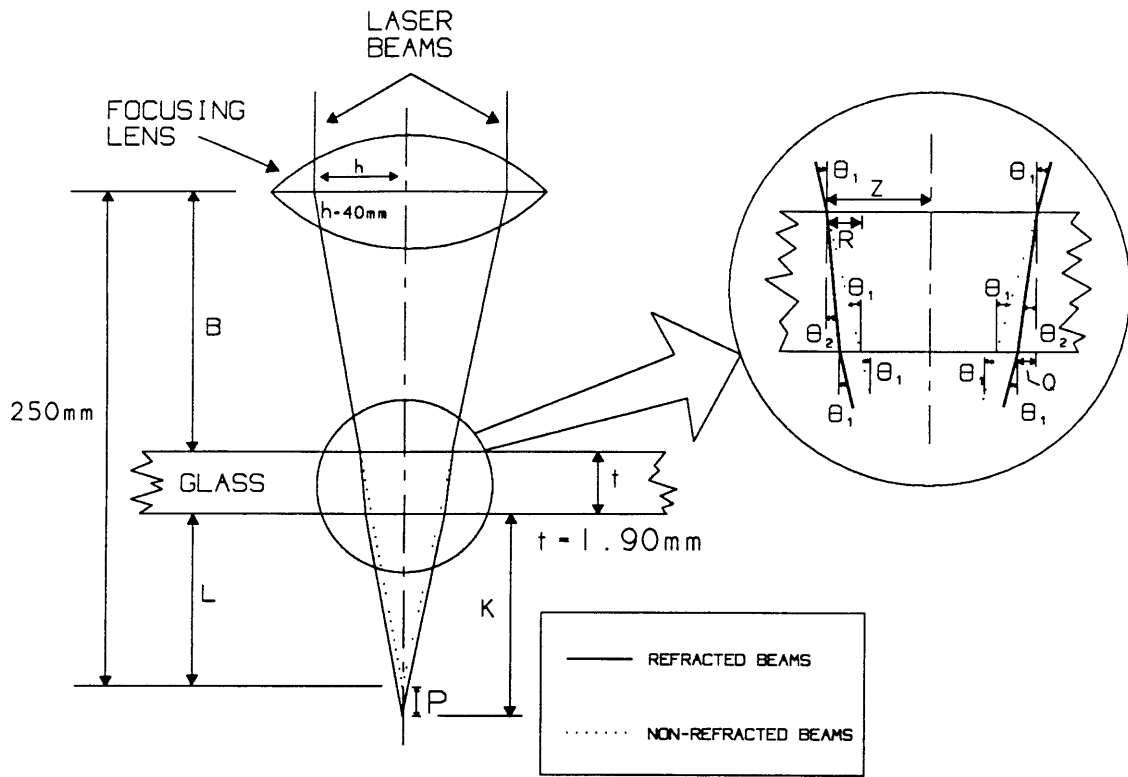


Figure C.1 Geometry of Refractance Analysis

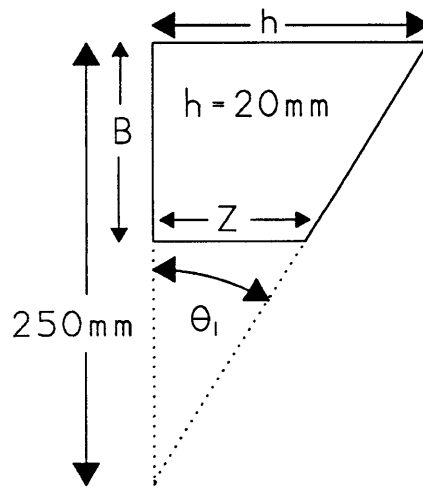


Figure C.2 Similar Triangles

Appendix D

Baseline Data

Run #	t	r_p	ψ	Pe_c	Volts	Q_{max}	T_{max}	Nu_c	Nu_r	Nu_i	$\Delta\phi$
A4RUN3637	0.33	2.29	0	46.43	L100	228.91	73.51	16.25	15.17	-5.82	-21.01
A4RUN3938	0.61	2.33	0	85.83	L150	347.82	70.68	17.48	13.26	-11.40	-40.68
A4RUN4041	0.82	2.34	0	115.38	L200	363.60	61.96	20.28	11.42	-16.77	-55.73
A4RUN4342	0.96	2.35	0	135.08	L240	437.47	39.26	22.45	8.49	-20.78	-67.77
A4RUN6667	1.63	2.38	0	228.36	H50	629.92	72.10	44.45	7.19	-43.87	-80.70
A4RUN6564	3.04	2.40	0	427.76	H100	772.11	69.25	72.98	-4.98	-72.00	-97.07
A4RUN6263	5.07	2.41	0	713.41	H150	1462.15	77.07	110.73	5.74	43.00	-87.03
A4RUN6160	6.57	2.44	0	924.48	H200	1742.50	64.67	173.70	-51.00	-110.59	-107.08
A4RUN5859	8.25	2.44	0	1160.87	H250	2455.14	68.53	233.60	-50.17	-166.04	-102.40
A4RUN9091	0.35	2.11	45	49.25	L100	524.87	59.52	32.92	31.39	-228.15	17.54
A4RUN9392	0.51	2.12	45	71.76	L150	938.10	51.13	47.96	47.60	5.92	7.05
A4RUN9495	0.72	2.13	45	101.31	L200	1446.08	49.07	60.51	58.99	5.90	12.89
A4RUN9796	0.93	2.14	45	130.86	L240	1689.47	57.21	46.20	43.93	13.50	18.07
A4RUN7071	1.55	2.28	45	218.10	H50	1717.04	52.46	54.49	52.21	14.33	-16.66
A4RUN7372	3.24	2.30	45	455.91	H100	3120.31	39.44	129.29	106.03	-15.62	-34.91
A4RUN7475	5.33	2.43	45	750.00	H150	4008.81	50.71	181.75	166.20	-73.55	-23.87
A4RUN2324	0.21	1.68	90	29.55	L50	947.09	83.58	13.71	13.28	3.42	14.45
ASRUN2625	0.32	2.01	90	45.03	L100	1128.13	92.49	27.00	25.73	8.49	18.27
ASRUN2728	0.60	2.02	90	84.43	L150	1487.83	91.58	35.99	34.24	11.09	17.95
ASRUN3029	0.73	2.03	90	102.72	L200	1677.25	88.06	43.79	42.59	10.18	13.44
ASRUN3132	0.88	2.03	90	123.83	L240	1954.20	88.39	48.22	47.50	8.28	9.89
ASRUN2212	1.22	1.98	90	171.67	H50	2596.83	52.78	86.60	86.46	-5.00	-3.31
ASRUN2013	2.53	2.07	90	356.00	H100	5254.26	52.39	142.45	141.85	-13.05	-5.26
ASRUN2116	4.02	2.37	90	647.00	H150	7231.79	58.21	244.59	244.34	-10.99	-2.58
ASRUN4344	0.23	1.91	135	32.36	L50	1012.17	64.17	29.39	28.90	4.91	9.63
ASRUN4645	0.35	1.94	135	49.24	L100	1398.83	61.74	49.66	49.24	6.42	7.42
ASRUN4748	0.51	1.95	135	71.76	L150	1664.39	61.43	68.67	67.92	-11.37	-9.50
ASRUN5049	0.72	1.98	135	101.31	L200	1916.58	62.10	68.52	68.34	-4.89	-4.09
ASRUN5152	0.93	1.99	135	130.86	L240	2128.89	68.29	67.42	66.04	13.56	11.60
ASRUN5453	1.47	1.91	135	206.85	H50	1012.17	64.17	29.39	28.90	4.91	9.63
ASRUN5556	3.71	2.02	135	522.04	H100	6876.51	75.24	188.85	188.45	-12.37	-3.76
ASRUN5857	6.81	2.09	135	958.25	H150	8120.60	83.64	335.07	330.86	1.95	0.49

Table D.1: Baseline Data for the First Harmonic Fit of the Smoothed Data

Run #	t	r_p	ψ	Pe_c	Volts	Q_{max}	T_{max}	Nu_c	Nu_r	Nu_i	$\Delta\phi$
A4RUN3637	0.66	2.29	0	92.86	L100	228.91	73.51	16.87	12.83	-10.94	-40.46
A4RUN3938	1.22	2.33	0	171.66	L150	347.82	70.68	23.13	15.78	-16.92	-47.81
A4RUN4041	1.64	2.34	0	230.76	L200	363.60	61.96	32.51	17.18	-27.60	-58.10
A4RUN4342	1.92	2.35	0	270.16	L240	437.47	39.26	64.11	-20.96	-60.58	64.11
A4RUN6667	3.26	2.38	0	458.72	H50	629.92	72.10	85.22	-16.66	-83.98	-181.28
A4RUN6564	6.08	2.40	0	855.52	H100	772.11	69.25	126.47	-76.36	-108.82	-127.14
A4RUN6263	10.14	2.41	0	1426.82	H150	1462.15	77.07	208.26	42.89	-264.93	-80.97
A4RUN6160	13.14	2.44	0	1848.96	H200	1742.50	64.67	482.06	14.76	-481.83	-88.25
A4RUN5859	16.90	2.44	0	2321.74	H250	2455.14	68.53	597.61	-31.88	-596.61	-93.60
A4RUN9091	0.70	2.11	45	98.50	L100	524.87	59.52	45.22	42.48	15.90	20.85
A4RUN9392	1.02	2.12	45	143.52	L150	938.10	51.13	55.69	55.57	3.66	3.77
A4RUN9495	1.44	2.13	45	202.62	L200	1446.08	49.07	66.99	83.68	-22.23	-14.88
A4RUN9796	1.86	2.14	45	261.72	L240	1689.47	57.21	77.82	75.53	-15.08	-11.29
A4RUN7071	3.10	2.28	45	436.20	H50	1717.04	52.46	128.08	56.44	-105.90	-61.94
A4RUN7372	6.48	2.30	45	911.82	H100	3120.31	39.44	337.59	53.08	-333.99	-80.95
A4RUN7475	10.66	2.43	45	1508.00	H150	4008.81	50.71	523.11	274.25	-170.84	-31.92
ASRUN2324	0.42	1.68	90	59.10	L50	947.09	83.58	54.90	54.41	3.18	3.35
ASRUN2625	0.64	2.01	90	90.86	L100	1128.13	92.49	19.19	17.53	-7.81	-24.82
ASRUN2728	1.20	2.02	90	168.86	L150	1487.83	91.58	48.95	38.65	-13.53	-19.29
ASRUN3029	1.46	2.03	90	205.44	L200	1677.25	88.06	54.00	52.72	-11.69	-12.90
ASRUN3132	1.76	2.03	90	247.66	L240	1954.20	88.39	71.40	68.09	-21.49	-17.52
ASRUN2212	2.44	1.98	90	343.34	H50	2596.83	52.78	281.40	193.80	204.14	46.40
ASRUN2013	5.06	2.07	90	712.00	H100	5254.26	52.39	573.55	540.55	-191.73	-19.53
ASRUN2116	12.04	2.37	90	1694.16	H150	7231.79	58.21	644.29	124.32	-632.18	-78.87
ASRUN4344	0.46	1.91	135	64.72	L50	1012.17	64.17	36.98	21.00	30.38	53.23
ASRUN4645	0.70	1.94	135	98.48	L100	1398.83	61.74	48.10	48.03	-2.29	-3.27
ASRUN4748	1.02	1.95	135	143.52	L150	1664.39	61.43	56.96	56.24	-9.08	-9.89
ASRUN5049	1.44	1.98	135	202.62	L200	1916.58	62.10	67.65	64.72	-19.70	-16.93
ASRUN5152	1.86	1.99	135	261.72	L240	2128.89	68.29	120.63	118.39	-23.16	-11.87
ASRUN5453	2.94	1.91	135	413.70	H50	1012.17	64.17	36.98	21.00	30.38	53.23
ASRUN5556	7.42	2.02	135	1044.08	H100	6876.51	75.24	406.13	373.85	-158.66	-23.00
ASRUN5857	13.62	2.09	135	1916.50	H150	8120.60	83.64	335.07	330.87	55.74	9.03

Table D.2: Baseline Data for the Second Harmonic Fit of the Smoothed Data

Column Title Descriptions:

Run # : The run number consists of the "Auto" file number in the DSA's software as well as the two experiment numbers where all recorded is stored for that particular frequency and compressor phase angle. The first two digit number is the run number that recorded pressure and heat flux measurements; the second two digit number is the run number that recorded centerline temperature and wall temperature measurements.

f: The frequency (Hz) of the particular run.

r_p : The pressure ratio for the run, (P_{HIGH} / P_{LOW}).

Ψ : The compressor phase angle between the pistons in the driven and the undriven compressors.

Pe_ω : The oscillating Peclet number for the run, which equals ($Re_\omega \times Pr$). For this data the Prandtl number, Pr , for air is assumed to be 0.71.

Volts: The voltage set on the auto transformer. The "L" or "H" denotes the belt setting for the pulleys connected to the DC motor, where "L" stands for low belt setting and "H" stands for high belt setting.

Q_{max} : The maximum smoothed heat flux (W/m^2) during one cycle.

T_{max} : The maximum smoothed temperature ($^{\circ}C$) during one cycle.

Nu_c : The magnitude of the complex Nusselt number which equals $(Nu_r^2 + Nu_i^2)^{1/2}$.

Nu_r : The real component of the complex Nusselt number.

Nu_i : The imaginary component of the complex Nusselt number.

$\Delta\phi$: The phase shift between heat flux and ΔT where a negative number denotes that heat flux leads ΔT .

References

- Aerometrics Incorporated, Sales Brochure "Aerometrics Doppler Signal Analyzer."
- Aerometrics Incorporated, Sales Brochure "Aerometrics Laser Doppler Velocimeter Systems."
- Akhavan, R., Kamm, R.D., and Shapiro, A.H., 1991, "An Investigation of Transition to Turbulence in Bounded Oscillatory Stokes Flow, Part 1. Experiments," *Journal of Fluid Mechanics*, Vol 225, pp 395-422.
- Bhunja, S.K., 1988, "A Refractive Index Matched Facility To Study Solid-Liquid Multiphase Flows Using Laser Velocimetry," M.S. Thesis, Dept. of Mech. and Aerospace Eng., Case Western University, Cleveland, OH.
- Drain, L.E., *The Laser Doppler Technique*, John Wiley and Sons, New York, 1980. pp 168-170.
- Faulkner, H.B., 1983, "An Investigation of Instantaneous Heat Transfer During Compression and Expansion in Reciprocating Gas Handling Equipment," Ph.D. Thesis, Dept. of Mech. Eng., MIT.
- Gedeon, D., 1986, "Mean-Parameter Modelling of Oscillating Flow," *Journal of Heat Transfer*, Vol 108, No 3, pp 513-518, August.
- Hino, M., Sawamoto, M., and Takasu, S., 1976, "Experiments on Transition to Turbulence in an Oscillatory Pipe Flow," *Journal of Fluid Mechanics*, Vol 75, Part 2, pp 193-207.
- Hino, M., Kashiwayanagi, M., Namayama, A. and Hara, T., 1983, "Experiments on the Turbulence Statistics and the Structure of a Reciprocating Oscillatory Flow", *Journal of Fluid Mechanics*, Vol 131, pp 363-400.
- Ho, Y., 1991, "Experimental Investigation of Heat Transfer with Combined Oscillating Pressure and Oscillating Flow," M.S. Thesis, Dept. of Mech. Eng., MIT.
- Jeong, E.S., 1991, "Heat Transfer with Oscillating Pressure in Reciprocating Machinery Flow," Ph.D. Thesis, Dept. of Mech. Eng., MIT.
- Kirmse, R.E., 1979, "Investigation of Pulsating Turbulent Pipe Flow," *Journal of Fluids Engineering*, Vol 101, pp 436-442.

- Kornhauser, A.A., and Smith, J.L. Jr., 1987, "A Comparison of Cylinder Heat Transfer Expressions Based on Prediction of Gas Spring Hysteresis Loss," *Fluid Flow and Heat Transfer in Reciprocating Machinery*, American Society of Mechanical Engineers, pp 89-96.
- Kornhauser, A.A., and Smith, J.L. Jr., 1988, "Application of a Complex Nusselt Number to Heat Transfer During Compression and Expansion," *On Flows in Internal Combustion Engines-IV*, American Society of Mechanical Engineers, pp 1-8.
- Kornhauser, A.A., and Smith, J.L. Jr., 1989, "Heat Transfer with Oscillating Pressure and Oscillating Flow," *Proceedings of the 24th Intersociety Energy Conversion Engineering Conference*, pp 2743-2753.
- Kornhauser, A.A., 1991, "Gas-Wall Heat Transfer During Compression and Expansion," Sc.D. Thesis, Dept. of Mech. Eng., MIT.
- Kurzweg, U.H., 1985, "Enhanced Heat Conduction in Fluids Subjected to Sinusoidal Oscillations," *Journal of Heat Transfer*, Vol 107, pp 459-462.
- Lee, K.P., 1983, "A Simplistic Model of Cyclic Heat Transfer Phenomena in Closed Spaces," *Proceedings of the 18th Intersociety Energy Conversion Engineering Conference*, pp 720-723.
- Lienhard, J.H. , *A Heat Transfer Textbook*, Prentice-Hall, Englewood Cliffs, NJ, 1987.
- Merkli, P., and Thomann, H., 1975, "Transition to Turbulence in Oscillating Pipe Flow," *Journal of Fluid Mechanics*, Vol 68, pp 576-575.
- Ohmi, M., Iguchi, M., and Urahata, I., 1982, "Flow Patterns and Frictional Losses in an Oscillating Pipe Flow," *Bulletin of the Japanese Society of Mechanical Engineers*, Vol 25, No 202, pp 536-543, April.
- Ramaprian, B.R., and Tu, S.W., 1983, "Fully Developed Periodic Turbulent Pipe Flow, Parts 1 and 2," *Journal of Fluid Mechanics*, Vol 137, pp 31-58, 59-81.
- Seume, J.R., and Simon, T.W., 1986, "Oscillating Flow in Stirling Engine Heat Exchangers," *Journal of the American Chemical Society*, Vol 118, pp 533-538.
- Simon, T.W., and Seume, J.R., 1988, "A Survey of Oscillating Flow in Stirling Engine Heat Exchangers," NASA-CR-182108.
- Overbye, V.D., Bennethum, J.E., Uychara, O.A., and Myers, P.S., 1961, "Unsteady Heat Transfer in Engines," *SAE Transactions*, Vol 69, pp 461-493.

- Pfriem, H., 1943, "Periodic Heat Transfer at Small Pressure Fluctuations," NACA-TM-1048, National Advisory Committee for Aeronautics, (Translated from *Forschung auf dem Gebiete des Ingenieurwesens*, Vol 11, No 2, 1940, pp 67-75).
- Schlichting, H, *Boundary Layer Theory*, McGraw-Hill, New York, 1979, pp 436-439.
- Shizgal, B., Goldsmith, H.L., and Mason, S.G., 1965, "The Flow of Suspensions Through Tubes IV: Oscillatory Flow of Rigid Spheres," *Canadian Journal of Chemical Engineering*, Vol 43, No 3, pp 97-101.
- TSI Incorporated, Mini-Course Handouts on Laser Doppler Velocimetry, 1992.
- Tziranis, A.K., 1992, "Temperature, Heat Flux, and Velocity Measurements in Oscillating Flows with Pressure Variations," M.S. Thesis, Dept. of Mech. Eng., MIT.
- Uchida, S., 1956, "The Pulsating Viscous Flow Superimposed on the Steady Laminar Motion of Incompressible Fluids in a Circular Pipe," *Z. Angew. Math. Phys.*, Vol 7, pp 403-422.
- White, F.M., *Viscous Fluid Flow*, McGraw-Hill, New York, 1991, pp 135-136.
- Womersley, J.R., 1955, "Method for Calculation of Velocity, Rate of Flow and Viscous Drag in Arteries when the Pressure Gradient is Known," *Journal of Physiology*, Vol 127, pp 553-563.